Plasma Physics Reports, Vol. 26, No. 1, 2000, pp. 1–9. Translated from Fizika Plazmy, Vol. 26, No. 1, 2000, pp. 3–11.

MAGNETIC CONFINEMENT SYSTEMS

Effect of the Transverse Magnetic Field on Turbulence and Parameters of a Plasma Column in the L-2M Stellarator

D. K. Akulina, G. M. Batanov, M. S. Berezhetskiĭ, G. A. Gladkov, S. E. Grebenshchikov, I. S. Danilkin, L. M. Kovrizhnykh, L. V. Kolik, A. B. Kuznetsov, N. F. Larionova, K. M. Likin, N. I. Malykh, A. I. Meshcheryakov, A. E. Petrov, K. A. Sarksyan, I. S. Sbitnikova, N. N. Skvortsova, O. I. Fedyanin, N. K. Kharchev, Yu. V. Khol'nov, and S. V. Shchepetov

Institute of General Physics, Russian Academy of Sciences, ul. Vavilova 38, Moscow, 117942 Russia

Received November 30, 1998; in final form, June 24, 1999

Abstract—The influence of magnetic configurations with magnetic hills or wells on the parameters of a plasma column and turbulence characteristics were studied in experiments in which the plasma was created and heated by a microwave beam at the second harmonic of the electron cyclotron frequency. Calculations show that, for $\langle\beta\rangle = (1.5–2) \times 10^{-3}$, a configuration with a magnetic well takes place and the Mercier criterion for stability of the ideal MHD modes is satisfied. It is shown that the compensation of the Shafranov shift of the plasma column by a transverse (vertical) field ($B_v/B_0 = 5 \times 10^{-3}$) leads to a configuration with a magnetic hill in which the Mercier stability criterion is violated in the central region of the plasma column. It is experimentally shown that the stored plasma energy in the magnetic-hill configuration is reduced by one-half in comparison with the magnetic-well configuration. In the case of a magnetic hill, the energy of fluctuations increases both in the plasma core and near the separatrix, and the quasi-regular components of the wavelet spectra grow. When the Shafranov shift is compensated only partially ($B_v/B_0 \sim 3 \times 10^{-3}$) and the system is near the instability threshold, the stored plasma energy and the central electron temperature are somewhat higher, and the radiation power of fast electrons from non-Maxwellian tails at the second harmonic of the electron gyrofrequency decreases. It is found that the wavelet spectra of fluctuations change, the coherence coefficient for spectral components increases, and the radial electric field near the separatrix decreases. © *2000 MAIK "Nauka/Interperiodica".*

1. In recent years, considerable efforts have been made to experimentally investigate the influence of turbulent processes on plasma confinement in magnetic confinement systems [1], in particular, in stellarators (see, e.g., [2–6]). However, for the most part, either attention was focused on the global confinement and stability for the purpose of attaining maximum β (this problem in itself is of extreme importance but is not connected directly with the turbulence characteristics of the central part of the plasma column) or the experiments were limited to studying turbulent processes in the edge plasma. Here, we attempt to determine the extent to which MHD activity (both at the edge and in the core of the plasma column) affects plasma confinement. To control MHD activity, we applied an external vertical magnetic field $\mathbf{B}_v$, which was used to correct the position of the plasma column in view of the Shafranov shift of the magnetic axis and the entire system of magnetic surfaces because of the finite β effect. This approach is based on the theoretical prediction that, for specific values of β in the L-2M stellarator, the vertical magnetic field can change a magnetic configuration with a magnetic well to a configuration with a magnetic hill in which the stability criterion for ideal MHD modes is violated in the central region of the plasma column. Such a formulation of the problem made it necessary to carry out measurements of the dependences of the spectral and statistical characteristics of plasma fluctuations on $\mathbf{B}_v$ along with parallel measurements of macroscopic parameters of the plasma, such as the stored plasma energy W and electron temperature T_e.

In addition, it was necessary to measure the fluctuation parameters independently in the core and at the edge of the plasma. It is obvious that a comparative analysis of the dependences obtained will allow us to draw some inferences about the influence of MHD activity on the plasma confinement, keeping in mind that ideal MHD modes are excited in the core region and, as shown in [5], resistive-ballooning modes are excited at the edge. Finally, note that wavelet analysis has been used to process the experimental data. This technique, which was developed in the last few years, allows one to obtain information on the spectra and coherence of various spectral components with a high time resolution [7]. The configurations of magnetic surfaces for the L-2M experimental conditions were

1063-780X/00/2601-0001$20.00 © 2000 MAIK "Nauka/Interperiodica"

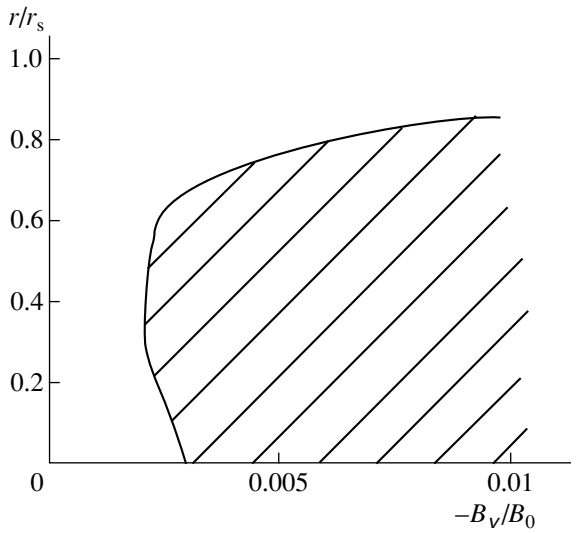

Fig. 1. The position of the instability domain in the (r, B_v) plane (mean radius of the magnetic surface versus the correcting vertical field) for $\langle\beta\rangle = 0.002$ and a parabolic pressure profile. In the hatched region, the Mercier stability criterion is violated.

obtained by studying the plasma equilibrium using the numerical procedure described in [8].

2. The main characteristics of the L-2M stellarator are described quite comprehensively in [9]. The stellarator has a high magnetic shear and a planar geometrical axis. The polarity is $l = 2$, the number of helical periods is $N = 14$, the major radius of the torus is $R = 100$ cm, and the mean radius of the vacuum separatrix surface is $r_s = 11.5$ cm. The vacuum angle of the rotational transform is $i = 0.185$ on the magnetic axis and 0.78 near the separatrix. The magnetic axis of the vacuum magnetic surfaces is shifted inward from the toroidal axis by 2.5 cm ($R = 97.5$ cm).

A plasma was created and heated with a 75-GHz ($\lambda = 4$ mm) gyrotron. The experiments described below were carried out at a power of 180–240 kW and discharge duration of 10–12 ms. For a longitudinal magnetic field of $B_0 = 1.34$ T, the electron cyclotron resonance (ECR) at the second harmonic occurred at $R = 100$ cm. A linearly polarized microwave was launched through a horizontal port of the vacuum chamber from the low-field side. The plasma radius in these experiments was controlled by a graphite limiter installed in the horizontal port on the low-field side. The limiter height was 70 mm, and its edge was shaped so as to coincide with the last magnetic surface of the 11.5-cm mean radius. The limiter was usually located 12 mm inward from the separatrix surface and, in some cases, this distance was increased to 30 mm. The plasma parameters typical of these experiments were the following: the mean density was $\bar{n} \approx (1–2) \times 10^{13}$ cm^{-3}, and the central electron temperature was $T_e(0) = 0.7–0.8$ keV. The thermal energy (energy content) of the plasma, W, was derived from diamagnetic measurements. The electron temperature T_e and its radial profile $T_e(r/r_s)$ were measured by a soft X-ray foil technique. In addition, the $T_e(r/r_s)$ profile was measured from the intensity of emission at the second harmonic of the electron cyclotron frequency at frequencies of 77–80 GHz. We also recorded the emission from fast electrons at a frequency of 71 GHz in the ECR region (taking into account the strong relativistic shift of their gyrofrequency). The plasma radiation power was measured by a pyroelectric detector.

Fluctuations of the electron density in the hot regions were studied by the phase-contrast technique (small-angle scattering) using a scattered ordinary wave that arose due to the splitting of linearly polarized microwaves used for ECR heating of the plasma. In this case, the amplitude of the density fluctuations was proportional to the amplitude of the radiation fluctuations [10].

The radial and poloidal structure of fluctuations and turbulent particle transport at the plasma edge was studied with the help of movable Langmuir probes described in detail in [5].

3. Applying the magnetic field $\mathbf{B}_v$ orthogonal to the equatorial plane of the stellarator, we can shift the magnetic surface along the major radius.[1] The inward shift decreases the helical modulation of the field (i.e., the ripple amplitude) and the trapped-particle density. The outward shift leads to the formation of a magnetic well in the central region of the plasma column ($r/r_s = 0.5$ for $\varepsilon = B_v/B_0 = 0.005$). As the shift increases, the magnetic well deepens and broadens. A similar effect occurs as a result of a finite plasma pressure [8] because of the Shafranov shift of magnetic surfaces.

Ideal MHD modes at the plasma edge near the separatrix in the L2-M stellarator are stabilized by the magnetic shear. Resistive modes are not stabilized by the shear. The formation of a magnetic well due to the outward shift of the magnetic surfaces (caused by either the vertical field or the Shafranov shift) leads to the stabilization of both the ideal and resistive MHD modes in the central region. If the vertical field is applied in such a way as to decrease the Shafranov shift caused by the plasma pressure, the depth of the magnetic well decreases and the stability region becomes narrower. Figure 1 shows the instability domain for ideal MHD modes, which is calculated taking into account both the finite plasma pressure and the vertical magnetic field. The vertical field leads to the shift of the magnetic configuration toward smaller values of the major radius, thus compensating for the Shafranov shift. Figure 2 shows the results of calculations of the magnetic surfaces (with the finite plasma pressure taken into account) for the case when the vertical field is absent and for the case $B_v = -40$ G, when the plasma column

[1] The initial shift of the magnetic axis in the vacuum magnetic configuration is 2.5 cm for $B_v/B_0 = 0.005$ ($B_v \approx 70$ G).

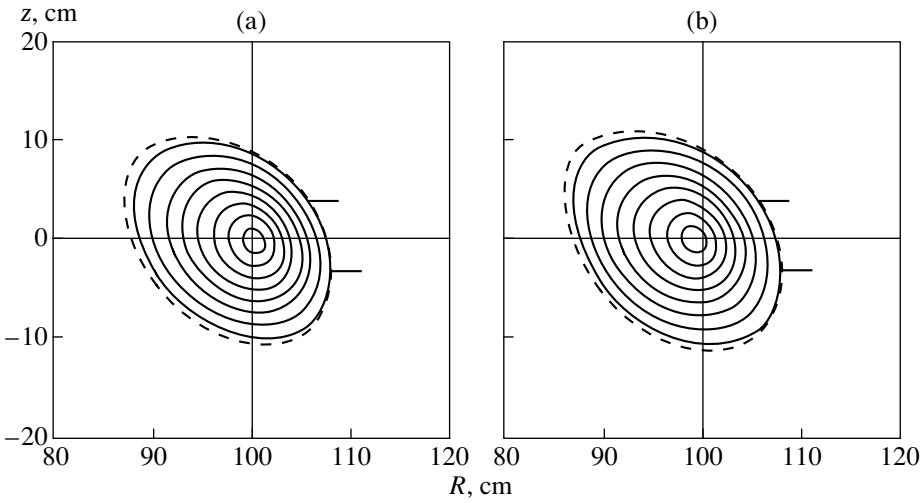

Fig. 2. Magnetic surfaces for $\langle\beta\rangle = 0.0025$ and B_v = (a) 0 and (b) –40 G.

is near the instability threshold for ideal MHD modes.[2] It is seen from Fig. 1 that, for $B_v = -40$ G, there is a narrow region in which the Mercier stability criterion [11] is violated ($r/r_s \approx 0.5$). For $B_v/B_0 > -0.002$, the plasma column is stable because of the effect of self-stabilization of ideal MHD modes.

Hence, for the vertical field compensating for the Shafranov shift of the plasma column, one would expect an increase in the level of density fluctuations in the central region of the plasma column and deterioration of plasma confinement.

The plasma stability against MHD modes depends on the radial profile of the plasma pressure [8]. By shifting the resonance region across the plasma column, it is possible to change the temperature and pressure profiles. Ray-tracing calculations using the procedure described in [12] yield a peaked power deposition profile with a 2–3-cm diameter for on-axis heating and a hollow profile in the shape of a 2–3-cm-thick ring, centered on the axis of the plasma column, for off-axis heating. The power deposition densities in this case differ by one order of magnitude, attaining 40 W/cm^3 for on-axis heating. Calculations show that the total absorption coefficient is about 0.86–0.98 and varies only slightly as the resonance region shifts. The transport rates and the profiles of the plasma parameters were also calculated by the neoclassical transport model with allowance for turbulent transport at the plasma edge [13]. These calculations showed that variations in the power density by more than one order of magnitude weakly affect variations in the mean and maximum values of the temperature and the energy confinement time.

[2] The negative values of B_v correspond to the inward shift of the magnetic configuration, and the positive values correspond to the outward shift.

4. Let us consider in more detail the results of the measurements of the plasma parameters and turbulence characteristics for different values of the vertical field B_v. The measurements were performed for four field values $B_v = 0, -40, -70$, and +70 G. The Mercier stability criterion is satisfied for $B_v = 0$ and +70 G. The value $B_v = -40$ G lies near the instability threshold, so that MHD modes may become unstable in a certain region of the plasma. At $B_v = -70$ G ($B_v/B_0 = -0.005$), the criterion is violated and the instability region expands over the entire cross section of the plasma column (Fig. 1).

Figure 3 shows the electron temperature profiles obtained from the measurements of soft X radiation by the foil technique for different positions of the resonant point along the major radius. When the resonant point lies on the axis of vacuum magnetic surfaces (B_0 (R = 100 cm) = 1.3 T), the temperature profile in the core plasma flattens. When the resonant point is shifted outward, the temperature maximum is shifted outward by 2–3 cm from the vacuum magnetic axis, which can be attributed to the effect of the Shafranov shift of the magnetic axis. The flattened profile in the case when the resonant point lies on the vacuum magnetic axis is also explained by the Shafranov shift, keeping in mind that the heating region has the shape of a ring. The partial compensation of the Shafranov shift at $B_v = -40$ G somewhat smoothes the temperature profile. It is seen from the results presented that variations in the power density caused by the shift of the resonant point result in variations of the maximum temperature by a factor of no more than 1.5, which agrees with calculations using the neoclassical model [13].

The measurements of the temperature by the intensity of emission at the second harmonic of the electron cyclotron frequency (77 GHz), shifted by 2.7% from the gyrotron frequency, show that the temperature

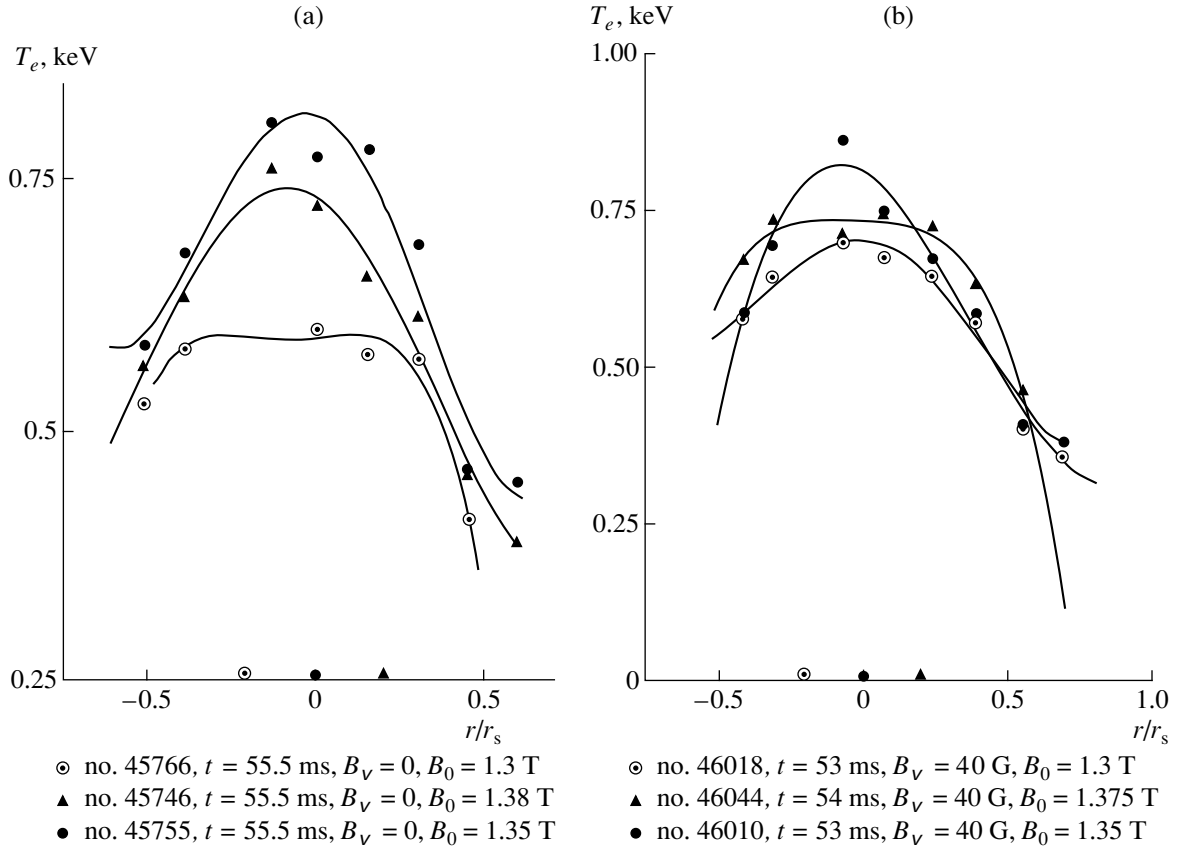

Fig. 3. Electron temperature profiles for different values of the toroidal field B_V = (a) 0 and (b) –40 G. The positions of the resonant points for the corresponding values of the toroidal field are marked on the abscissa.

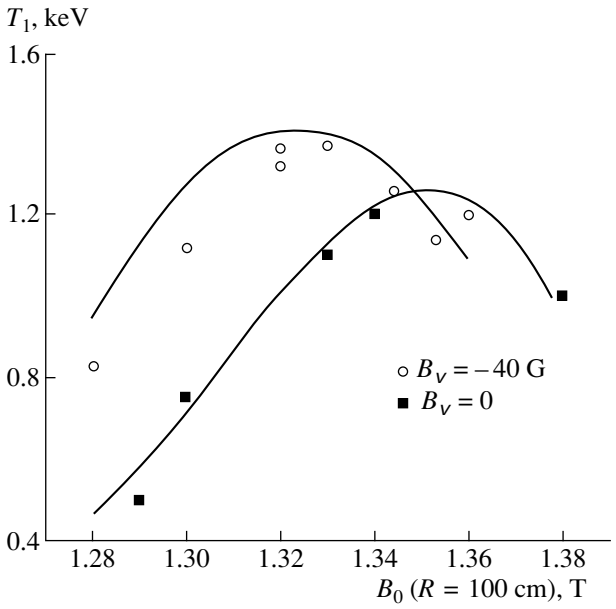

Fig. 4. Electron temperature measured by the intensity of radiation at a frequency of 77 GHz, as a function of the toroidal field.

increases with shifting the resonant point outward (Fig. 4), which is qualitatively consistent with the Shafranov (outward) shift of the magnetic axis. When the Shafranov shift is partially compensated, the outward shift of the resonant point is accompanied by a decrease in the electron temperature (for $B_0 > 1.35$ T).

It is seen from Fig. 5 that an increase in the toroidal field (i.e., the outward displacement of the resonant point) results in a nearly fourfold increase in the radiative temperature of fast electrons.[3] The compensation of the Shafranov shift almost completely cancels the dependence of the radiative temperature of fast electrons on the position of the resonant point. The increase in the radiative temperature of the fast electrons with increasing the outward displacement of the resonant point is apparently explained by the fact that the Shafranov shift is accompanied by an increase in both the trapped-particle density and the heating-power density. The compensation of the Shafranov shift results in less efficient generation of fast electrons because of a decrease in the power deposition density. (Note that our

[3] The radiative temperature was calculated by the radiation power of fast electrons within the receiver band assuming that the plasma radiation is blackbody radiation.

previous experiments demonstrated that the radiative temperature of fast electrons strongly increases with the heating power [14].)

The higher value of the temperature measured by the intensity of radiation at the second harmonic of the electron cyclotron frequency as compared to that measured by the foil technique can be explained by the fact that the former was determined in the initial stage of the discharge, 1–2 ms after the electron density reached a value of 10^{13} cm^{-3}, whereas the latter was measured 5–7 ms after the beginning of the discharge, when the electron density grew to $(1.2–1.5) \times 10^{13}$ cm^{-3}. It was shown in [14] that the central temperature varies nearly in inverse proportion to the mean electron density.

A greater inward shift of the magnetic axis (B_v = –70 G) leads to an appreciable decrease in the maximum temperature (by a factor of 1.5), whereas the outward shift (B_v = +70 G) reduces it only slightly (to 0.9).

Applying the vertical field strongly affects the plasma energy (Fig. 6). For B_v = –40 G and B_v = 0, there is little sense to talk about the change of the plasma energy within the scatter in diamagnetic signals. At the same time, for B_v = –70 G, a significant decrease in the plasma energy (to 150–200 J) is observed in comparison to that for B_v = 0 and –40 G (~300–320 J). A significant difference is also observed in the time behavior of the plasma energy at various values of the vertical field. For B_v = 0 and –40 G, the plasma energy measured by the diamagnetic signal reaches its steady-state value 4–5 ms after the beginning of the discharge, whereas for B_v = –70 G, it reaches a maximum value of 260–280 J in 4–5 ms and then decreases to 180–200 J at the end of the discharge. The time behavior of the mean density and radiation loss is also different in these cases. For B_v = 0 and –40 G, the electron density increases from 0.9×10^{13} to $(1.5–1.6) \times 10^{13}$ cm^{-3} and the radiation power reaches 80–90 kW at the end of the discharge. For B_v = –70 G, the density grows more rapidly, reaching $(1.8–1.9) \times 10^{13}$ cm^{-3} at the end of the discharge and the radiation power increases to 130 kW, which comprises 75% of the heating power. At a vertical field of +70 G, when the magnetic surfaces are shifted outward and a magnetic well forms in the central region ($r/r_s \le 0.5$) of the initial magnetic configuration, the density increases from 10^{13} to 1.5×10^{13} cm^{-3} and the radiation power is less than 70 kW. In this case, the plasma energy reaches its steady-state value (~240 J) 4–5 ms after the beginning of the discharge.

Hence, the strongest decrease in the energy and the central temperature is observed for B_v = –70 G, i.e., when the Mercier stability criterion is violated.

5. The characteristics of turbulent plasma fluctuations were measured under the same experimental conditions as for the measurements of the energy, temperature, and other macroscopic parameters of the plasma. The measurements of the plasma-density fluctuations

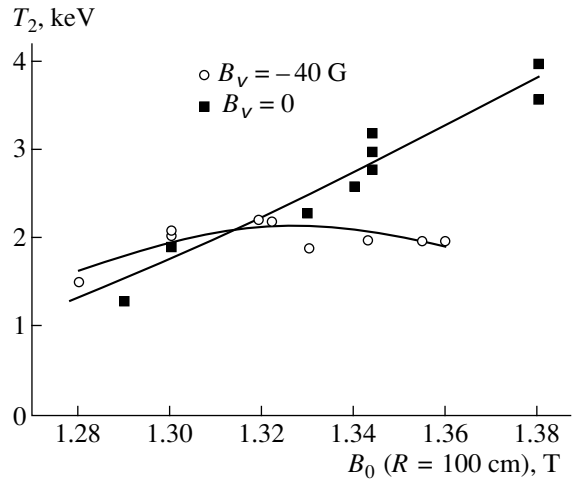

Fig. 5. Radiative temperature of fast electrons, measured from the intensity of radiation at a frequency of 71 GHz, as a function of the toroidal field.

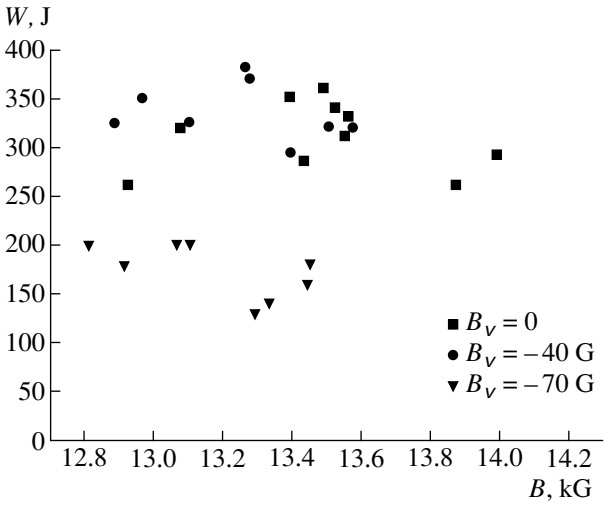

Fig. 6. Plasma energy measured from diamagnetic signals.

show that the fluctuation energy in the plasma core increases by a factor of 2 when the vertical field changes from B_v = 0 to –70 G. In this case, the intensity of noise grows continuously during the discharge. The wavelet spectra of turbulent noise are shown in Fig. 7. They are obtained for the same instants with averaging over an interval of 1–3 ms. In the absence of a vertical field, we observed a spectrum that dropped off continuously at high frequencies and contained broadband quasi-coherent oscillations at frequencies of about 50 kHz and low-intensity bands near 10 and 20 kHz. For B_v = –40 G, a redistribution of noise energy over the spectrum is observed. The maximum of broadband quasi-coherent oscillations shifts to 60 kHz, and a single broad band with a maximum near 15 kHz is seen at low frequencies. For B_v = –70 G, the fraction of the

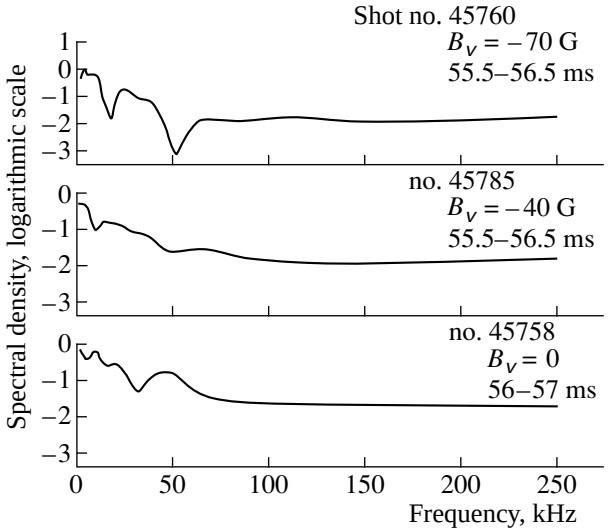

Fig. 7. Wavelet spectra of the heating radiation transmitted through the plasma.

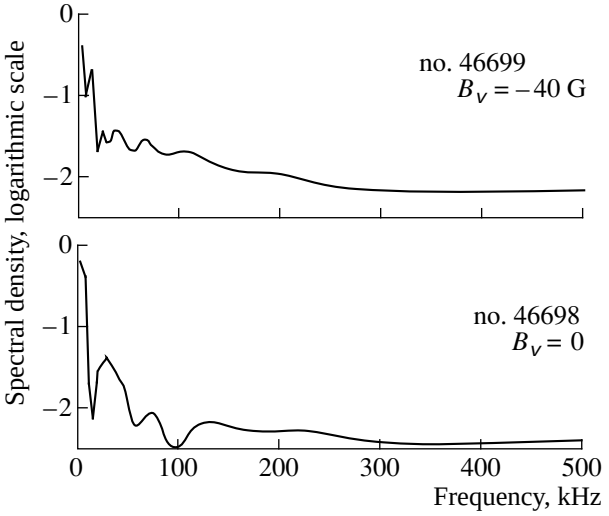

Fig. 8. Wavelet spectra of the floating potential of a probe in the edge plasma ($r/r_s = 0.86$).

energy of quasi-harmonics in the total noise energy is substantially increased as compared to the previous case. Two broad bands with peaks of spectral density at 7.5 and 25 kHz are clearly seen in the spectrum. The increase in the energy of quasi-harmonics with increasing the vertical field is also confirmed by the shape of the time correlation functions: along with the central peak, an appreciable excess of the correlation coefficient above the random noise is recorded at long correlation times (0.1–1 ms).

Measurements of the bicoherence coefficient also show that the nonlinear interaction of oscillations changes when the vertical field is applied: the bicoherence coefficient increases from 0.05 at $B_v = 0$ to 0.09–0.12.

The wavelet spectra of fluctuations in the floating potential in the edge plasma, which are shown in Fig. 8, also demonstrate well-pronounced frequency bands. Compensation of the Shafranov shift increases the amplitude of fluctuations over the entire frequency spectrum for the plasma radii $1 \geq r/r_s \geq 0.86$. Both the plasma potential and the radial electric field decrease in this case (Fig. 9). For $B_v = -40$ G, the radial and poloidal coherence coefficients turn out to be higher than for $B_v = 0$ (Fig. 10).

A comparison of the results of measuring the scattering of the heating radiation and the electric-field fluctuations in the edge plasma shows that the inward shift of the plasma results in enhancement of turbulence in both the core and edge plasma. Quasi-harmonic structures are formed and a coupling appears between the central and peripheral regions of the plasma column. Hence, under conditions when the Mercier stability criterion for ideal MHD modes is violated, we observe an increase in the energy of fluctuations in the central region of the plasma together with energy redistribution in the oscillation spectra and the formation of quasi-harmonic structures. The instability conditions for resistive MHD modes at the plasma edge are fulfilled for any value of the vertical field, whereas the ideal MHD modes are stable at the plasma edge because of the high value of the shear. Nevertheless, an increase in the fluctuation level and the energy redistribution over the oscillation spectrum are also observed at the plasma edge when the ideal MHD modes are unstable in the central region of the plasma. This is evidence that instabilities in the central region of the plasma affect the edge plasma.

6. A comparison of the results of measuring the energy and plasma turbulence in the presence of the vertical field shows that the noise energy increases, the turbulent spectra are regularized, and the stored plasma energy decreases at the values of the vertical field at which ideal MHD modes are unstable according to the Mercier criterion. However, the reduction of the plasma energy may also be attributed to an increase in the electron density and energy loss because of a more intense interaction with the chamber wall at the inner circumference of the torus, especially for $B_v = -70$ G. In this case, because of the imperfect fabrication and assembly of the chamber, the vacuum separatrix magnetic surface probably intersects the wall even when the limiter is 1.2 cm inside the separatrix. Therefore, it is necessary to carry out an additional analysis to clear up how the limiter and the shift of magnetic surfaces due to the vertical field or the plasma pressure affect the heating conditions and plasma confinement.

Our previous experiments showed that introducing the limiter in the absence of a vertical field decreases both the stored plasma energy and the rate at which the electron density and radiation grow [9]. Measurements with thermocouples showed that, as the limiter is inserted into the plasma, the fraction of energy

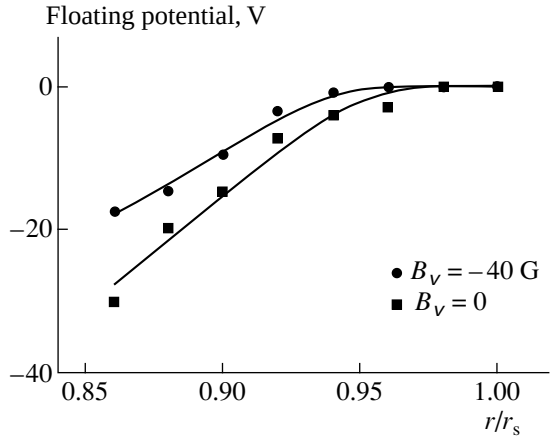

Fig. 9. Floating potential of a vertically oriented probe as a function of radius.

absorbed by the limiter increases, reducing both the recycling at the walls and the plasma radiation. However, the growth of the density and radiation during the discharge usually does not decrease the plasma energy, because the diamagnetic signal remains constant up to the end of the heating pulse even when the limiter is removed from the separatrix. Under these conditions, the plasma energy is nearly proportional to the square of the plasma radius. The fact that the diamagnetic signal remains constant while the plasma radiation grows indicates that the radiative loss does not contribute substantially to the energy balance. It is likely that, in this case, the radiative loss occurs at the plasma edge and affects only a narrow peripheral region (the effective radius of the plasma depends only slightly on the size of this region). When the diamagnetic signal falls during the discharge, it is likely that the effective cross section of the plasma decreases because of a decrease in the central temperature accompanied by the growth of the plasma density and expansion of the radiative-loss region.

The shift of the magnetic surfaces by applying the vertical field changes the depth to which the limiter is inserted into the plasma and, consequently, changes the ratio between the particle and heat fluxes onto the wall and the limiter, which explains the change in the growth of the density and radiation. It is evident that the depth

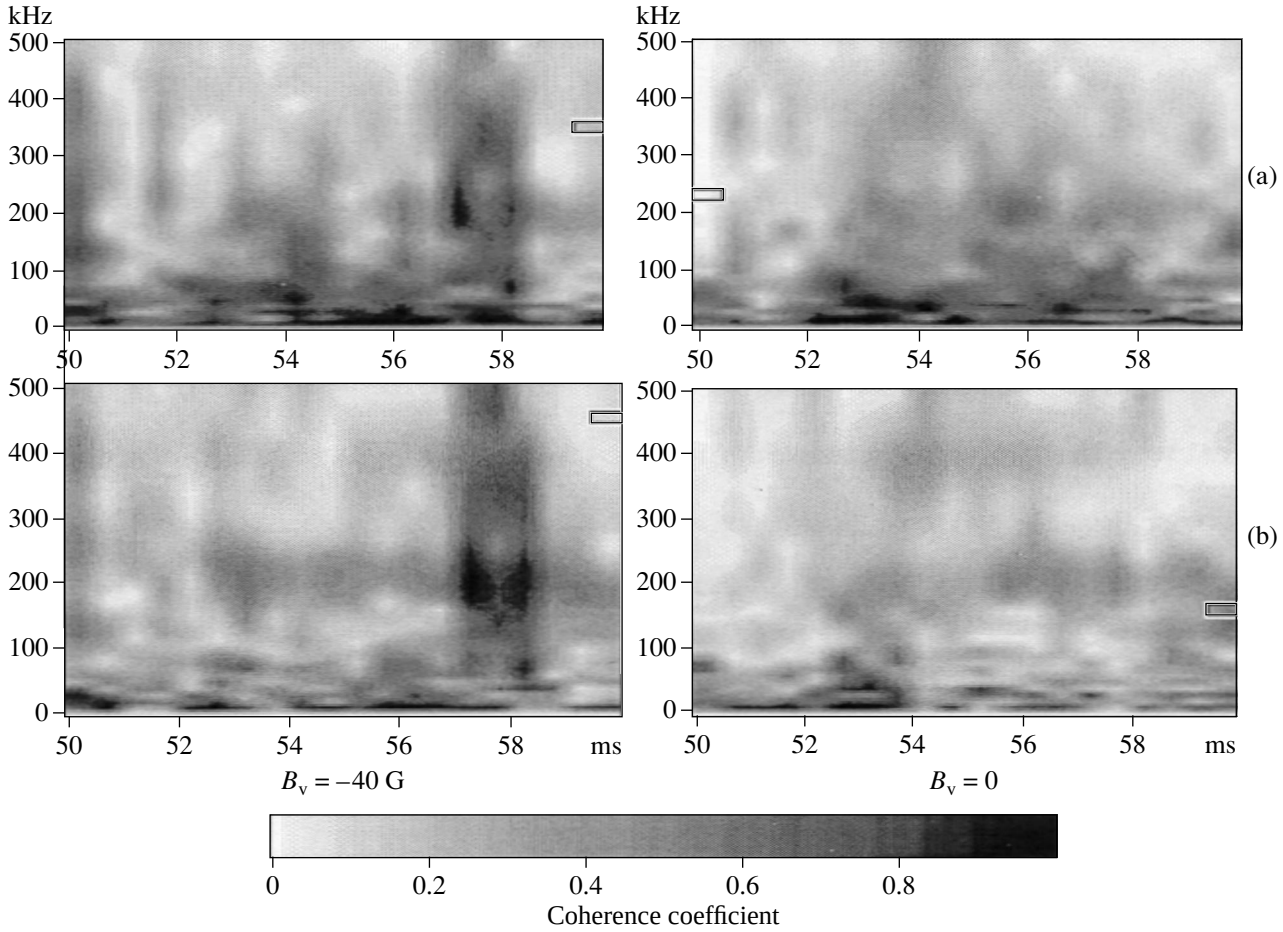

Fig. 10. Coherence coefficient of oscillations of the floating potential as a function of time and frequency in (a) poloidal and (b) radial directions. The distance between the probes is 4 mm.

to which the limiter is inserted into the plasma decreases when the magnetic surfaces shift inward and increases when they shift outward. As a result, the mean plasma radius changes. From calculations using the model [8], we obtain that when the limiter is located 1.2 cm inward from the separatrix surface the mean radii of the last closed magnetic surfaces for the values of the vertical field of +70, 0, –40, and –70 G are equal to 8.6, 9.7, 10.5, and 10.8 cm, respectively (for $\langle\beta\rangle \approx 0.2\%$). Correspondingly, it was expected that, compared to the case $B_v = +70$ G (when the radius is minimum), the plasma energy in the last three cases should be higher by a factor of 1.27, 1.49, and 1.56, respectively. In fact, the measurements show that, for $B_v = 0$, the plasma energy is higher by a factor of 1.25. For $B_v = -40$ G, the energy increases by a factor of 1.38, which is somewhat lower than the predicted value. For $B_v = -70$ G, the maximum of the diamagnetic signal increases insignificantly (by a factor of 1.17) and drops to 0.83 at the end of the heating pulse. Thus, the shift of the discharge conditions to the instability region for ideal MHD modes results in a pronounced deviation from the proportionality between the plasma energy and the square of the plasma radius.

A somewhat different dependence of the plasma energy on the vertical field is observed when the limiter is located 3 cm inside the vacuum separatrix. In this case, the mean radius of the last closed magnetic surface for $B_v = +70$ G is equal to 6.2 cm and that for $B_v = -70$ G is equal to 8.8 cm; i.e., the corresponding plasma cross-section areas should differ by a factor of 2. Indeed, we observe an increase in the plasma energy, but by no more than a factor of 1.3. However, for $B_v = -70$ G and a limiter depth of 3 cm, the energy turns out to be the same as for 1.2 cm, although one would expect a reduction in the plasma energy by a factor of about 1.3 (according to calculations, the mean radii of the last magnetic surfaces are 8.8 and 10.2 cm, respectively). Calculations show that, for smaller radii, the pressure growth leads to the stabilization of MHD modes and the size of the instability region is reduced. Actually, the measurements of scattering of the heating radiation show that the fluctuation amplitude decreases as the plasma cross-section area decreases.

An increase in the heating power to 220–240 kW at $B_v = -40$ G leads to an increase in the plasma density to $(1.8–2.0) \times 10^{13}$ cm^{-3} and in the radiation loss to 130–140 kW; i.e., these quantities increase to the same levels as for the discharge at $B_v = -70$ G and a heating power of 180–190 kW. However, at a higher power, an increase in the density and radiation loss does not lead to a decrease in the plasma energy. In contrast, the plasma energy increases to 500 J; i.e., the increase in the power by even a quarter results in a twofold increase in the plasma energy. The difference is that, for $B_v = -70$ G, ideal MHD modes should be unstable over the entire plasma cross section, except for the edge, whereas, for $B_v = -40$ G, instability should only occur in a narrow region. There exists another peculiarity of the plasma confinement that confirms the substantial influence of the increase in the plasma density and radiative loss on the plasma energy at a power of 220–240 kW and $B_v = -40$ G. When the limiter depth changes from 3 to 1.2 cm, the plasma energy increases by a factor of 1.33 (from 375 to 500 J), i.e., nearly proportionally to the cross-section area (the mean radius of the boundary surface increases from 8.8 to 10.5 cm). Note that such an increase in the plasma energy occurs in spite of the fact that the radiation loss increases from 100 to 130–140 kW.

Hence, the analysis of the influence of various factors on plasma confinement shows that the lowest energy is observed when the instability threshold for ideal MHD modes is substantially exceeded over the entire plasma cross section, except for the edge.

7. In conclusion, we summarize the main results of the study. When the resonance region shifts along the major radius, the stored plasma energy remains unchanged to within the measurement error, although the temperature profile in the plasma core ($r/r_s \le 0.5$) varies. The inward shift of the magnetic surfaces caused by the vertical field that partially compensates the Shafranov shift due to the finite plasma pressure leads to a smoothing of the temperature profiles and the suppression of emission from fast electrons.

The inward shift of the magnetic surfaces violates the stability criterion for ideal MHD modes over the entire plasma cross section, except for the edge region. In this case, a decrease in the plasma energy and the central electron temperature and an increase in the mean electron density and radiative loss are recorded. By analyzing the scattering of the heating radiation, it is found that the fluctuation amplitude and the fraction of quasi-harmonic components in the fluctuation spectrum in the central region of the plasma column double. At the same time, an increase in the fluctuation level and a redistribution of the energy over the fluctuation spectrum are observed in the edge plasma. Presumably, when the instability threshold for ideal MHD modes is exceeded over the entire cross section (except for the edge region), a decrease in the plasma energy is related to plasma turbulence, which plays a decisive role in reducing the plasma lifetime in a stellarator.

ACKNOWLEDGMENTS

This work was supported in part by the Russian Foundation for Basic Research, project nos. 96-02-16107 and 98-02-1645.

REFERENCES

1. C. Hidalgo, Plasma Phys. Controlled Fusion **37**, A53 (1995).
2. J. H. Harris, M. Murakami, B. A. Carreras, *et al.*, Phys. Rev. Lett. **63**, 1249 (1989); Phys. Fluids B **2**, 1353 (1990).

3. O. Motojima, F. Sano, M. Sato, *et al.*, Nucl. Fusion **25**, 1785 (1985).
4. S. Okamura, K. Matsuoka, K. Nishimura, *et al.*, Nucl. Fusion **35**, 283 (1995).
5. G. M. Batanov, O. I. Fedyanin, N. K. Khartchev, *et al.*, Plasma Phys. Controlled Fusion **40**, 1241 (1998).
6. M. A. Pedrosa, C. Hidalgo, and B. Van Milligen, Plasma Phys. Controlled Fusion **38**, 365 (1996).
7. N. N. Astaf'eva, Usp. Fiz. Nauk **166**, 1145 (1996).
8. C. V. Shchepetov and A. B. Kuznetsov, Nucl. Fusion **36**, 1097 (1996).
9. V. V. Abrakov, D. K. Akulina, E. D. Andryukhina, *et al.*, Nucl. Fusion **37**, 233 (1997).
10. V. G. Zhukovskiĭ, *Plasma Density Fluctuations* (Énergoatomizdat, Moscow, 1993).
11. C. Mercier, Nucl. Fusion **2**, 81 (1962).
12. K. M. Likin and B. F. Ochirov, Fiz. Plazmy **18**, 81 (1992) [Sov. J. Plasma Phys. **18**, 42 (1992)].
13. S. E. Grebenshchikov, I. S. Danilkin, and N. B. Mineev, Fiz. Plazmy **22**, 609 (1996) [Plasma Phys. Rep. **22**, 551 (1996)].
14. D. K. Akulina, G. A. Gladkov, Yu. I. Nechaev, and O. I. Fedyanin, Fiz. Plazmy **23**, 32 (1997) [Plasma Phys. Rep. **23**, 28 (1997)].

Translated by N. F. Larionova

Plasma Physics Reports, Vol. 26, No. 1, 2000, pp. 10–20. Translated from Fizika Plazmy, Vol. 26, No. 1, 2000, pp. 12–23.

PLASMA DYNAMICS

Capillary Discharges for Guiding of Laser Pulses

N. A. Bobrova*, S. V. Bulanov, A. A. Esaulov*, and P. V. Sasorov***

**Institute of Theoretical and Experimental Physics, Bol'shaya Cheremushkinskaya ul. 25, Moscow, 117259 Russia*
***Institute of General Physics, Russian Academy of Sciences, ul. Vavilova 38, Moscow, 117942 Russia*

Received March 30, 1999

Abstract—The dynamics of a capillary discharge is studied to achieve optimum conditions for the guiding of ultrashort intense laser pulses. A dynamic regime is revealed in which, after a short transient process, the discharge plasma is in dynamic and thermal equilibrium. Such plasma configuration is stable against MHD perturbations. It is shown that the radial inhomogeneity of the discharge plasma composition can provide the improvement of the focusing properties of a plasma waveguide. The radius of the region where electromagnetic radiation is localized is governed by a contact discontinuity between the plasma that initially fills the channel and the plasma that is produced due to ablation of the capillary wall material. © *2000 MAIK "Nauka/Interperiodica".*

1. INTRODUCTION

Ultrashort laser pulses with intensities on the order of $10^{18–21}$ W/cm^2 [1, 2] are widely used in studies on the higher harmonic generation, X-ray lasers, nuclear fusion, and new methods of charged particle acceleration [3–5]. In most applications, conditions should be created for both focusing of laser radiation to a small spot of radius r_0 and transportation of the laser pulse over many Rayleigh lengths ($l_R = \pi r_0^2/\lambda$, where λ is the wavelength of laser light) without diffraction spreading.

In the case of the laser wake-field accelerator (LWFA) [3, 4, 6], it is necessary to provide transportation of the laser pulse in an underdense plasma over distances on the order of the acceleration length $l_{acc} \approx (c/\omega_{pe})(\omega_0/\omega_{pe})^2$ without significant spreading. Here, $\omega_{pe} = (4\pi n_e e^2/m)^{1/2}$ is the Langmuir frequency and ω_0 is the carrier frequency of laser radiation. The ratio $\omega_0/\omega_{pe} \sim n_e^{-1/2}$, where n_e is the electron plasma density, should be as large as ≈10–100. On the other hand, if one needs to get into the regime with a fairly high acceleration rate, this ratio should not be too large, because the electric field amplitude in a wake wave is proportional to $n_e^{1/2}$. Also, in order for the particles not to slip out of the acceleration phase in the model of unlimited wake-field acceleration, which can be realized in a nonuniform plasma with a density profile properly chosen [7], laser pulses should be guided over distances longer than l_{acc}.

The diffraction spreading of laser pulses can be prevented by either the self-focusing of high-power electromagnetic radiation in an underdense plasma [8, 9] or the guiding of the laser pulse in a narrow channel (initially empty or prefilled with a plasma) [10]. The possibility of the laser-pulse guiding due to relativistic self-focusing and the electron acceleration in a relativistically self-guided channel were demonstrated in [9] and [11], respectively. This regime can be attained only with laser light intensities above $P_{cr} \approx 16.5\ (\omega_0/\omega_{pe})^2$ GW. The guiding of 2-TW 1-μm laser pulses can be achieved if the electron density is higher than $n_e > 10^{19}$ cm^{-3}. However, the guiding in such regimes can be accompanied by the onset of various instabilities. It is natural to expect that, instead of a regular wake field, irregular Langmuir oscillations will be generated, as was demonstrated by particle-in-cell simulations [12].

The laser-pulse guiding and the excitation of the wake field with a regular structure can be provided in a plasma-filled channel created in a dielectric (such a channel can also be produced in a plasma). As a result, the efficient acceleration of charged particles can be achieved [12]. The experimental demonstration of the laser-pulses guiding in a plasma waveguide formed near the axis of the capillary discharge was reported in [13].

Here, we present the results of MHD simulations aimed at determining the optimum conditions for the laser-pulse guiding and studying the influence of the radial inhomogeneity of the discharge plasma composition on the properties of a plasma waveguide. The laser-pulse guiding in capillary discharges is important for the generation of wake fields with regular structures and efficient acceleration of charged particles.

2. PLASMA WAVEGUIDE PARAMETERS

We write out the expressions for the acceleration length l_{acc} and the effective radius r_w of the region in which electromagnetic radiation is localized in a

plasma waveguide with a parabolic electron density profile $n_e(r) = n_e(0) + n_e''(0)r^2/2$:

$$l_{acc} = \frac{\lambda}{2\pi}\left[\frac{n_{cr}}{n_e(0)}\right]^{3/2}, \quad (1)$$

$$r_w = (\lambda R_0)^{1/2}\left[\frac{n_{cr}}{2\pi^2 n_e(0)}\right]^{1/4}\left[\frac{n_e(0)}{n_e''(0)R_0^2}\right]^{1/4}. \quad (2)$$

We assume that the channel radius R_0 is larger than r_w and that the critical density n_{cr} defined by the condition $\omega_{pe} = \omega_0$ is higher than $n_e(0)$. In this case, the transverse dimension r_w of the region where electromagnetic radiation is localized is proportional to $[n_e(0)d_e^2/n_e''(0)]^{1/4}$, where $d_e = c/\omega_{pe}$.

Conditions appropriate for the laser-pulse guiding can also be reached in plasma waveguides with a steplike radial electron density profile. If the plasma density in the region $r < r_1$ corresponds to $\omega_{p0} = (4\pi e^2 n_{e0}/m)^{1/2}$ and, at distances larger than r_1 from the axis of the system, the Langmuir frequency is equal to $\omega_{p1} = (4\pi e^2 n_{e1}/m)^{1/2}$, where $n_{e0} < n_{e1}$, then a laser pulse is radially localized in a region whose characteristic dimension r_1 satisfies the condition $r_1 > c/(\omega_{p1}^2 - \omega_{p0}^2)^{1/2}$.

For lasers operating at wavelengths of 1 μm, it is necessary to use waveguides in which r_1 is on the order of 10 μm (for plasma channels with parabolic density profiles, we have $r_w \approx 10$ μm). The electron density at the waveguide axis should be on the order of $\approx 10^{19}$ cm^{-3}. For CO_2 lasers operating at wavelengths of 10 μm, it is necessary to use waveguides with r_1 on the order of 100 μm (this corresponds to $r_w \approx 100$ μm for plasma channels with parabolic density profiles). In this case, the electron density at the waveguide axis is on the order of $\approx 10^{17}$ cm^{-3} (see the discussion in [14]).

Below, we will show that waveguides with the parameters just mentioned can be produced in capillary discharges. Simulations of the dynamics of capillary discharges used to create an X-ray laser [15] revealed regimes in which the plasma parameters are close to those required for the guiding of laser pulses. Note that smooth plasma density profiles with a local minimum of the electron density on the channel axis are typical of the late (but before the plasma starts to recombine) stages of the capillary discharge dynamics. Since the plasma dynamics in the capillaries show very complicated dependence on the wall material, the plasma composition inside the channel, and the parameters of the external electric circuit [15, 16], Bobrova *et al.* carried out a special investigation of the dynamics of such discharges. One of the main objectives of our study is to optimize the parameters of capillary discharges that can be used to guide laser pulses.

The quality of a plasma waveguide can be characterized by the ratio

$$h = \frac{n_e(r = r_w) - n_e(r = 0)}{n_e(r = 0)}, \quad (3)$$

where $n_e(r_w)$ is the electron density at the boundary of the region in which an electromagnetic wave is localized and $n_e(r = 0)$ is the electron density at the capillary axis. In experiments [13], h was apparently no higher than several percent, because, for a nearly parabolic electron density profile (which increases markedly near the capillary wall), the diameter of the region where the electromagnetic energy is localized was almost one order of magnitude smaller than that of the capillary channel. In investigating capillary discharge dynamics numerically, Bobrova *et al.* [17] were faced with a similar situation. For plasma waveguides with a small relative depth of the plasma density well, the nonlinear effects are insignificant if $a^2 < h$, where $a = eE/m_e\omega_0 c$ is the dimensionless wave amplitude. That is why we need to study how to increase the value of h for plasma waveguides in capillary discharges.

One of the possible ways to increase the parameter h is to use the radial inhomogeneity of the discharge plasma composition. Such an inhomogeneity is typical of discharges in capillary channels prefilled with a plasma whose elementary composition differs from that of the capillary wall. In the course of ablation and ionization of the wall material [15, 16], a cylindrical boundary forms between the initial and ablated plasmas. In the absence of diffusion, this boundary can be regarded as a contact discontinuity. Changing the composition of the gas that originally fills the capillary channel, the gas density, and other discharge parameters makes it possible to control both the radial position of the contact discontinuity inside the channel and the ratio between the electron densities on both sides of the discontinuity.

Let us estimate this ratio under the natural assumption that the pressure and the electron and ion temperatures, T_e and T_i, are all continuous at the discontinuity. As will be shown below, this situation is typical of the capillary discharges under consideration, because they develop on time scales long enough for local dynamic and thermal (due to heat conduction) equilibria to establish. Let us denote the degree of ionization on both sides of the contact discontinuity by z_1 and z_2 (subscripts 1 and 2 will refer to the physical quantities on different sides of the discontinuity). At the discontinuity, the pressure balance condition can be written as

$$z_1 n_{i1} T_e + n_{i1} T_i = z_2 n_{i2} T_e + n_{i2} T_i, \quad (4)$$

and the electron densities on both sides of the discontinuity are equal to

$$n_{em} = z_m n_{im} \quad (m = 1, 2). \quad (5)$$

Let the subscript 1 refer to the quantities on the inner side of the discontinuity. Then, the above formulas yield the following estimate of h:

$$h = \frac{z_2/z_1 - 1}{z_2(T_e/T_i) + 1}. \quad (6)$$

For example, for $z_1 = 1$ (a capillary channel is prefilled with pure deuterium), $z_2 = 3$, and $T_e = T_i$, we have $h = 50\%$. Increasing T_i/T_e in this example to 2 gives $h = 80\%$. Both of these values are much higher than those attained in capillary discharges in which the effect of the plasma-composition homogeneity was not used.

3. PHYSICAL MODEL

The physical process that has a major impact on the dynamics of the capillary plasma is the ablation of the wall material under the heat flux from the plasma to the wall. The ablated material, being heated and ionized, forms a plasma with high electrical conductivity, which leads to a significant redistribution of the electric current between the plasma that initially fills the capillary channel and the ablated plasma. In our model, the channel can be prefilled with either ionized or nonionized gas and the discharge plasma may contain both ionized and nonionized components. We study the dynamics of a capillary discharge using the two-temperature one-fluid MHD model in a one-dimensional approximation, which is natural due to the large length-to-radius ratio of the capillary channel.

The set of dissipative MHD equations used here was described in our previous papers [15, 16]. Here, we only present the assumptions under which they were derived. We take into account all dissipative processes in both ion and electron plasma components, in particular, the Nernst and Ettinghausen effects. The expressions for the dissipative coefficients and the rate of heat transfer between ions and electrons were taken from [18], where the familiar set of Braginskii equations [19] was generalized to the case of a plasma with a large mean charge number of ions. As in [18], we take into account the difference between the Coulomb logarithms λ_{ee} and λ_{ei} for electron–electron and electron–ion collisions, respectively, and the contribution of neutral atoms to the electron–ion collision frequency at low temperatures when $z < 1$.

The ion plasma component is assumed to be unmagnetized. In the equation of state and the equation for the degree of ionization, the approximation of local thermodynamic equilibrium is used separately for the electron and ion components. For the mean ion charge number $z > 1$, the ionization state is determined from the Raizer approximation and the mean-ion model. For $1 < z < Z/2$, where Z is the atomic number of the chemical element under consideration, the average ionization potential is determined from the Sommerfeld formula in the Thomas–Fermi model for an ion shell. For $Z/2 \le z \le Z - 1$, the formula for the hydrogen-like ionization potential with allowance for the screening of the ion electric field by $(Z - z - 1)$ electrons is used. The hydrodynamic description can be applied to a nonisothermal plasma only when the electron density is not too low. Consequently, we restrict ourselves to considering plasmas in which the degree of ionization z exceeds a certain value z_0. The simulations reported below were carried out with $z_0 = 10^{-6}$. In the range $z_0 \le z \le 1$, we used the simplified Saha formula that takes into account only neutral and singly ionized atoms. The free electron gas was assumed to be ideal.

The radiation energy losses were described using a simple model in which the Rosseland mean free path, corresponding to absorption due to bremsstrahlung and photoionization, was estimated from the Zel'dovich–Raizer formula [20].

In simulations of plasma–wall interaction, the wall material was regarded as a cold high-density neutral gas. We assumed that the specific heat of evaporation of the wall material is much less than the specific internal energy of the plasma inside the channel. In the region of neutral gas (where the density is high and the temperature is low), the plasma electric conductivity was assumed to be negligible. Unlike in [15, 16], the basic set of equations used here accounts for the effects of ion heat conduction.

Electron density fluctuations driven by possible MHD instabilities can break the regular structure of a plasma wave excited by a laser pulse and can prevent a proper acceleration process. Consequently, it is necessary to consider such dynamic regimes of the discharge that are free of MHD instabilities. Let us describe one way of suppressing MHD instabilities in a well-conducting capillary discharge. Various MHD instabilities are known to disrupt classical Z-pinches after the first compression. At the same time, a sufficiently symmetric first compression is achievable in many experiments. We expect that the capillary discharge is free of MHD instabilities for the regimes in which the electric current in the plasma has already decayed after the first plasma compression. In this case, the plasma density profile can remain parabolic. Such a dynamic regime of the capillary discharge can be attained by switching off the electric current at a certain time. Note that Z-pinches are stable during the first compression and the following expansion up to the time at which the pinch radius becomes maximum. Consequently, if the electric current is switched off during the plasma expansion, after the shock wave has converged on the axis, then no MHD instabilities will occur. Even if MHD instabilities have developed during the current pulse, they are damped after the pulse is switched off. For the current pulse to be aperiodic, the external electric circuit formed by the capacity of the source, C, and

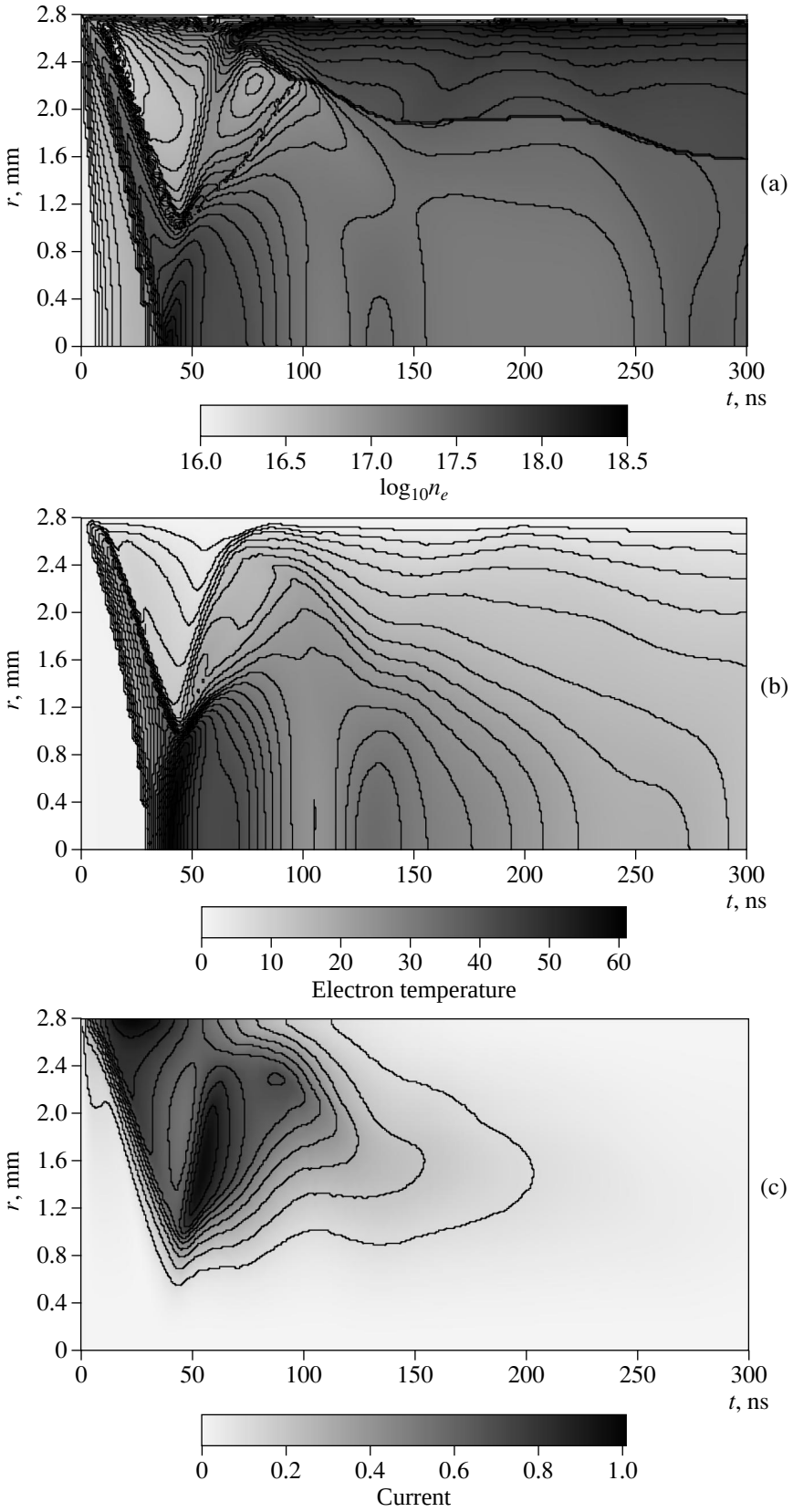

Fig. 1. Results from numerical simulation of the dynamics of a capillary discharge in a channel with a diameter of 5.6 mm prefilled with deuterium at a density of 3.5×10^{-7} g/cm^3 for the discharge current amplitude $I_0 = 30$ kA and characteristic decay time of the current $t_0 = 23$ ns: (a) contours of the decimal logarithm of the electron density (expressed in cm^{-3}), (b) contours of the electron temperature (expressed in eV), and (c) contours of the electric current flowing inside a region of radius r (in units of I_0).

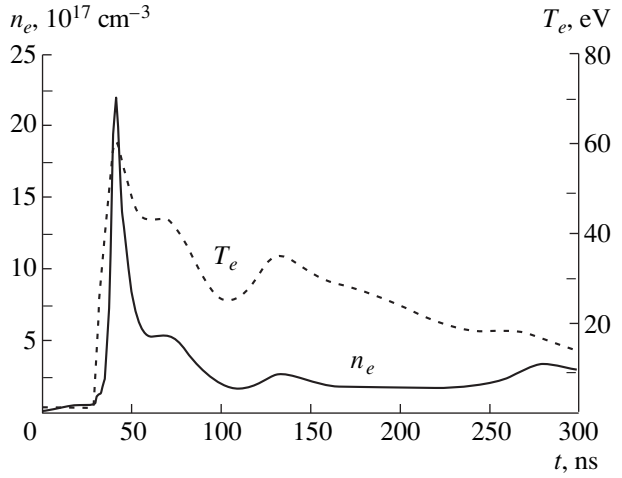

Fig. 2. Time evolution of the electron density n_e and electron temperature T_e at the channel axis for the same discharge parameters as in Fig. 1.

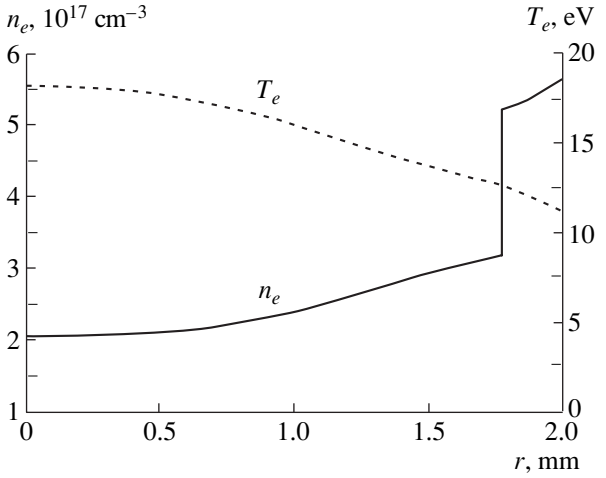

Fig. 3. Radial profiles of the electron density n_e and electron temperature T_e at t = 250 ns for the same discharge parameters as in Fig. 1.

the inductance of the circuit itself, L, should be supplemented by the resistance

$$R = 2(L/C)^{1/2}, \tag{7}$$

in which case the current pulse is shaped as

$$I(t) \propto te^{-t/t_0}, \tag{8}$$

where $t_0 = (LC)^{1/2} = t_{1/2}/\pi$ and $t_{1/2}$ is the half-period of the current pulse in the absence of Ohmic resistance.

To describe the dynamics of a capillary discharge, we introduce the dimensionless parameter

$$\frac{t_c}{t_0} = \frac{(\pi\rho_0)^{1/2} cR_0^2}{I_0 t_0}, \tag{9}$$

where t_c is the time for which the shock wave reaches the channel axis. This parameter represents the ratio of the typical plasma time scale to the characteristic time of the external electric circuit [16]. The shock wave velocity in the channel should be on the order of the Alfvén speed, $v_A = B/(4\pi\rho_0)^{1/2}$, where the magnetic field is $B = 2I_0/cr_0$. For a constant value of t_c/t_0, the trajectories of plasma elements in the $(r–t)$ plane are found to be self-similar. MHD simulations [16] showed that the dynamics of shock waves in different capillary discharges with the same value of t_c/t_0 remain the same. This indicates that, under the condition $t_c/t_0 \sim 1$, the plasma in experimental devices with parameters similar to those considered below should be free of MHD instabilities. We also chose the pulse to be short enough so that MHD instabilities have no time to develop. Then, after switching off the electric current, the plasma remains stable. Below, we assume that the parameter t_c/t_0 is constant. After switching off the current, the capillary plasma is slowly cooled by the surrounding cold ablated plasma, so that the typical plasma density and temperature profiles with a nearly constant pressure will be established.

4. CHANNELS WITH A PARABOLIC DENSITY PROFILE

We carried out an extensive series of simulations of capillary discharges prefilled with deuterium in order to determine conditions that are close to the optimum ones and ensure the formation of waveguides for the guiding of laser pulses with wavelengths on the order of 1 and 10 μm. In presenting the numerical results, we start with the regimes in which the jump in the electron density at a contact discontinuity separating the deuterium plasma from the ablated plasma lies far beyond the region of radius r_w [see (2)], where electromagnetic radiation is localized. Numerical simulations of the discharge dynamics in a deuterium-filled capillary channel allows us to optimize the electron density at the channel axis and the radius r_w of the region in which an electromagnetic wave is localized. A capillary channel was filled with preionized deuterium at a uniform density and temperature. The dimensionless parameter t_c/t_0 in (9) was set to be on the order of unity. Note that filling the channel with hydrogen or deuterium is preferable, because the energy losses through gas ionization do not cause laser pulse depletion, although, in such channels, the condition $t_c/t_0 \sim 1$ is far more difficult to satisfy.

In the version of a CO_2 laser, the channel radius was R_0 = 2.8 mm, the initial deuterium density was $\rho_0 = 3.5 \times 10^{-7}$ g/cm^3, and the electron temperature was 1.0 eV. The capillary walls were made of polyacetal ($(CH_2O)_n$). The wall material was modeled by a gas with the mean atomic number Z = 7, mean mass number A = 14, and initial density ρ_0 = 1 g/cm^3. The electric

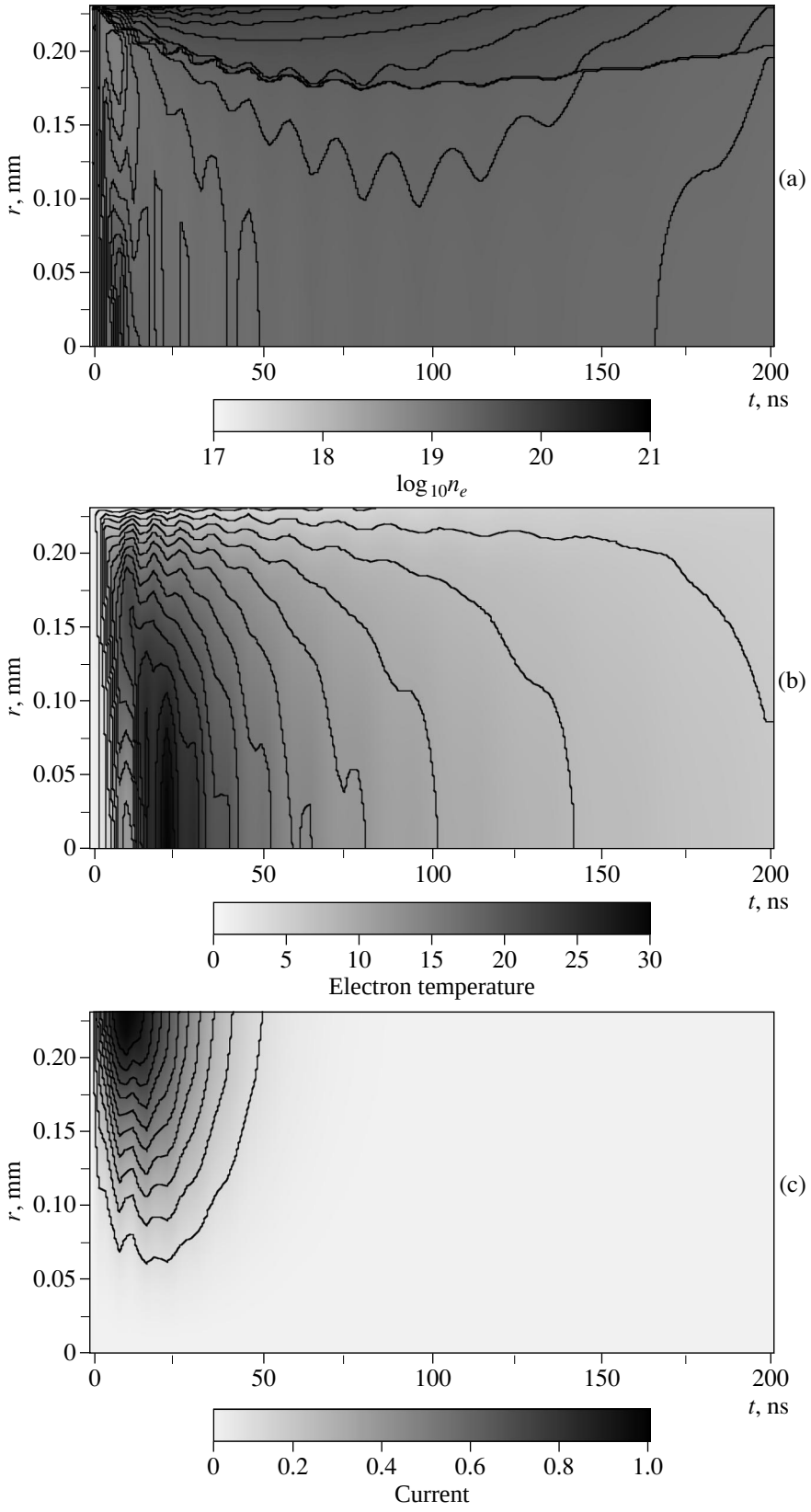

Fig. 4. Results from numerical simulation of the dynamics of a capillary discharge in a channel with a diameter of 0.46 mm prefilled with deuterium at a density of 4.5×10^{-5} g/cm^3 for the current amplitude $I_0 = 10$ kA and $t_0 = 10$ ns: (a) contours of the decimal logarithm of the electron density (expressed in cm^{-3}), (b) contours of the electron temperature (expressed in eV), and (c) contours of the electric current flowing inside a region of radius r (in units of I_0).

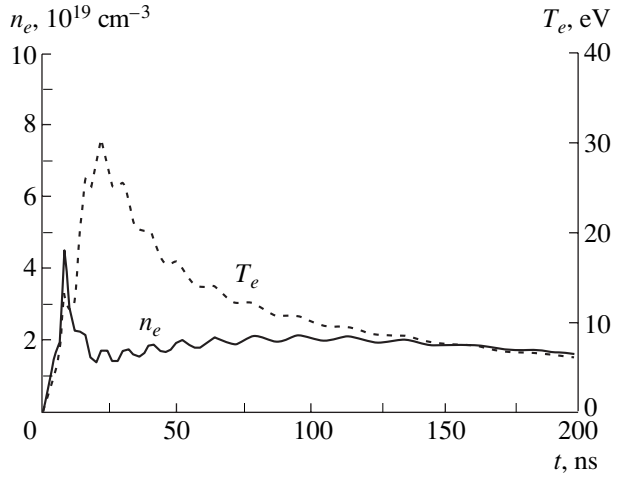

Fig. 5. Time evolution of the electron density n_e and electron temperature T_e at the channel axis for the same discharge parameters as in Fig. 4.

current amplitude in the external circuit was $I_0 = 30$ kA, the characteristic decay time t_0 of the discharge current being 23 ns.

In Fig. 1, the evolution of the capillary discharge is shown. Figures 1a and 1b present contours of the decimal logarithm of the electron density and contours of the electron temperature, respectively, and Fig. 1c presents contours of the electric current flowing inside a region of radius r. In the first stage (about 100 ns), the capillary plasma experiences relaxation oscillations accompanied by the ablation and ionization of the wall material. Then, the plasma density and temperature approach their quasisteady profiles and the plasma experiences residual small-amplitude acoustic oscillations. A contact discontinuity separating the deuterium plasma that initially fills the capillary channel from the plasma that is produced via ablation of the capillary wall material is distinctly seen in Fig. 1a. Originally, the discontinuity travels immediately behind the shock front. After the shock wave has been reflected from the channel axis, the contact discontinuity stops converging at a distance of about 1 mm from the axis and, then, starts to expand toward the capillary wall. At the time $t \approx 100$ ns, the plasma ablated from the wall causes the discontinuity to reverse direction: it starts to converge slowly toward the axis. Near the capillary walls, the electron density decreases, because the temperature and the degree of ionization of the wall plasma both fall off and its mass density grows toward the wall. After the time $t = 100$ ns, the electric current vanishes and the capillary plasma can be regarded as being in quasi-equilibrium. Figure 2 shows the time evolution of the electron density and electron temperature at the channel axis. The electron density is seen to be nearly constant at the axis for about 100 ns after the time $t = 150$ ns, and the electron temperature decreases slowly. Note that, for the electron density and electron temperature to evolve in such a smooth fashion, the governing characteristics of the current pulse, channel radius, and initial gas density in the channel should be adjusted accordingly. If these parameters were chosen inconsistently, we observed relaxation oscillations in the course of which the plasma density and plasma temperature changed precisely on the time scale required for the shock wave to propagate over a distance of about the channel radius. In this case, the plasma density might change by an order of magnitude. Since the characteristic time required for a laser pulse to traverse a distance of about 10 cm (the supposed length of the channel) is 3 ns, we can assume that, as the pulse propagates through the plasma, the plasma distribution inside the channel is quasisteady. Consequently, such channels can also be used to guide laser pulses. However, the properties of the excited wake field will be very sensitive to the stage at which the laser pulse enters the channel, which is difficult to predict. This circumstance is unfavorable for LWFA operation. Hence, the parameters of capillary discharges should be adjusted in a proper manner in order to avoid undesirable dynamic regimes with relaxation oscillations.

Figure 3 shows radial profiles of the electron density and electron temperature at the time $t = 250$ ns. The electron temperature is seen to decrease gradually from the channel axis toward the wall. A contact discontinuity between deuterium and ablated plasmas is at a distance $r = 1.8$ mm from the axis. In a deuterium plasma, the electron density profile is parabolic, with a minimum ($n_e = 2.0 \times 10^{17}$ cm^{-3}) at the center. The radius of the region in which electromagnetic radiation is localized is $r_w = 170$ μm [see (2)] and the electron temperature is $T_e = 18$ eV. We emphasize that r_w is a function of the time-dependent quantity $n_e'' R_0^2 / n_e$. In these simulations, the quantity $n_e'' R_0^2 / n_e$ is on the order of unity and there exists the time interval (≈50 ns) within which it changes insignificantly.

Now, we turn to the description of the results of simulations for the guiding of 1-μm laser pulses in capillary discharges. This series of numerical experiments was carried out with the channel radius $R_0 = 0.23$ mm, initial deuterium density $\rho_0 = 4.5 \times 10^{-5}$ g/cm^3, and electron temperature 1.0 eV. The electric current in the external electric circuit was computed from equation (8) with $I_0 = 10$ kA and $t_0 = 10$ ns.

Figure 4 illustrates the results from tracing the evolution of a capillary discharge numerically. The time over which the shock wave converges to the discharge axis and then is reflected from it is fairly short. Thereafter, the plasma column experiences oscillations, which are damped as time elapses. After the time $t = 100$ ns, the plasma is in quasi-equilibrium and the electron density and electron temperature slowly decrease. From Fig. 4c, we can see that, in this stage, no current flows in the plasma. A contact discontinuity between

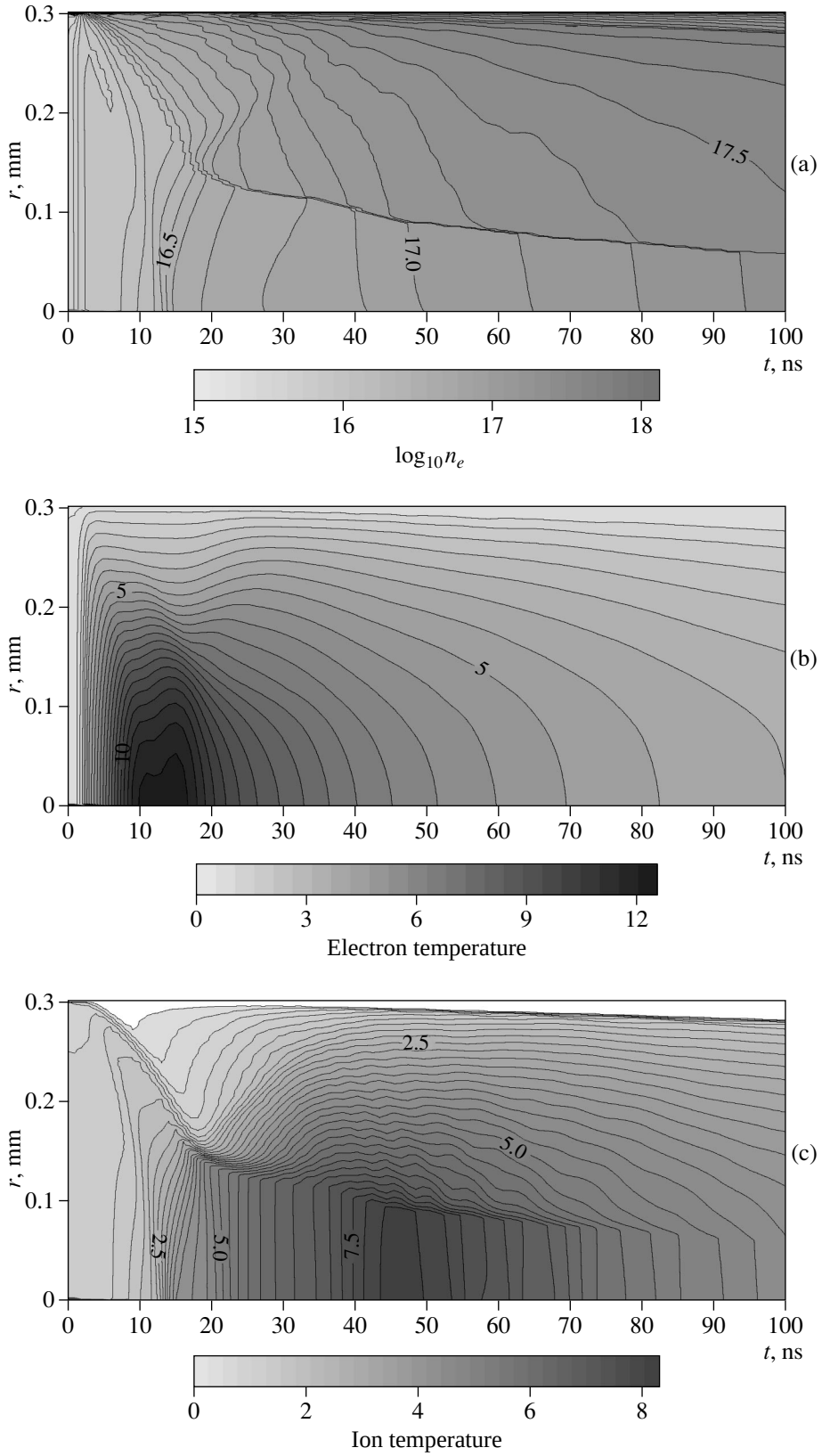

Fig. 6. Results from numerical simulation of the dynamics of a capillary discharge in a channel with a diameter of 0.6 mm prefilled with deuterium at a density of 3.5×10^{-8} g/cm^3 for the current amplitude $I_0 = 0.3$ kA and $t_0 = 20$ ns: (a) contours of the decimal logarithm of the electron density (expressed in cm^{-3}), (b) contours of the electron temperature (expressed in eV), and (c) contours of the ion temperature (expressed in eV).

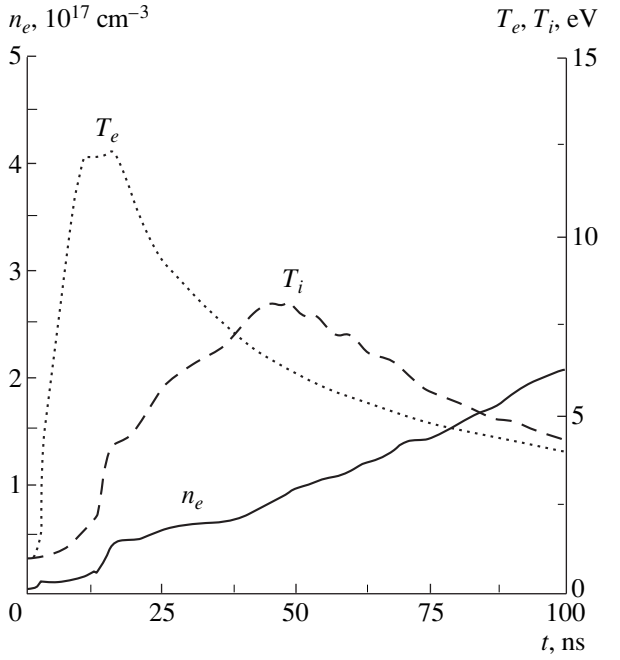

Fig. 7. Time evolution of the electron density n_e and electron and ion temperatures, T_e and T_i, at the channel axis for the same discharge parameters as in Fig. 6.

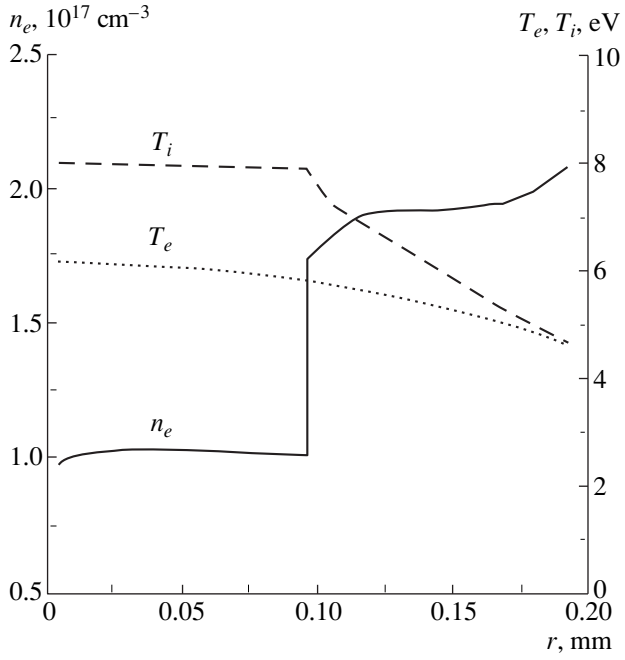

Fig. 8. Radial profiles of the electron density n_e and electron and ion temperatures, T_e and T_i, at t = 50 ns for the same discharge parameters as in Fig. 6.

deuterium and ablated plasmas stays near the capillary wall, without being displaced toward the center. This indicates that, after the transient process has come to an end, the ablation of the wall material stops almost completely. Figure 5 shows the time evolution of the electron density and electron temperature at the channel axis. At the time t = 100 ns, the electron density profile is parabolic, with a minimum ($n_e = 2.0 \times 10^{19}$ cm^{-3}) at the axis. The radius of the region where electromagnetic radiation is localized is r_w = 20 μm and the electron temperature is T_e = 10 eV.

5. IMPROVEMENT OF THE PARAMETERS OF A PLASMA WAVEGUIDE BY MEANS OF THE RADIAL INHOMOGENEITY OF THE PLASMA COMPOSITION IN A CAPILLARY DISCHARGE

We also simulated the dynamics of capillary discharges with the purpose of forming a plasma waveguide at the expense of a jump in the electron density at a contact discontinuity rather than due to a parabolic electron density profile near the discharge axis. Let us consider the dynamics of a capillary discharge in a channel with a diameter of 0.6 mm prefilled with deuterium at a density of 3.5×10^{-8} g/cm^3, the initial plasma temperature being $T_i = T_e$ = 1 eV. The electric current amplitude in the external circuit was I_0 = 0.3 kA and the characteristic decay time of the discharge current was 20 ns.

The results from simulating the evolution of this discharge are illustrated in Fig. 6, which shows contours of the decimal logarithm of the electron density (Fig. 6a) and contours of the electron and ion temperatures (Figs. 6b, 6c). We can see that a weak shock wave converges from the capillary wall toward the discharge axis, is reflected from an axial region at the time of about t = 15 ns, and then starts to expand. A contact discontinuity between deuterium and ablated plasmas, which is clearly seen in Figs. 6a and 6c, initially travels behind the shock front. After the discontinuity has met the expanding shock front, it continues to move inward but at a lower speed. After the time t = 50 ns, the electric current in the external circuit vanishes and the capillary plasma can be assumed to be in quasi-equilibrium. In this case, the contact discontinuity converges very slowly toward the center. Figure 7 shows the time evolution of the electron density and the electron and ion temperatures at the discharge axis. After t = 50 ns, the central electron density is seen to grow slowly: it doubles over 50 ns. The central electron temperature becomes maximum at the time at which the shock wave arrives at the axis. Then, the electron temperature decreases and, after t = 50 ns, it changes only slightly. As the shock wave is reflected from the axis, the central ion temperature grows very rapidly. It continues to grow after the reflected shock wave has passed and becomes maximum at t = 50 ns. Then, the ion temperature starts to fall off slowly. Note that, after the electric current has been damped, the difference between the electron and ion temperatures at the channel axis becomes maximum at about t = 50 ns. Figure 8 shows

radial profiles of the electron density and the electron and ion temperatures at $t = 50$ ns. A contact discontinuity between deuterium and ablated plasmas is seen to lie at a distance $r = 0.1$ mm from the channel axis. The electron density in a deuterium plasma is nearly constant and is equal to $n_e = 1.0 \times 10^{17}$ cm^{-3}. The radius of the region where electromagnetic radiation is localized is $r_w = 100$ μm, which coincides with the distance from the axis to the discontinuity. At $t = 50$ ns, the electron density at the discontinuity is higher than that at the axis by $h = 75\%$. The electron temperature decreases gradually from the axis toward the wall, being nearly constant in the region between the axis and the discontinuity. The ion temperature is constant inside the channel formed by the contact discontinuity, and, outside the channel, it falls off. Note that the radial profile of the ion temperature has a break at the discontinuity.

This example of the dynamic regime of a capillary discharge shows that the radial inhomogeneity of the discharge plasma composition may serve as a means for forming higher quality plasma waveguides in the axial regions.

6. CONCLUSION

We have investigated the dynamics of capillary discharges using a one-dimensional MHD code in order to predict optimum regimes for the guiding of ultrashort intense laser pulses.

We have revealed a dynamic regime in which the discharge plasma is in dynamic and thermal equilibrium after the termination of a short transient process. In the initial stage, the plasma is rapidly compressed (pinched) and a shock wave is reflected from the discharge axis. After this transient process has come to an end (when all of the MHD instabilities have been damped), the plasma is in dynamic and thermal quasi-equilibrium and is slowly cooled off. In this stage, the electric current and Ampére force are both equal to zero. Inside the channel, the plasma pressure is uniform and the electron density profile is parabolic with a minimum at the axis, where the plasma temperature is maximum.

Since such a plasma configuration is stable against MHD modes, small perturbations of the plasma density are damped. Consequently, we have shown that, in capillary discharges, it is possible to achieve conditions that are optimum for the guiding of ultrashort intense laser pulses. In a certain range of the parameters of a capillary discharge, laser pulses can be guided in a region whose transverse dimension is about ten wavelengths of the laser light.

One way of improving the focusing properties of plasma waveguides is to exploit the radial inhomogeneity of the discharge plasma composition. Such discharges can be initiated in a capillary channel prefilled with a plasma whose elementary composition differs from that of the material of the capillary wall. The radius of the region in which electromagnetic radiation is localized is governed by a contact discontinuity between the plasma that initially fills the capillary channel and the plasma ablated from its wall. The example we have investigated shows that laser pulses can be guided in a cylindrical region whose transverse dimension is governed by the position of a contact discontinuity and was found to be 100 μm for CO_2 lasers.

ACKNOWLEDGMENTS

We are grateful to T. Tajima for fruitful discussions. This work was supported by the Russian Foundation for Basic Research, project no. 96-02-16125.

REFERENCES

1. C. J. Joshi and P. B. Corkum, Phys. Today **48** (1), 36 (1995).
2. G. A. Mourou, C. P. J. Barty, and M. D. Perry, Phys. Today **51** (1), 22 (1998).
3. T. Tajima and J. M. Dawson, Phys. Rev. Lett. **43**, 267 (1979).
4. E. Esarey, P. Sprangle, J. Krall, and A. Ting, IEEE Trans. Plasma Sci. **24**, 252 (1996).
5. A. Modena, Z. J. Najmudin, A. E. Dangor, *et al.*, Nature (London) **337**, 606 (1995); K. Nakajima, D. Fisher, T. Kawakubo, *et al.*, Phys. Rev. Lett. **74**, 4428 (1995).
6. P. Sprangle, E. Esarey, A. Ting, and G. Joyce, Appl. Phys. Lett. **53**, 246 (1988); L. M. Gorbunov and V. I. Kirsanov, Zh. Éksp. Teor. Fiz. **93**, 509 (1987) [Sov. Phys. JETP **66**, 290 (1987)]; E. Esarey, P. Sprangle, and J. Krall, Phys. Fluids B **5**, 2690 (1993).
7. S. V. Bulanov, V. I. Kirsanov, F. Pegoraro, and A. S. Sakharov, Laser Phys. **6**, 1078 (1993); S. V. Bulanov, V. A. Vshivkov, G. I. Dudnikova, *et al.*, Fiz. Plazmy **23**, 284 (1997) [Plasma Phys. Rep. **23**, 259 (1997)].
8. C. E. Max, J. Arons, and A. B. Langdon, Phys. Rev. Lett. **33**, 209 (1974); G. Z. Sun, E. Ott, Y. C. Lee, and P. Guzdar, Phys. Fluids **30**, 526 (1987).
9. A. B. Borisov, A. V. Borovskij, V. V. Korobkin, *et al.*, Phys. Rev. Lett. **68**, 2309 (1992); C. Durfree, III and H. Milchberg, Phys. Rev. Lett. **71**, 2409 (1993).
10. T. Tajima, Laser Part. Beams **3**, 1432 (1985); P. Sprangle, E. Esarey, and A. Ting, Phys. Rev. A **41**, 4463 (1990); S. V. Bulanov, F. F. Kamenets, F. Pegoraro, and A. M. Pukhov, Phys. Lett. A **195**, 84 (1994); C. Durfree, III, J. Lynch, and H. Milchberg, Phys. Rev. E **51**, 2368 (1995); T. C. Chiou, T. Katsouleas, C. D. Decker, *et al.*, Phys. Plasmas **2**, 310 (1995).
11. R. Wagner, S.-Y. Chen, A. Maksimchuk, and D. Umstadter, Phys. Rev. Lett. **78**, 3125 (1997).
12. S. V. Bulanov, T. Zh. Esirkepov, N. M. Naumova, *et al.*, IEEE Trans. Plasma Sci. **24**, 393 (1996).
13. Y. Ehrlich, C. Cohen, A. Zigler, *et al.*, Phys. Rev. Lett. **77**, 4186 (1996).
14. I. V. Pogorelsky, A. Van Steenbergen, R. Fernow, *et al.*, in *Proceedings of VII Workshop on Advanced Accelerator Concepts, Lake Tahoe, CA, 1996*, paper BNL-63649.

15. N. A. Bobrova, S. V. Bulanov, T. L. Razinkova, and P. V. Sasorov, Fiz. Plazmy **22**, 387 (1996) [Plasma Phys. Rep. **22**, 349 (1996)].
16. N. A. Bobrova, S. V. Bulanov, R. Pozzoli, *et al.*, Fiz. Plazmy **24**, 3 (1998) [Plasma Phys. Rep. **24**, 1 (1998)].
17. N. A. Bobrova, S. V. Bulanov, D. Farina, *et al.*, J. Phys. Soc. Jpn. **67**, 3437 (1998).
18. N. A. Bobrova and P. V. Sasorov, Fiz. Plazmy **19**, 789 (1993) [Plasma Phys. Rep. **19**, 409 (1993)].
19. S. I. Braginskii, in *Reviews of Plasma Physics*, Ed. by M. A. Leontovich (Gosatomizdat, Moscow, 1963; Consultants Bureau, New York, 1965), Vol. 1.
20. Ya. B. Zel'dovich and Yu. P. Raizer, *Physics of Shock Waves and High-Temperature Hydrodynamic Phenomena* (Fizmatgiz, Moscow, 1963; Academic, New York, 1966, 1967), Vols. 1 and 2.

Translated by G. V. Shepekina

Plasma Physics Reports, Vol. 26, No. 1, 2000, pp. 21–32. Translated from Fizika Plazmy, Vol. 26, No. 1, 2000, pp. 24–35.

PLASMA DYNAMICS

Three-Temperature Model for the Dynamics of a Plasma Produced by Exploding Metal Wires

G. V. Ivanenkov* and W. Stepniewski**

**Lebedev Institute of Physics, Russian Academy of Sciences, Leninskiĭ pr. 53, Moscow, 117924 Russia*
***Institute of Plasma Physics and Laser Microfusion, Warsaw 49, Hery 23, Poland*

Received April 14, 1998; in final form, June 9, 1999

Abstract—An MHD model of the implosion of a dense hot plasma column is developed. Because of a better description of radiation transport, this model has a higher spatial resolution compared to the previously developed, simpler, two-temperature model. The new model is applied to calculating the load (a single metal wire or an X–pinch, in particular, a heterogeneous corona–core structure with a sharp boundary) of a nanosecond high-voltage generator. An algorithm of the type previously used to solve the problem in the two-temperature model is supplemented by the iteration procedure for calculating the quasisteady radiation under the assumption that the plasma is optically thick. *© 2000 MAIK "Nauka/Interperiodica".*

1. INTRODUCTION

For fifty years, experiments with pinches, which have occupied a prominent place in plasma studies, have generated a lot of rather sophisticated problems. A combination of complicated processes (for many, it is even difficult to make standard physical estimates) allows few analytical solutions and should be studied by numerical methods. The dense-pinch experiments make it especially important to model the implosion of radiating plasma loads in terawatt-power generators.

In [1], we proposed a radiative–collisional MHD model of a hot dense axially symmetric plasma column aimed at calculations of a single exploding wire. The numerical algorithm was based on the simple free-point method developed by D'yachenko [2] and further improved by Jach [3]. This algorithm combines the Euler and Lagrange approaches and, along with a high calculation rate, ensures the possibility of calculating strong deformations, describes well the distortion of free boundaries, and simplifies the multifluid plasma simulation. However, the use of this algorithm is accompanied by the generation of specific numerical instabilities (especially, angular ones). Moreover, the scheme is nonconservative and imposes rather rigid restrictions on the time step. The physical drawback of the model is the assumption that there is complete equilibrium between the plasma electrons and radiation; in an optically thick plasma, this equalizes the temperatures, $T_e = T_\gamma$. At the same time, as will be shown below, even in the inner plasma region, the temperature difference $||T_\gamma - T_{e,i}|$ is comparable with $|T_e - T_i|$. In the outer (transparent) region, the electron–radiation system becomes even farther from equilibrium. As the grid size decreases, the grid transparency increases. As a result, it becomes impossible to use the assumption that photons and electrons are in equilibrium, and a fairly strong smoothing in calculating the fields and the shape of the plasma–vacuum boundary is required. Attempts to eliminate these defects by decreasing the time step in accordance with a decrease in the grid size lead to the faster onset of the $m = 0$ mode of the plasma column instability and an increase in both the maximum temperature of the constrictions and temperature gradients. This is clearly manifested by the increase in the growth rate of instabilities near cold electrodes.

In the model of an exploding wire proposed in this paper, an important factor is the corona–core structure. The need for this modification follows from direct observations of such structures in recent experiments [4, 5], in which the modern method of X-ray backlighting (with an X-pinch used as a small-size source of probing radiation) was employed. In the images of a discharge produced by the explosion of metal wires, a dense and relatively hot core surrounded by a plasma corona (an optically observed plasma column) is clearly seen. The plasma density sharply drops (approximately 100 times) at the core–corona interface, which is typical of liquid–vapor phase transitions [6]. According to [4, 5], the occurrence of such a structure is associated with the specific features of incomplete evaporation of metal during the electric explosion, ending in the boiling of the core [6]. It is also found [7] that, during the interaction of the core with a compression wave arriving from the corona, hydrodynamic instabilities occur at the boundary. Presumably, these are the Rayleigh–Taylor and Richtmeier–Meshkov instabilities. In the above papers, it was noted that the highly nonlinear behavior of these phenomena may be related to the experimentally observed fine structure of hot points emitting X radiation.

1063-780X/00/2601-0021$20.00

2. PHYSICAL MODEL AND NUMERICAL SCHEME

The three-temperature model is based on the axially symmetric equations incorporating the electron and ion temperatures $T_{e,i}$ and the radiation temperature T_γ. These equations generalize the two-temperature model [1] and go over to this model at $T_\gamma = T_e$. The methods described in [1] are used in solving the MHD equations of continuity and motion

$$\frac{dn}{dt} = -n\nabla\cdot\mathbf{v},$$
$$m_i n\frac{d\mathbf{v}}{dt} = -\nabla(p+p_{art}) + \nabla\cdot\mathbf{\Pi} + \frac{1}{c}\mathbf{j}\times\mathbf{B}, \quad (1)$$

where n is the density of ions with the average charge Z, $\mathbf{v}$ is the plasma mass velocity, $p = p_i + p_e$ is the pressure (due to specific features of the difference scheme, the pressure also includes the pressure p_{art} related to the artificial Neuman–Richtmeir viscosity), $\mathbf{\Pi} = \mathbf{\Pi}_i + \mathbf{\Pi}_e$ is the shear-viscosity tensor, and $d/dt = \partial_t + \mathbf{v}\cdot\nabla$ is the substantial derivative. The axial symmetry of the Z-pinch implies that $\mathbf{v}$ and $\mathbf{j}$ have the form $\mathbf{v} = \{v_r, 0, v_z\}$, and the magnetic field is $\mathbf{B} = \{0, B_\theta, 0\} = B\mathbf{e}_\theta$. Note that, because of the large value of Z, we have $\Pi_e/\Pi_i \simeq Z^3\sqrt{m_e/m_i}$; thus, we must incorporate the electron viscosity (which is usually neglected in the case of a low-Z plasma). In practice, this means that we should perform summation of the contributions from particles of both species to three (from five) nontrivial magnetic viscosity coefficients (seemingly, incorporation of the current velocity in $\mathbf{\Pi}_e$ is beyond the accuracy of the model). We also neglect the radiation pressure.

In our new model, the thermal terms are modified. Taking into account the plasma quasineutrality, we can write the heat transport equations in the form[1]

$$C_{ve}Zn\frac{d_eT_e}{dt} + \nabla\cdot\mathbf{q}_e = -p_e\nabla\cdot\mathbf{u}_e + \frac{\mathbf{j}^2}{\sigma} + \mathbf{\Pi}_e:\nabla\mathbf{u}_e$$
$$-n(C_{ve}T_e+\varepsilon_Z)\frac{dZ}{dt} - Q_\gamma - \mathbf{R}\cdot\mathbf{u} - Q_{e-i},$$
$$C_{vi}n\frac{d_iT_i}{dt} + \nabla\cdot\mathbf{q}_i$$
$$= -(p_i+p_{art})\nabla\cdot\mathbf{u}_i + \mathbf{\Pi}_i:\nabla\mathbf{u}_i + Q_{e-i}. \quad (2)$$

Here, $C_{ve,i}$ are the specific heats of electron and ion fluids per particle, $\mathbf{u}_{e,i}$ are the electron and ion velocities related to the mass and current velocities by $\mathbf{v} = \mathbf{u}_i + (Zm_e/m_i)\mathbf{u}_e$ and $\mathbf{u} = \mathbf{u}_e - \mathbf{u}_i = -\mathbf{j}/eZn$; $d_{e,i}/dt = \partial_t + \mathbf{u}_{e,i}\cdot\nabla$ are the substantial derivatives, ε_Z is the interpolated ionization potential as a function of Z, $\mathbf{q}_e = \mathbf{q}_{ue} + \mathbf{q}_{Te}$ and $\mathbf{q}_i = \mathbf{q}_{iT}$ are the heat fluxes, $\mathbf{R} = \mathbf{R}_u + \mathbf{R}_T$ is the sum of the e–i friction force and the thermal force, $Q_{e-i} = 3n(T_e - T_i)/2\tau_{ei}$ is the e–i heat transfer power, and Q_γ is the power of the radiative cooling of electrons. The thermal fluxes and thermal force are

$$\mathbf{q}_{Te,i} = -(\kappa_{\perp e,i}\nabla T_{e,i} + \kappa_{\wedge e,i}\mathbf{e}_\theta\times\nabla T_{e,i}),$$
$$\mathbf{R}_T = -(\alpha_\perp\nabla T_e + \alpha_\wedge\mathbf{e}_\theta\times\nabla T_e),$$

and the drift components are

$$\mathbf{q}_{ue} = [(-C_{pe}/e + \alpha_\perp)\mathbf{j} + \alpha_\wedge\mathbf{e}_\theta\times\mathbf{j}]T_e,$$
$$\mathbf{R}_u = Ze n\mathbf{j}/\sigma.$$

The transport coefficients are taken from [8–10], the classical part of the conductivity (which plays the major role in a dense plasma) is taken from [11], and the anomalous conductivity was the same as in [1]. In the equation of state, we take into account that the ion component is nonideal and incorporate the effects of the quantum degeneration of electrons [12].

The electrodynamic effects are described based on the equation for the magnetic-field generation, which follows from the Maxwell equations (in the quasisteady approximation) and Ohm's law:

$$\mathbf{E} + \frac{1}{c}\mathbf{v}\times\mathbf{B} = \frac{\mathbf{j}}{\sigma} - \frac{1}{Zen}$$
$$\times\left(\nabla p_e - \frac{1}{c}\mathbf{j}\times\mathbf{B} - \nabla\cdot\mathbf{\Pi}_e + \mathbf{R}\right). \quad (3)$$

The resulting equations for the magnetic field are

$$\partial_t\mathbf{B} = \nabla\times\left[\left(\mathbf{v} - \frac{\mathbf{j}}{Zen}\right)\times\mathbf{B} + \frac{c}{Zen}(\nabla p_e - \nabla\cdot\mathbf{\Pi}_e + \mathbf{R})\right],$$
$$\mathbf{j} = \frac{c}{4\pi}\nabla\times\mathbf{B}. \quad (4)$$

The description of radiation is based on the equations for the optically thick medium

$$Q_\gamma \equiv 4\Sigma_{SB}(T_e^4 - T_\gamma^4)/l_P = -\nabla\cdot\kappa_\gamma\nabla T_\gamma, \quad (5)$$

where $\kappa_\gamma = 16\Sigma_{SB}l_R T_\gamma^3/3$ is the radiative heat conductivity and Σ_{SB} is the Stefan–Boltzmann constant. The Planck- and Rosseland-averaged photon mean free paths $l_{P,R}$ are taken from [13], where they were approximated by power law functions of the type

$$1/l\ [\mathrm{cm}^{-1}] = k(T_e\ [\mathrm{eV}])^{s_1}\{(m_i n)\ [\mathrm{g/cm}^3]\}^{s_2}.$$

A detailed description of ionization, excitation, and emission requires a very cumbersome set of equations, which essentially complicates the algorithm; therefore, we used the averaged-ion model, as was done in [1]. This model is based on the solution to the equation for

[1] We draw attention to the misprints in [1]: the thermal-force power in the equation for T_e was erroneously omitted, and the thermal force in the motion equations was written incorrectly. In fact, they were used, as in this paper.

the averaged-charge kinetics

$$\frac{dZ}{dt} = (R_{ion} - R_{phr} - R_{3r})Z, \quad (6)$$

in which the rates of the electron-impact ionization R_{ion}, photorecombination R_{phr}, and three-body recombination R_{3r} were taken from [14]. The ionization energy as a function of Z was obtained by the linear interpolation of the data for free multicharge ions; we also included the correction for the decrease in the ionization threshold and the vanishing of the upper levels under the action of ion microfields (these corrections were taken from [15]).

We assume that, at the sharp free plasma boundary $r = a(z, t)$, the azimuthal components of both the magnetic field $B = 2I/ca$ and the full stress tensor $-p\delta_{ik} + \Pi_{ik} + (B_iB_k - B^2\delta_{ik}/2)/4\pi$ are continuous and the normal components of the heat flux are absent, $\mathbf{n} \cdot \mathbf{q}_{e,i} = 0$. The condition for the emission of radiation into vacuum is

$$-\kappa_\gamma \nabla_n T_\gamma = 2\Sigma_{SB} T_\gamma^4.$$

We note that the assumption of a sharp boundary completely ignores the most rarefied region of the corona, which nevertheless contributes to the current. This allows us to use the adopted simple description of the radiation transport and neglect the current instabilities and generation of the beams of accelerated particles, which are not yet completely understood. To some extent, such an approach corresponds to experiments with preliminary cleaning of the wire surface of impurities [16]. On large time scales, the use of the continuity condition for the full stress tensor also meets difficulties; therefore, at the vacuum boundary, we used a simple condition $p = 0$ (the field B is continuous, and the viscous stress is substantially less than the pressure, because the deformation rates are much lower than the collision frequencies).

We assumed the electrodes to be perfectly conducting rigid plates; the plasma was assumed to flow freely along their surface:

$$v_z = \Pi_{rz} = \Pi_{zz} = E_r = \nabla_z T_\gamma = 0,$$
$$|\nabla_z T_{e,i}| = \max.$$

Here, the subscript max stands for the maximum absolute value of the derivative outside the boundary cells. On the axis, we set standard symmetry conditions

$$v_r = B = \nabla_r T_{e,i,\gamma} = \nabla_r p = 0.$$

For numerical calculations, we used a modification of the algorithm described in [1]. In addition to the technical refinements, we introduce the iteration procedure in order to solve the equation for the radiation temperature. Because the radiation transport processes proceed on time scales much shorter than MHD processes, the simultaneous solution to the time-dependent radiative and hydrodynamic equations meets some difficulties. To overcome them, at each step, we first calculated the contribution from the radiative heat transport assuming that $T_\gamma = T_e$ taken from the previous step; after that, the difference analogue of equation (5) was solved as a linear algebraic system with respect to T_γ^4. From the obtained distribution of the radiation temperature, we found more accurate values of the electron temperature and once again calculated the diffusion term; the process was iterated until the required accuracy was reached. During almost the entire calculation procedure, two to three iterations were made at each time step. A thin layer near the surface in which radiative loss is comparable to surface losses requires special consideration. In this layer, whose thickness is on the order of the photon mean-free-path length, weak absorption of photons arriving from the plasma interior cannot compensate for radiative cooling of electrons; thus, the diffusion approximation used in (5) is violated [17]. However, as was noted in [8], the transparency conditions are less rigid than the requirement for the relative smallness of l_R; therefore, we equated the cross-section-integrated radiation power from the outer layer of thickness D to the diffusion flux on its inner boundary. As is seen in (5), their ratio is characterized by the parameter $\xi = l_P l_R/DL_T$, where $L_T \simeq T_e/|\nabla T_e|$. This allows us to find the position of the boundary at which surface losses begin to dominate over volume losses. Then, we artificially decreased the photon temperature by introducing the factor $(1 + \xi^s)^{-1}$ (where the power index s lies between one and two) before the diffusive term and the source in (5). Thus, Q_γ went over to the expression for the radiative loss in a transparent medium and the convergence of iterations at the boundary between the optically thick and transparent plasma improved. In addition, in equations (5) and (2), we introduced the factors limiting the heat fluxes to their maximum attainable physical values.

Calculations were carried out on both long- and short-size grids. In the first case, a Pentium personal computer was quite sufficient, whereas, in the second case, we needed an Alpha working station. This allowed us to trace the changes in rather complicated algorithm features (that are characteristic of cell schemes) as the spatial resolution was improved. We also attempted to replace the iteration procedure by introducing nonsteady radiation transport; however, we succeeded only with the use of the Alpha station and only for a long-size grid; the decrease in the grid size required an excessive decrease in the time step.

3. SIMULATION OF A DENSE Z-PINCH IN AN EXPLODING-WIRE DISCHARGE

We start with the same problem as in [1]. In the initial state, about 10 ns after the current (which is assumed to be uniform over the wire cross section) has reached 10 kA, we have a cylindrical plasma column 500 μm in diameter, which is formed as a result of the

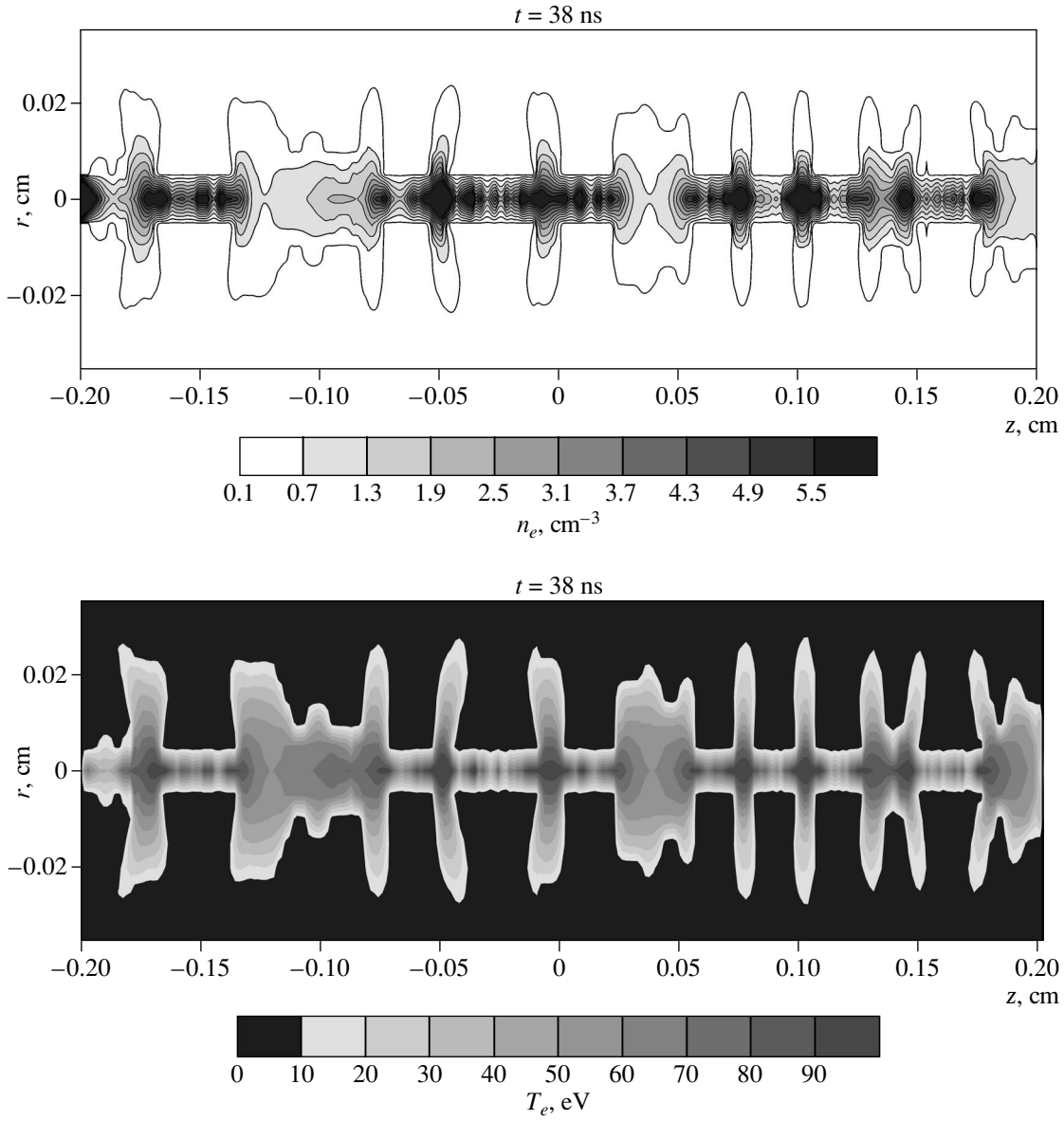

Fig. 1. Example of distributions of the electron density and temperature in the problem without a core.

explosion of a tungsten wire 20 μm in diameter and 4 mm in length. The plasma density decreases with r by a parabolic law and vanishes at the column surface. The plasma particles and radiation have the same initial temperatures ≃2 eV. The seed perturbation for the onset of instability was given in the same way as in [1]—as small (1–3%) random nonuniformities (with a characteristic scale length of 10–100 μm) of the initial distributions of the density and temperature. We calculated the plasma evolution for the sinusoidal discharge current with a 300-kA amplitude and 100-ns half-period.

Qualitatively, the solution did not differ fundamentally from the results of calculations by the two-temperature model [1]. The difference mainly resulted from the decrease in the time step caused by the fact that the radiation and electrons are not in equilibrium. Therefore, we used a shorter size grid, which, on the one hand, increases the resolution of the scheme, but, on the other hand, increases the growth rate of MHD instabilities. As a result, the distributions of thermodynamical parameters obtained differed from those in [1] by larger gradients and the shape of the sharp free boundary was more irregular. The irregular shape of the solution to the three-temperature problem was most pronounced near the electrodes, which were assumed to be cold. Naturally, in this case, the temperature of constrictions was from one-and-a-half to two times higher than that obtained in the two-temperature model and reached the maximum value (150–200 eV) for a shorter time (about 5 ns).

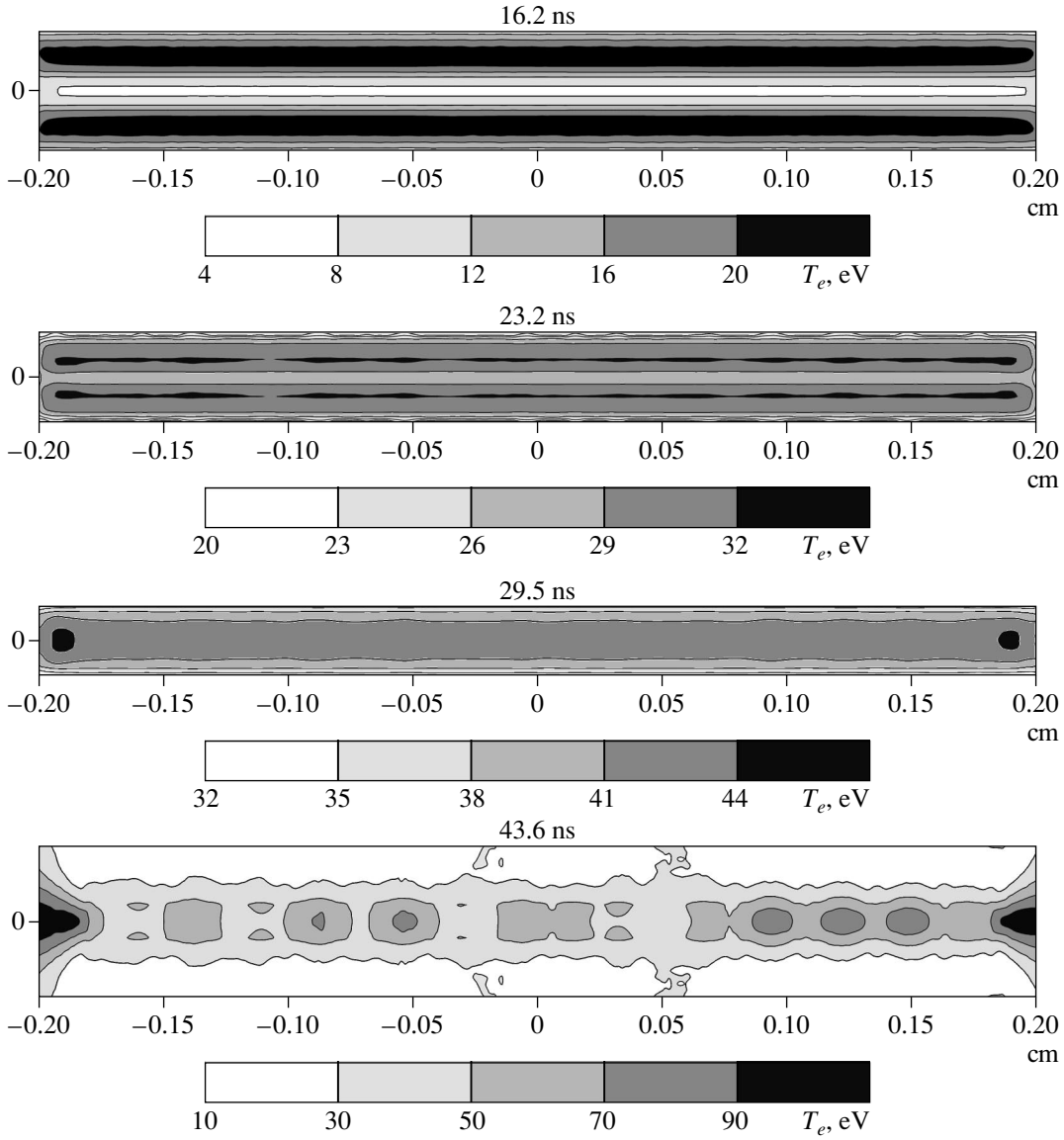

Fig. 2. Time dependence of spatial distributions of the electron temperature in the plasma column with a core.

Figure 1 presents as an example the results of calculations performed for the 31×700 grid. Now, we will go over to the simulation of an explosion of a one-and-a-half times thicker tungsten wire. The model assumes the existence in the initial state of a core from a cold dense substance (a detailed analysis, experimental background, references, as well as the two-temperature version of the solution to the core problem, are presented in [4]). This problem needs the improvement of the model of radiation transport. In order to model the core, we introduced into the initial parabolic distribution a tenfold jumplike increase in the density in the region $\simeq 80$ μm in diameter in the vicinity of the axis. Other parameters were the same. Calculations were carried out on both the long-size (13×299) and short-size (21×500 and 31×700) grids. Further, we will focus on the simpler results obtained for the long-size grid.

The results of calculations are presented in Figs. 2–4. Figure 2 shows the evolution of the electron temperature distribution in the course of plasma heating by the current compressing the plasma. The distributions presented in Fig. 2 refer to the stage of the propagation of an MHD shock toward the axis (16.2 ns), the instant the shock arrives at the corona–core boundary (23.2 ns), the instant of the first compression (29.5 ns), and the subsequent evolution of the constriction (43.6 ns). Complex structures that are finally formed from the constrictions are shown in Fig. 3 at the instant when the current is close to maximum. The specific features of the plasma evolution associated with the introduction of a core into the model were discussed in detail in

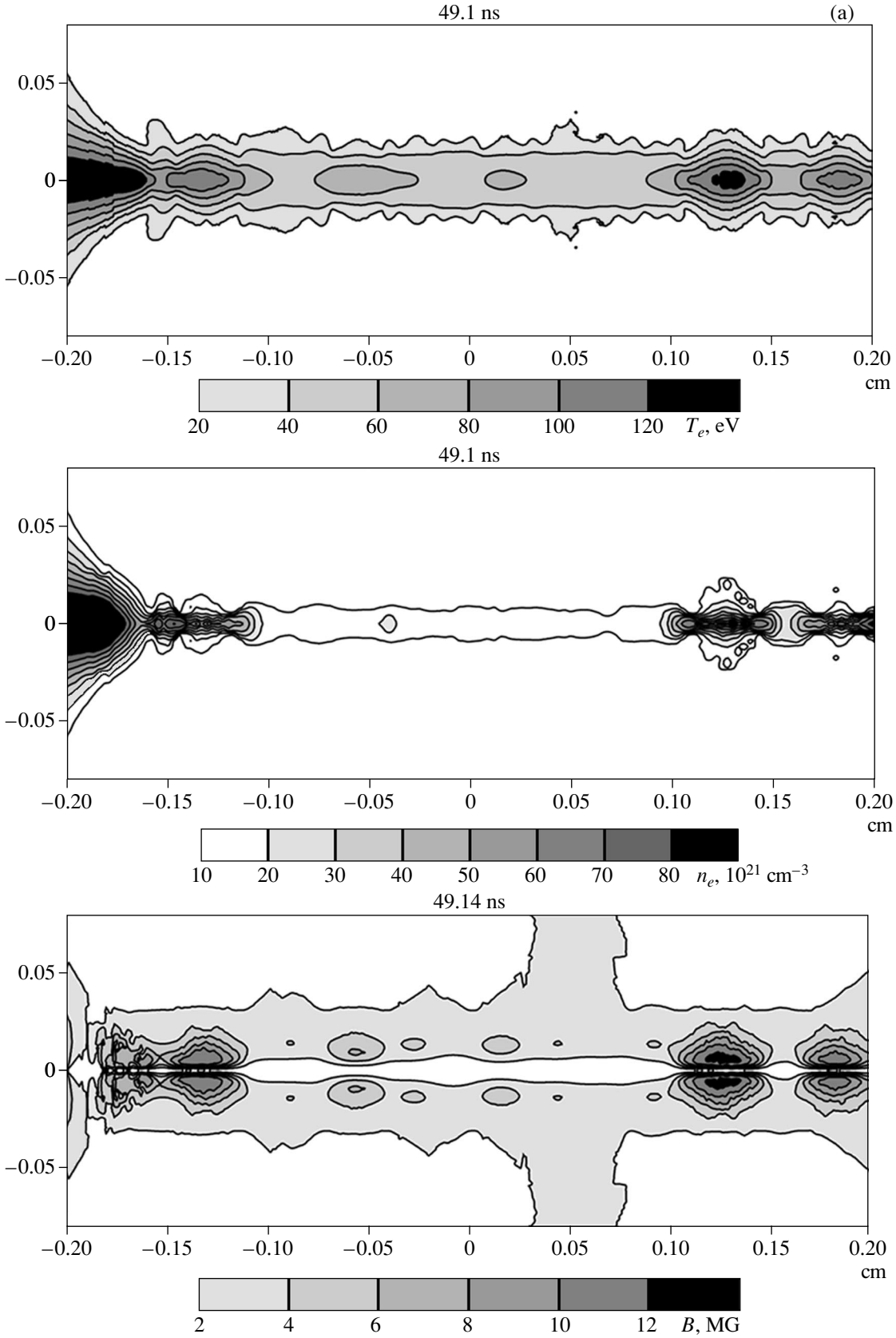

Fig. 3. Distribution of the electron temperature and density and the magnetic field at the final stage of calculation: (a) overall picture and (b) magnified images of the region of the strongest compression.

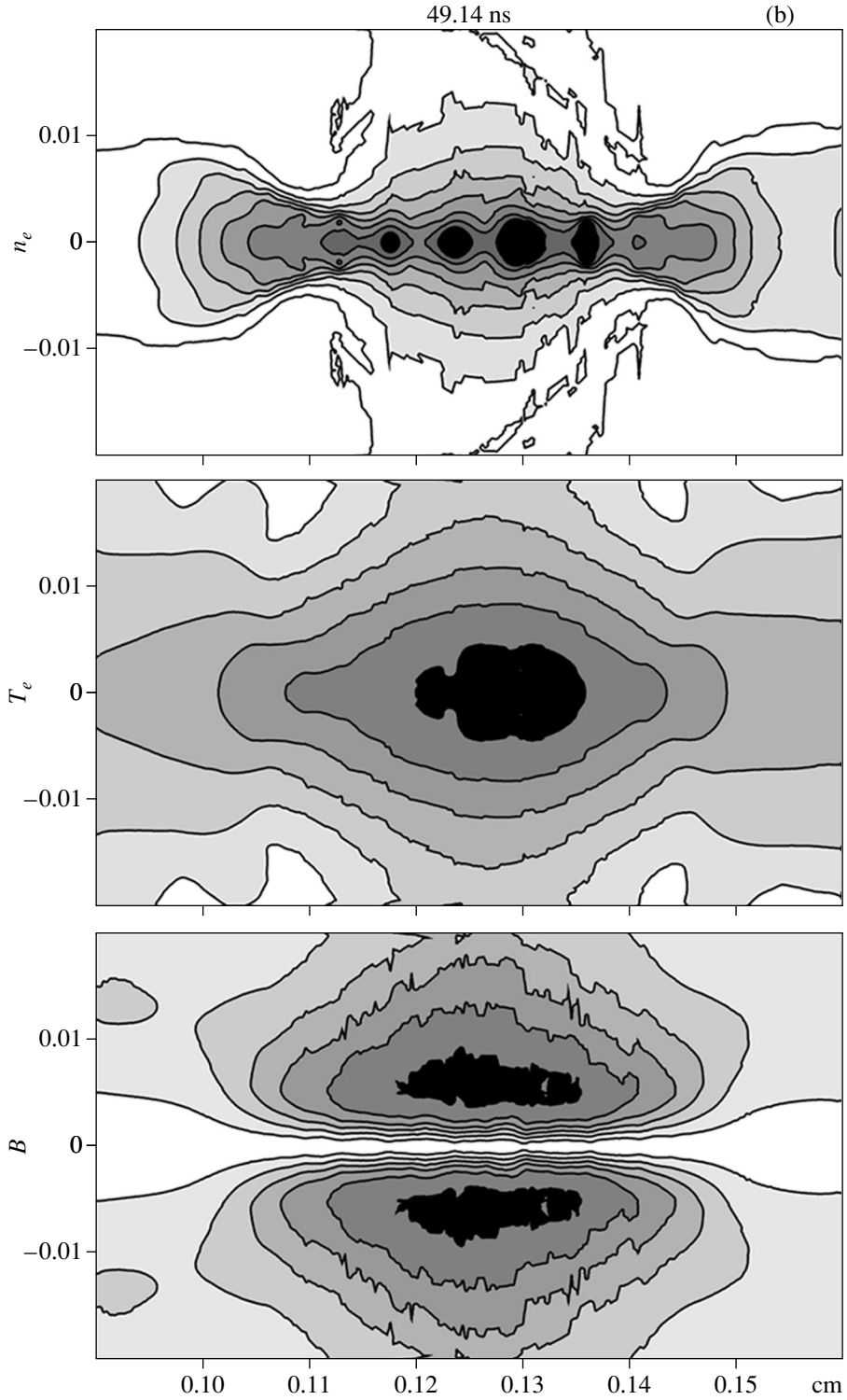

Fig. 3. (Contd.)

[4, 5, 7]. Initially, these features manifest themselves in the low-temperature emission from the core. When the shock front reaches the corona–core boundary, the shock decays into a wave reflected from the core and a compression wave propagating into the core. These two waves are very different: the reflected wave has a broad front and is similar in many respects to the initial corona compression wave, whereas the passed wave

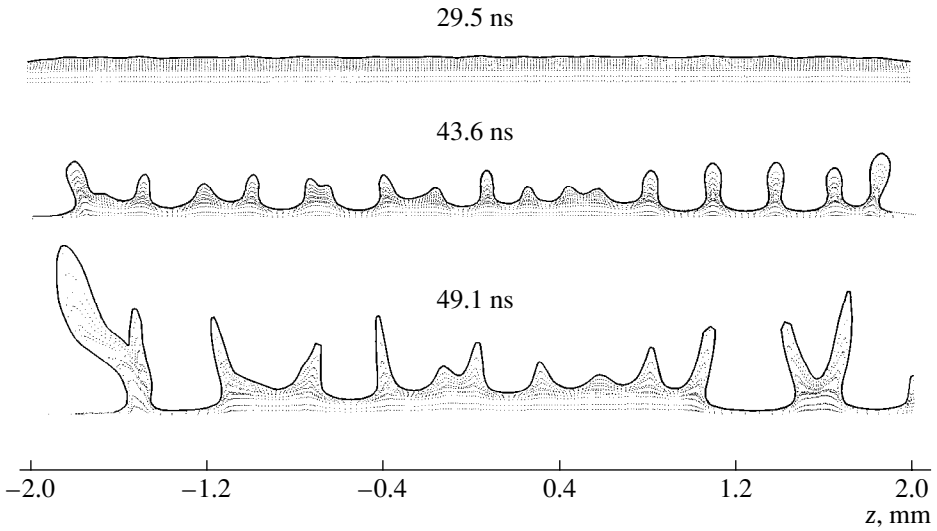

Fig. 4. Behavior of the plasma-column shape and spatial distribution of the calculation points on the 13×299 grid.

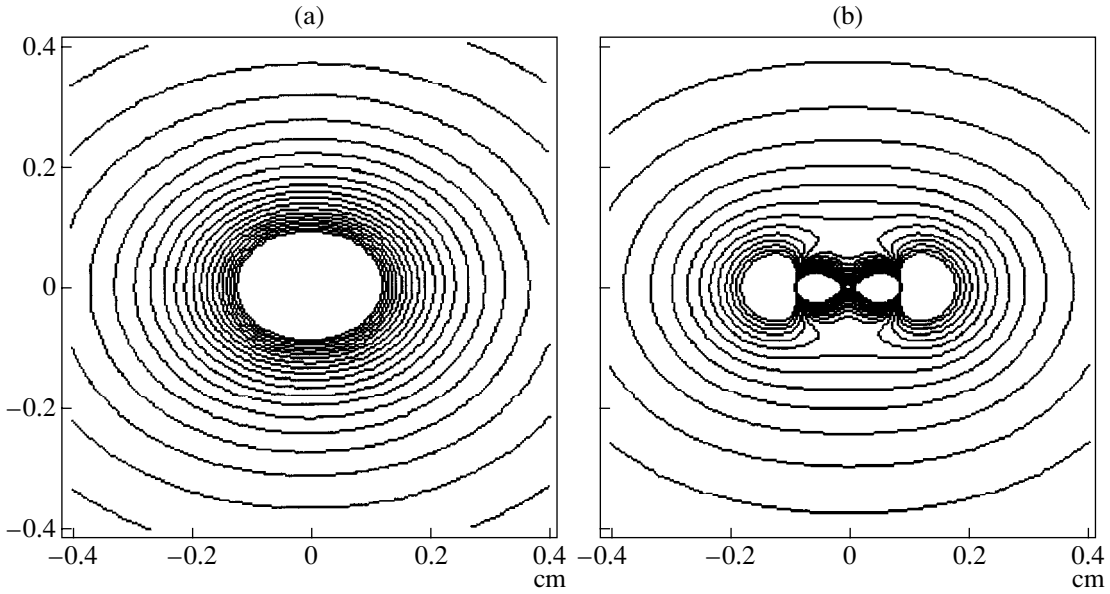

Fig. 5. Azimuthal magnetic field of a two-wire X-configuration (a) inside and (b) outside the intersection region.

has a much narrower front and at first seems to be less intense in a dense core medium. For a time of 5–10 ns, the core is heated by the ionizing wave of radiative heat conduction, which precedes the shock. Then, the accelerated and amplified shock wave reaches the core axis and reflects, which results in the strong heating of the core. This can be seen from a comparison of the temperature distributions corresponding to 23.2 and 29.5 ns. In addition, the distribution corresponding to 23.2 ns shows the presence of emission from the core surface when the shock formed by the corona compression wave decays. This emission, which manifests itself in the figure as a thin hot-plasma layer, lasts for $\simeq$10 ns (on the order of magnitude, this time is equal to the front width, $\simeq$70 μm, divided by the front velocity, $\simeq 5 \times 10^5$ cm/s).

After 30 ns, the temperature maximum is on the axis and a part of the current, which previously flowed through the corona, starts to flow through the core. The onset of the $m = 0$ mode of the MHD instability proceeds in a much more complicated fashion (see Fig. 4) than in models without a core. Finally, as in those models, alternating regions of a compressed and rarefied plasma are formed; however, in the constriction regions, $\simeq$100 μm in size, complex structures are pro-

duced in the form of several hot subpoints surrounded by a less dense substance of the heated core. Presumably, the nature of this phenomenon is the same as that of the phenomenon observed in experiment [7]. However, in our model, the situation is strongly simplified: actually, there is an approximately hundredfold drop at the corona–core interface, the core being a two-phase vapor–liquid medium [6]. The model also fails to describe the possible bursts of hydrodynamic turbulence [7]. This complicates the comparison between our model and the experiment.

It is also of interest to mention the results of calculations for a shorter size grid. In this case, we observed the onset of an instability with a smaller space and time scales. As a result, the maximum temperature and density in constrictions somewhat exceeded those obtained with a long-size grid. At the same time, the growth rates of numerical instabilities were also higher, so that we were forced to stop calculations in the earlier stage. We note that the plasma parameters calculated on the long-size grid are of the same order as for shorter size grids and the cell size affects the results only through the spatial resolution of the scheme. Regardless of the cell size, in all of the calculations, the values of Z were below 25, which was still far from the experimentally observed ion charge numbers.

4. SIMULATION OF THE X-PINCH

It is of interest to try to apply our model to the X-pinch occurring as a result of an explosion of two or four crossed wires in a diode. The three-dimensional geometry makes this problem very complicated to solve. As the first step, we can approximate the plasma configuration with the region between the surfaces of two coaxial cones. However, in this case, the magnetic field is completely absent in the inner vacuum region and cannot prevent the expansion of the heated plasma into the cone. To overcome this, we use the following qualitative method. We consider the plane of two initial crossed straight wires and assume that the actual plasma configuration can be replaced with the region between two cones touching the plasma columns on the inner and outer sides. As for the magnetic field, we take the exact expression for the azimuthal component B_θ of the field of the initial wires. This field can be easily found by solving the magnetostatic Ampere equation. Thus, for two straight current filaments crossed at an angle of 2α (the wire positions are described by the equation $r = |z|\tan\alpha$), we have the following expression for the components of the magnetic field:

$$B_r = Ic^{-1}\sin\alpha\{[\sin 2\alpha r(1+\cos 2\theta - \sin 2\theta)$$
$$\times(s_-^{-1}+s_+^{-1})/4 - z(\sin^2\alpha\cos\theta + \cos^2\alpha\sin\theta)]$$
$$\times(s_-^{-1}-s_+^{-1})\},$$

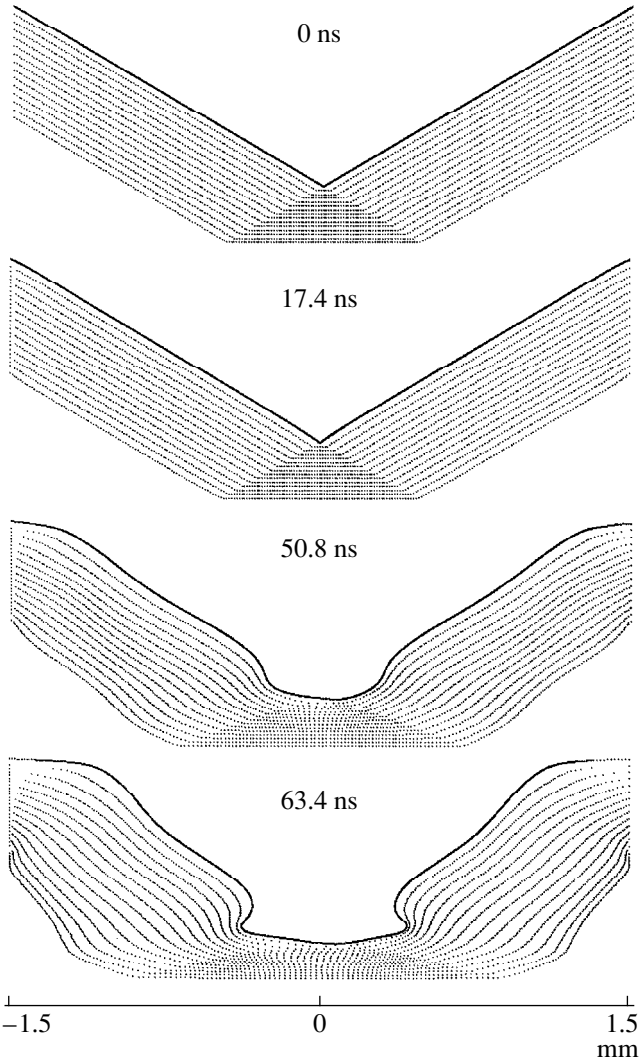

Fig. 6. The behavior of the shape of the X-pinch plasma and the distribution of the calculation points.

$$B_\theta = Ic^{-1}[(r\cos\alpha - z\sin\alpha\cos\theta)s_-^{-1}$$
$$+ (r\cos\alpha + z\sin\alpha\cos\theta)s_+^{-1}],$$
$$B_z = Ic^{-1}\sin\alpha r(s_-^{-1} - s_+^{-1})\cos\theta,$$

where

$$(s_\pm = z^2\sin^2\alpha + r^2(1-\sin^2\alpha\cos^2\theta)$$
$$\pm rz\sin 2\alpha\cos\theta).$$

This procedure can be extended to a more complex configuration in which the field of a similar pair of wires located in the perpendicular plane is added to the above field to produce the four-wire configuration and to any even number of the crossed current filaments. In the limit of large values of $|z|$, these solutions go over to the well-known formulas by Syrovatskiĭ [18] for the

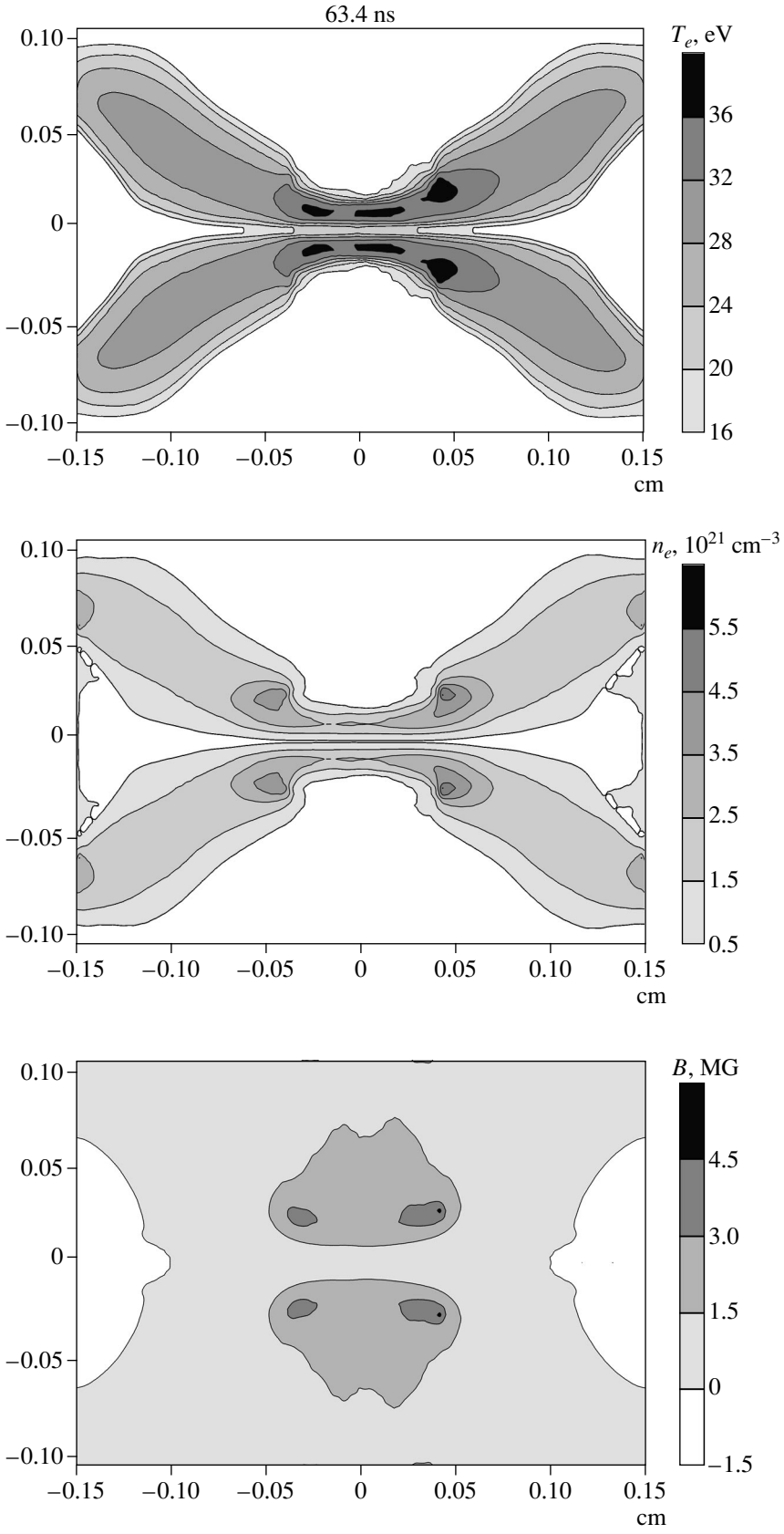

Fig. 7. Electron temperature, density, and magnetic field of the X-pinch.

magnetic field of an arbitrary number of parallel current filaments equidistantly located along the cylinder generatrix. In our case, only the azimuthal component of three magnetic field components was used and the boundary conditions $B = B_\theta$ on the inner and outer plasma–vacuum interfaces $r = a_{\text{ext, int}}(z, t)$ (in place of $B = 2I/ca$ with a one-wire load) were imposed. The rest was the same as in the problem based on equations (1)–(6).

Such an approach coarsens the model and restricts its applicability to the region near the wire intersection. Thus, if we expand the solution for the two-wire configuration with respect to azimuth, the $m = 0$ harmonic is dominant only in this region, whereas the amplitude of the $m = 2$ harmonic increases with distance from the intersection point (the $m = 1$ harmonic and other odd harmonics can be excluded if we assume the problem to be symmetric with respect to the plane perpendicular to the current filaments). The difference is clearly seen even in the behavior of the magnetic field component B_θ inside and outside the intersection region (Fig. 5), where the $m = 2$ mode is present even at the point of filament intersection, $z = 0$. As a first step, we will restrict ourselves to the simplified model and will describe only the most important intersection region. In order to avoid extra difficulties in solving the problem, which is rather complicated in itself, we do not include the core in our consideration. For the same purpose, we also do not include the complete set of the magnetic field components in the model. It is hard to estimate the inaccuracy of our approach in advance; however, the results presented below can serve to obtain such an estimate.

The initial configuration of the calculation points is shown in Fig. 6. Calculations carried out on both the rough (15×251) and finer (21×500) grids show the fundamental difference in the dynamics of a two-wire X-pinch and a single-wire system. First, the geometry of the intersection region turns out to be unfavorable for the formation of an MHD shock. In contrast to the similar problem for the Z-pinch, the shock wave is not only late to originate, but its intensity is very weak. The perturbations penetrate into the plasma not with a defocusing shock wave but with a heat-conduction wave; this is seen even in the calculation-point distribution in Fig. 6. The low intensity of the shock wave leads to its deceleration and a slowing-down of the compression process as a whole. The final instant (63 ns after the current passes its maximum) corresponds to a slightly more than twofold compression of the constriction. Note that, in this case, the constriction extends in the z-direction and the azimuthally asymmetric modes become important. The regions most remote from the point of intersection are where the highest plasma parameters are attained (Fig. 7). However, the values of these parameters are modest compared to those obtained for a single-wire configuration.

It is of interest to compare the results with previous attempts to calculate the X-pinch [19]. The model proposed in [19] surpasses our model in the accuracy of the description of radiation transport and atomic processes; however, both models are comparable in the description of the pinch dynamics. Note that the geometrical configuration of the plasma in [19] represented the region between the surfaces of two coaxial cones and the magnetic field in the inner vacuum region was completely absent. The main factor contributing to the inaccuracy of the model in [19] in the late stage of compression near the pinch cross is the plasma expansion into the inner vacuum region. In contrast to this, the more adequate description of the magnetic field in our model allows us to approach the situation in which the 3D effects manifest themselves in the X-pinch dynamics more clearly.

5. CONCLUSION

The main advantage of the three-temperature model developed in this paper is the possibility of taking into account small-scale nonequilibrium processes in the electron–radiation system. In order to study these processes, the time step must be substantially reduced. This leads to an increase in the spatial resolution of the scheme and, consequently, to a more detailed description of the distribution of the plasma parameters and the shape of the free plasma boundary. This is manifested most clearly in calculations of the corona–core system. The shape of the corona–core was still too blurred and did not allow us to adequately describe the fine processes of the onset of the surface hydrodynamic instabilities that were observed in [7]. Presumably, we revealed a tendency toward the formation of a fine structure of hot points. By partially taking into account the 3D structure of the magnetic field, we obtained a much stronger compression than in the previous X-pinch model [19]. Nevertheless, in our model, the amplitude of the shock wave is low, which may be due to an incomplete and insufficiently accurate consideration of 3D effects. On the whole, the three-temperature model can be considered appropriate for solving the problem of pinch dynamics, but the formulation of the problem should be more adequate for actual experiments.

REFERENCES

1. G. V. Ivanenkov and V. Stepniewski, Fiz. Plazmy **22**, 528 (1996) [Plasma Phys. Rep. **22**, 459 (1996)].
2. V. F. D'yachenko and V. S. Imshennik, in *Reviews of Plasma Physics*, Ed. by M. A. Leontovich (Atomizdat, Moscow, 1974; Consultants Bureau, New York, 1980), Vol. 8.
3. K. Jach and E. Wlodarczyk, J. Tech. Phys. (Warsaw) **27**, 85 (1986).
4. G. V. Ivanenkov, A. R. Mingaleev, S. A. Pikuz, *et al.*, in *Proceedings of 4th International Conference on Dense Z-Pinches, Vancouver, Canada, 1997*, p. 253.
5. G. V. Ivanenkov, A. R. Mingaleev, S. A. Pikuz, *et al.*, Zh. Éksp. Teor. Fiz. **114**, 1216 (1998) [JETP **87**, 663 (1998)].

6. S. A. Pikuz, G. V. Ivanenkov, T. A. Shelkovenko, and D. Hammer, Pis'ma Zh. Éksp. Teor. Fiz. **69**, 349 (1999) [JETP Lett. **69**, 377 (1999)].
7. S. Yu. Gus'kov, G. V. Ivanenkov, A. R. Mingaleev, *et al.*, Pis'ma Zh. Éksp. Teor. Fiz. **67**, 531 (1998) [JETP Lett. **67**, 559 (1998)].
8. Yu. V. Afanas'ev, E. G. Gamaliĭ, and V. B. Rozanov, Tr. FIAN **134**, 5 (1982).
9. S. I. Braginskii, in *Reviews of Plasma Physics*, Ed. by M. A. Leontovich (Atomizdat, Moscow, 1963; Consultants Bureau, New York, 1980).
10. V. M. Zhdanov, *Transport Phenomena in Multicomponent Plasmas* (Energoatomizdat, Moscow, 1982).
11. I. M. Bespalov and A. Ya. Polishchuk, Pis'ma Zh. Tekh. Fiz. **15** (2), 4 (1989) [Sov. Tech. Phys. Lett. **15**, 39 (1989)].
12. M. M. Basko, Teplofiz. Vys. Temp. **23**, 483 (1985).
13. G. D. Tsakiris and K. Eidman, J. Quant. Spectrosc. Radiat. Transfer **38**, 353 (1987).
14. I. G. Beĭgman, L. A. Vaĭnshteĭn, and A. V. Vinogradov, Astron. Zh. **46**, 985 (1969) [Sov. Phys. Astron. **13**, 775 (1969)].
15. V. S. Volokitin, I. O. Golosnoĭ, and N. N. Kalitkin, Izv. Vyssh. Uchebn. Zaved., Fiz., No. 4, 11 (1995).
16. G. V. Ivanenkov, A. R. Mingaleev, T. A. Novikova, *et al.*, Zh. Tekh. Fiz. **65** (4), 40 (1995).
17. Ya. B. Zel'dovich and Yu. P. Raizer, *Physics of Shock Waves and High-Temperature Hydrodynamic Phenomena* (Nauka, Moscow, 1966; Academic, New York, 1966, 1967), Vols. 1 and 2.
18. S. I. Syrovatskiĭ, Zh. Éksp. Teor. Fiz. **50**, 1133 (1966) [Sov. Phys. JETP **23**, 754 (1966)].
19. E. L. Cochran and J. Davis, Phys. Fluids B **2**, 1238 (1990).

Translated by A. D. Smirnova

Plasma Physics Reports, Vol. 26, No. 1, 2000, pp. 33–40. Translated from Fizika Plazmy, Vol. 26, No. 1, 2000, pp. 36–43.

PLASMA OSCILLATIONS AND WAVES

Effect of the Helical Nonuniformity of the Confining Magnetic Field on the MHD Eigenmodes in Straight Stellarators

I. A. Girka and P. K. Kovtun

Kharkov State University, pl. Svobody 4, Kharkov, 310077 Ukraine

Received August 26, 1998

Abstract—Perturbation theory is applied to derive the dispersion relation describing the propagation of magnetohydrodynamic waves in a plasma in the helical magnetic field of a stellarator. The correction to the eigenfrequency, $\delta\omega$, introduced by a small deviation of the magnetic surfaces from being cylindrical is found. *© 2000 MAIK "Nauka/Interperiodica".*

1. INTRODUCTION

The Alfvén and magnetosonic branches of magnetohydrodynamic (MHD) waves are of interest mainly because they are used for RF heating of plasmas in fusion devices (see, e.g., [1–3]). MHD oscillations of the plasma column in an axisymmetric magnetic field have been studied quite thoroughly (see, e.g., [4–7] and the literature cited therein).

Here, we study analytically the problem of MHD eigenmodes of the plasma column in a stellarator with allowance for the deviation of the magnetic surfaces from being cylindrical. We consider electromagnetic waves with a frequency on the order of the ion cyclotron frequency in a plasma whose pressure is low in comparison with that of the external magnetic field, in which case the electron inertia can be neglected in studying MHD oscillations. We assume that the plasma is fully ionized. Under these assumptions, we can apply perturbation theory to derive the dispersion relation for MHD waves and to determine the correction to the frequency of eigenmodes that results from the deviation of the stellarator magnetic surfaces from being cylindrical. We show that this correction is a second-order quantity in the small parameter characterizing the magnetic field nonuniformity.

2. FORMULATION OF THE PROBLEM

We consider the propagation of MHD waves with a frequency $\omega \ll |\omega_{ce}|, \omega_{pe}$ (where $\omega_{c\alpha}$ and $\omega_{p\alpha}$ are the cyclotron and Langmuir frequencies of the particles of species α with $\alpha = e$ for electrons and $\alpha = i$ for ions) in a plasma column in a coaxial ideally conducting metal chamber. The entire system is in a constant magnetic field $\mathbf{B}_0 = \mathbf{e}_r B_{0r} + \mathbf{e}_\varphi B_{0\varphi} + \mathbf{e}_z B_{0z}$ written in cylindrical coordinates (r, φ, z). In the paraxial approximation, the magnetic field of an $l \geq 2$ stellarator can be simplified to [8]

$$B_{0r} = \bar{\epsilon} B_{00} \sin(l\theta), \quad B_{0\varphi} = \epsilon l (k_s r)^{-1} B_{00} \cos(l\theta), \quad B_{0z} = B_{00} - \epsilon B_{00} \cos(l\theta), \tag{1}$$

where $\epsilon(r) \equiv l b_l I_l(k_s r)/B_{00}$, $\bar{\epsilon}(r) \equiv l b_l I_l'(k_s r)/B_{00}$, $b_l = 8Jbk_s^2 K_l'(k_s b)(lc)^{-1}$, B_{00} is a uniform magnetic field produced by the toroidal coils, $\theta = \varphi - \alpha z$, $\alpha = 2\pi/L$, $k_s = \alpha l$, L is the pitch of the helical winding, b is the radius of a thin helical coil with the current J (in our problem, b is assumed to be equal to the radius of the metal chamber), $K_l(\xi)$ and $I_l(\xi)$ are modified Bessel functions, and the prime denotes the derivative with respect to the argument. Under the assumption that the helical-coil currents are lower than the toroidal-coil currents, the quantities ϵ and $\bar{\epsilon}$ can be regarded as small parameters of the problem, $\epsilon \ll 1$ and $\bar{\epsilon} \ll 1$, which allows us to apply perturbation theory. The magnetic surfaces of the magnetic field (1) are described by the equation

$$r_0 = r - \bar{\epsilon}(l\alpha)^{-1} \cos(l\theta) - \bar{\epsilon}^2/(2l^2\alpha^2 r)\cos^2(l\theta) + O(\bar{\epsilon}^3), \tag{2}$$

where r_0 should be treated as the "number" of the magnetic surface. We assume that the equilibrium plasma density $n(r, \varphi, z)$ is a function of the magnetic surface, $n(r, \varphi, z) = n(r_0)$. For $r_0 = b$, equation (2) describes the outermost magnetic surface, which is assumed to coincide with the inner surface of the metal chamber. The density profile is assumed to be such that the fundamental Alfvén resonance (AR), at which $\varepsilon_1^{(0)}(r) = N_z^2$, and the satellite AR [9], at which $\varepsilon_1^{(0)}(r) = (N_z \pm N_s)^2$, are both absent. Girka and Stepanov [10] solved a similar problem—the propagation of MHD waves in a plasma column in a rippled magnetic field.

For the confining magnetic field (1) written in cylindrical coordinates, all nine elements of the plasma

1063-780X/00/2601-0033$20.00

dielectric tensor are nonzero. However, we can introduce a local coordinate system that is associated with the lines of the external field (1) and in which the dielectric tensor can be simplified to

$$\varepsilon_{11}^{\mathrm{loc}} = \varepsilon_{22}^{\mathrm{loc}} = \varepsilon_1, \quad \varepsilon_{12}^{\mathrm{loc}} = -\varepsilon_{21}^{\mathrm{loc}} = i\varepsilon_2,$$
$$\varepsilon_{33}^{\mathrm{loc}} = \varepsilon_3,$$

the remaining components being equal to zero, $\varepsilon_{ik}^{\mathrm{loc}} = 0$.

For a cold plasma in which collisions are neglected, the elements of the dielectric tensor are

$$\varepsilon_1 = 1 + \sum_i \frac{\omega_{pi}^2(r_0)}{\omega_{ci}^2 - \omega^2}, \quad \varepsilon_2 = \sum_i \frac{\omega\omega_{pi}^2(r_0)}{(\omega_{ci}^2 - \omega^2)\omega_{ci}}, \quad (3)$$
$$\varepsilon_3 = -\omega_{pe}^2/\omega^2.$$

Here, the cyclotron frequency $\omega_{c\alpha}$ is defined in terms of the total magnetic field $B_0(r, \varphi, z)$ from (1): $\omega_{c\alpha} = eB_0/(m_\alpha c)$, where $B_0 = \{B_{0r}^2 + B_{0\varphi}^2 + B_{0z}^2\}^{1/2}$. The basic vectors of the local coordinate system are chosen as follows: the vector $\mathbf{e}_3 = \mathbf{B}_0/B_0$ is directed along a magnetic field line, the vector $\mathbf{e}_1 = \nabla r_0/|\nabla r_0|$ is perpendicular to the magnetic surface formed by this line, and the vector $\mathbf{e}_2 = \mathbf{e}_3 \times \mathbf{e}_1$ is such that the basic vectors form a right-hand triple.

We expand the elements of the plasma dielectric tensor in powers of the small parameters ϵ and $\bar{\epsilon}$:

$$\varepsilon_{1,2} = \varepsilon_{1,2}^{(0)}(r) + \varepsilon_{1,2}^{(1)}(r)\cos(l\theta) + \varepsilon_{1,2}^{(2)}(r) + O(\bar{\epsilon}^3), \quad (4)$$

$$\varepsilon_1^{(0)}(r) = 1 + \frac{\omega_{pi}^2(r)}{\omega_{ci}^{(0)2} - \omega^2}, \quad (5)$$

$$\varepsilon_1^{(1)}(r) = -\frac{1}{k_s}\frac{\partial \ln(\omega_{pi}^2)}{\partial r_0}\bar{\epsilon}(r)[\varepsilon_1^{(0)}(r) - 1] + \epsilon(r)\frac{2(\varepsilon_1^{(0)}(r) - 1)^2}{N_A^2(r)}, \quad (6)$$

$$\varepsilon_1^{(2)}(r) = -\frac{(\varepsilon_1^{(0)} - 1)}{k_s}\frac{\partial \ln(\omega_{pi}^2)}{\partial r_0}\left(\frac{\bar{\epsilon}^2}{4k_s r} + \frac{\epsilon\bar{\epsilon}(\varepsilon_1^{(0)} - 1)}{N_A^2}\right)$$
$$-\frac{(\varepsilon_1^{(0)} - 1)^2}{2N_A^2}\left(\bar{\epsilon}^2 + \frac{l^2\epsilon^2}{k_s^2 r^2} - \epsilon^2(\varepsilon_1^{(0)} - 1)\frac{\omega^2 + 3\omega_{ci}^{(0)2}}{\omega_{pi}^2}\right) \quad (7)$$
$$+\frac{\bar{\epsilon}^2}{4k_s^2}\frac{\partial^2\omega_{pi}^2}{\partial r_0^2}\frac{1}{\omega_{ci}^{(0)2} - \omega^2},$$

$$\varepsilon_2^{(0)}(r) = \frac{\omega_{pi}^2(r)\omega}{\omega_{ci}^{(0)}(\omega_{ci}^{(0)2} - \omega^2)}, \quad (8)$$

$$\varepsilon_2^{(1)}(r) = -\frac{\bar{\epsilon}}{k_s}\frac{\partial \ln\omega_{pi}^2}{\partial r_0}\varepsilon_2^{(0)} + \epsilon\varepsilon_2^{(0)}\left(1 + \frac{2\omega_{ci}^{(0)}\varepsilon_2^{(0)}}{\omega N_A^2}\right), \quad (9)$$

$$\varepsilon_2^{(2)}(r) = -\frac{\varepsilon_2^{(0)}}{k_s}\frac{\partial \ln(\omega_{pi}^2)}{\partial r}\left(\frac{\bar{\epsilon}^2}{4k_s r} + \frac{\epsilon\bar{\epsilon}}{2} + \epsilon\bar{\epsilon}\frac{\omega_{ci}^{(0)}\varepsilon_2^{(0)2}}{\omega N_A^2}\right)$$
$$+\frac{\bar{\epsilon}^2}{4k_s^2}\frac{\partial^2\omega_{pi}^2}{\partial r_0^2}\frac{\omega/\omega_{ci}^{(0)}}{\omega_{ci}^{(0)2} - \omega^2} + \frac{\varepsilon_2^{(0)}}{4}\left(1 + \frac{2\omega_{ci}^{(0)}\varepsilon_2^{(0)}}{\omega N_A^2}\right) \quad (10)$$
$$\times\left(2\epsilon^2 - \bar{\epsilon}^2 - \frac{l^2\epsilon^2}{k_s^2 r^2}\right) + \frac{\epsilon^2}{2}\frac{\varepsilon_2^{(0)3}(\omega^2 + 3\omega_{ci}^2)}{\omega^2 N_A^4},$$

where $\omega_{ci}^{(0)} = \omega_{ci}(B_{00})$ and $N_A(r) = \omega_{pi}(r)/\omega_{ci}^{(0)}$ is the Alfvén refractive index.

The angular dependence in expansion (4) is governed by the symmetry of the confining magnetic field (1). This symmetry enables us to seek a solution to the Maxwell equations for the axial component of the magnetic field of an MHD wave in the form

$$B_z = \exp\{i(k_z z + m\varphi - \omega t)\} \times [B^{\sim}(r) + B^{(+)}(r)\exp(il\theta) + B^{(-)}(r)\exp(-il\theta)], \quad (11)$$

where $B^{\sim}(r) = B^{(0)}(r) + B^{(2)}(r)$; $B^{(2)} \sim \epsilon^2 B^{(0)}$; $B^{(\pm)} \sim \epsilon B^{(0)}$; m is the azimuthal wavenumber; k_z is the axial wavenumber of the fundamental mode of an MHD wave; and $B^{(0)}(r)$ is the fundamental mode amplitude, which is assumed to be known from the solution to the problem of the propagation of an MHD wave in a straight magnetic field (in the zeroth approximation). The amplitudes $B^{(\pm)}(r)$ of the satellite modes and the small second-order correction $B^{(2)}$ to the amplitude of the fundamental mode can be evaluated from perturbation theory. Such an approach to solving the Maxwell equations is usually referred to as the Floquet–Bloch method (see, e.g., [11]). Here and below, we neglect small second-order terms proportional to $\exp[\pm 2il\theta]$, which make a small contribution (whose order is higher than ϵ^2) to the final expression for the eigenfrequency.

To simplify the set of Maxwell equations, note that, in studying fast magnetosonic (FMS) and Alfvén branches of MHD waves, the electron inertia can be neglected. For MHD waves in the frequency range under consideration, we have $\varepsilon_3 \longrightarrow \infty$; i.e., we can approximately set $E_3 = 0$, which allows us to express E_z in terms of E_r and E_φ:

$$E_z = -\bar{\epsilon}(r)E_r\sin(l\theta) - E_\varphi l\epsilon(r)/(k_s r)[\cos(l\theta) + \epsilon(r)/2]. \quad (12)$$

Then, we can reduce the Maxwell equations in a plasma to the following three equations for the components B_z,

E_r, and E_φ in cylindrical coordinates:

$$\frac{1}{r}\frac{\partial}{\partial r}(rE_\varphi) - \frac{1}{r}\frac{\partial E_r}{\partial \varphi} = i\frac{\omega}{c}B_z,$$

$$\frac{c}{\omega r}\frac{\partial^2}{\partial z \partial \varphi}(a_{13}E_r + a_{23}E_\varphi) + \frac{c}{\omega}\frac{\partial^2 E_\varphi}{\partial z^2} + i\frac{\partial B_z}{\partial r}$$

$$= -\frac{\omega}{c}\{\varepsilon_{21}E_r + \varepsilon_{22}E_\varphi - \varepsilon_{23}(a_{13}E_r + a_{23}E_\varphi)\}, \quad (13)$$

$$\frac{1}{r}\frac{\partial B_z}{\partial \varphi} + i\frac{c}{\varphi}\frac{\partial^2 E_r}{\partial z^2} + i\frac{c}{\omega}\frac{\partial^2}{\partial z \partial r}(a_{13}E_r + a_{23}E_\varphi)$$

$$= -i\frac{\omega}{c}\{\varepsilon_{11}E_r + \varepsilon_{12}E_\varphi - \varepsilon_{13}(a_{13}E_r + a_{23}E_\varphi)\}.$$

Here, the elements $a_{13} = B_{0r}/B_{00}$ and $a_{23} = B_{0\varphi}/B_{00}$ of the matrix for transforming from a local to a cylindrical coordinate system can be calculated from the formula $a_{ki} = (\mathbf{e}_k^{\text{cyl}}, \mathbf{e}_i)$, where $\mathbf{e}_k^{\text{cyl}}$ $(k = r, \varphi, z)$ are the unit vectors of the cylindrical coordinate system and $\varepsilon_{kl} = a_{ki}\varepsilon_{ij}^{\text{loc}}a_{lj}$ are the elements of the plasma dielectric tensor in cylindrical coordinates.

To solve the problem, we substitute expansions (11) for the fields of an MHD wave into equations (13) and impose the following boundary conditions:

(i) The wave fields should be finite over the entire volume inside the chamber.

(ii) The tangential component of the electric field should vanish at the inner surface of the metal chamber.

(iii) If there is a vacuum gap between the plasma column and the chamber, then the tangential components of the electric and magnetic fields of an MHD wave should be continuous at the plasma–vacuum boundary; specifically, in local coordinates, the continuous components are E_2 and B_3.

3. ZEROTH APPROXIMATION

In the zeroth approximation, the amplitude of the fundamental harmonic of the electric field of an MHD wave can be expressed in terms of $B^{(0)}$ from the solution to equations (13):

$$E_\varphi^{(0)} = -i\frac{\omega}{ck_\perp^2}\left(\frac{m}{r}\mu B^{(0)} + \frac{dB^{(0)}}{dr}\right),$$
$$E_r^{(0)} = -\frac{\omega}{ck_\perp^2}\left(\frac{m}{r}B^{(0)} + \mu\frac{dB^{(0)}}{dr}\right), \quad (14)$$

where

$$k_\perp^2(k_z, r) = \frac{\omega^2}{c^2}\frac{(\varepsilon_1^{(0)} - N_Z^2)^2 - \varepsilon_2^{(0)2}}{\varepsilon_1^{(0)} - N_Z^2},$$

$$\mu(k_z, r) = \frac{\varepsilon_2^{(0)}}{\varepsilon_1^{(0)} - N_Z^2},$$

and $N_Z = k_z c/\omega$ is the axial refractive index for the wave. The axial component $B^{(0)}$ of the magnetic field of the wave satisfies the equation

$$\frac{1}{r}\frac{d}{dr}\left(\frac{r}{k_\perp^2}\frac{dB^{(0)}}{dr}\right) + \left(1 - \frac{m^2}{k_\perp^2 r^2} + \frac{m}{r}\frac{d}{dr}\left(\frac{\mu}{k_\perp^2}\right)\right)B^{(0)} = 0, \quad (15)$$

which has the following solution that is finite at the cylinder axis: $B^{(0)} = A_0 f_0(r)$, where A_0 is an integration constant. For an arbitrary density profile, equation (15) can be solved numerically (see, e.g., [7] and subsequent papers), so that $f_0(r)$ can be assumed to be a known function.

In the zeroth approximation, the problem is treated in cylindrical geometry and the boundary conditions yield the following dispersion relation for an MHD wave in a uniform magnetic field:

$$D^{(0)}(\omega, k_z, m) = 0, \quad (16)$$

where

$$D^{(0)} = \left(\frac{m\mu}{k_\perp r}f_0(r) + \frac{1}{k_\perp}\frac{df_0(r)}{dr}\right)_{r=b}. \quad (17)$$

The solution $\omega = \omega_0$ to (16) is assumed to be known. Note that, for a circular cylinder, we have $E_z = 0$ not only in the plasma but also in the vacuum gap, in which case the dispersion relation can be derived with no regard for the condition that E_z and B_φ are continuous at the circular cylindrical plasma–vacuum boundary.

4. FIRST APPROXIMATION

Now, we solve the Maxwell equations in the first approximation. The amplitudes of the first satellite harmonics of the wave electric field are expressed in terms of the magnetic field as

$$E_r^{(\pm)} = -\frac{\omega}{ck_\pm^2}\left(\frac{m \pm l}{r}B^{(\pm)} + G_\pm(r) + \mu^\pm\left[\frac{dB^\pm}{dr} + F_\pm(r)\right]\right), \quad (18)$$

$$E_\varphi^{(\pm)} = -\frac{i\omega}{ck_\pm^2}\left(\mu^{(\pm)}\left[\frac{m \pm l}{r}B^{(\pm)} + G_\pm(r)\right] + \frac{dB^\pm}{dr} + F_\pm(r)\right), \quad (19)$$

where $k_\pm = k_\perp(k_z \mp k_s)$ and $\mu^{(\pm)} = \mu(k_z \mp k_s)$.

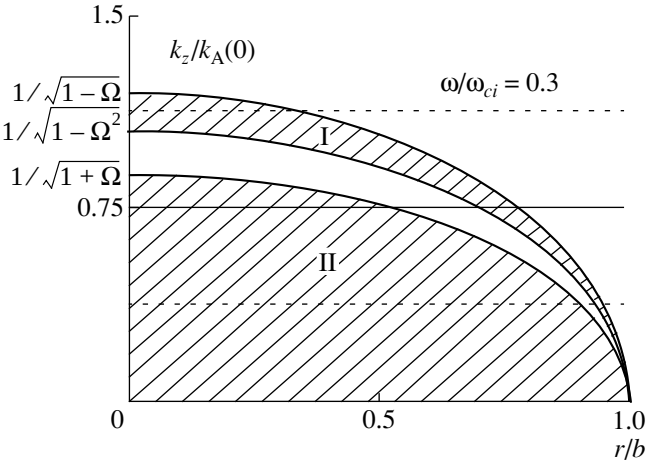

Diagram of sign($k_\perp^2$) in a plane in which the radius normalized to the radius of the metal chamber and the axial wavenumber normalized to the Alfvén wavenumber serve as coordinates. The regions in which $k_\perp^2 > 0$ are hatched.

The first-order functions $G_\pm(r)$ and $F_\pm(r)$ are related to the wave electric field components, which were found in the zeroth approximation, by

$$F_\pm(r) = \frac{1}{2}E_r^{(0)}\left(\pm\frac{\bar\epsilon(m\pm l)N_Z^{(\pm)}}{r} - \frac{\omega}{c}\varepsilon_2^{(1)}\right) + \frac{i}{2}E_\varphi^{(0)}\left(\frac{l\epsilon(m\pm l)N_Z^{(\pm)}}{k_s r^2} - \frac{\omega}{c}\varepsilon_1^{(1)}\right), \quad (20)$$

$$G_\pm(r) = \pm\frac{\bar\epsilon N_Z^{(\pm)}}{2}\frac{dE_r^{(0)}}{dr} + \frac{i\epsilon l N_Z^{(\pm)}}{2k_s r}\frac{dE_\varphi^{(0)}}{dr} + \frac{1}{2}E_r^{(0)}\left(\pm\frac{d\bar\epsilon}{dr}N_Z^{(\pm)} + \frac{\omega}{c}\varepsilon_1^{(1)}\right) + \frac{i}{2}E_\varphi^{(0)}\left(\frac{d}{dr}\left(\frac{l\epsilon}{k_s r}\right)N_Z^{(\pm)} + \frac{\omega}{c}\varepsilon_2^{(1)}\right), \quad (21)$$

where $N_Z^{(\pm)} = (k_z \mp k_s)c/\omega$.

The amplitudes of the satellite harmonics of the axial component of the wave magnetic field satisfy the equation

$$\frac{1}{r}\frac{d}{dr}\left(\frac{r}{k_\pm^2}\frac{dB^{(\pm)}}{dr}\right) + \left(1 - \frac{(m\pm l)^2}{k_\pm^2 r^2} + \frac{m\pm l}{r}\frac{d}{dr}\left(\frac{\mu^{(\pm)}}{k_\pm^2}\right)\right)B^{(\pm)} = \mathcal{L}_\pm(r), \quad (22)$$

where

$$\mathcal{L}_\pm(r) = -\frac{1}{r}\frac{d}{dr}\left[\frac{r}{k_\pm^2}(\mu^{(\pm)}G_{(\pm)} + F_\pm)\right] + \frac{m\pm l}{k_\pm^2 r}(G_{(\pm)} + \mu^{(\pm)}F_\pm). \quad (23)$$

This equation can be solved by the method of varying a constant:

$$B^{(\pm)}(r) = A^{(\pm)}f_1^{(\pm)}(r) + g_\pm(r). \quad (24)$$

Here, $A^{(\pm)}$ is an integration constant; $f_1^{(\pm)}(r)$ is the general solution to equation (22) with a zero right-hand side (this solution is finite at $r = 0$, whereas the second solution $f_2^{(\pm)}(r)$ diverges toward the plasma axis); and $g_\pm(r)$ is a particular solution to the inhomogeneous equation (22):

$$g_\pm(r) = C_1(r)f_1^{(\pm)}(r) + C_2(r)f_2^{(\pm)}(r), \quad (25)$$

where

$$C_1(r) = -\int_b^r \mathcal{L}_\pm(r)f_2^{(\pm)}(r)W^{-1}(f_1^{(\pm)}, f_2^{(\pm)})dr, \quad (26)$$

$$C_2(r) = \int_0^r \mathcal{L}_\pm(r)f_1^{(\pm)}(r)W^{-1}(f_1^{(\pm)}, f_2^{(\pm)})dr, \quad (27)$$

and $W(f_1^{(\pm)}, f_2^{(\pm)}) = f_1^{(\pm)}(r)\,df_2^{(\pm)}(r)/dr - f_2^{(\pm)}(r)\,df_1^{(\pm)}(r)/dr$ is the Wronskian of the functions $f_1^{(\pm)}$ and $f_2^{(\pm)}$.

With the boundary conditions imposed, allowing for small first-order terms does not change the dispersion relation but makes it possible to find the amplitudes $A^{(\pm)}$ of the first satellite harmonics. In the boundary conditions, we single out the terms proportional to $\exp[i(k_z \mp k_s)z + i(m \pm l)\varphi]$ to obtain

$$A^{(\pm)} = D_\pm^{-1}\left\{\pm\frac{l\bar\epsilon k_\pm c}{2k_s r\omega}E_r^{(0)} - i\frac{\bar\epsilon k_\pm c}{2k_s\omega}\frac{dE_\varphi^{(0)}}{dr} - \frac{(m\pm l)\mu^{(\pm)}}{k_\pm r}g_\pm - \frac{1}{k_\pm}\frac{dg_\pm}{dr} - \frac{\mu G_\pm + F_\pm}{k_\pm}\right\}_{r=b}, \quad (28)$$

where $D_\pm = D^{(0)}(\omega_0, k_z \mp k_s, m \pm l)$.

We will say a few words about the polarization of the satellite harmonics. The analysis of this question in the zeroth approximation shows that the harmonic polarization can be described merely by examining the behavior of the first term on the right-hand side of (24). Equation (15) implies that the plasma region transparent to the given wave is determined by the condition $k_\perp^2 > 0$. In the diagram shown in the figure, the regions

in which $k_\perp^2 > 0$ are hatched. The current radius normalized to the radius b of the metal chamber is plotted on the abscissa, and the ordinate is the axial wavenumber k_z normalized to the Alfvén wavenumber $k_A(0) = \omega\omega_{pi}(r = 0)/(c\omega_{ci})$ taken at the plasma axis. The radial density profile is assumed to be parabolic, $n(r) = n_0(1 - r^2/b^2)$, and the wave frequency is chosen to be $\omega = 0.3\omega_{ci}$. In region I, the wave polarization corresponds to the Alfvén wave (AW), and in region II, it corresponds to the FMS wave.

As an example, we consider a wave with a sufficiently small axial wavenumber k_z of the fundamental mode (see the horizontal solid line in the diagram). Near the plasma axis, the polarization of the fundamental mode coincides with that of the FMS wave. The opaque region for the fundamental mode lies farther away from the axis. In region I, the polarization of the fundamental mode coincides with that of the AW. Finally, there is another opaque region near the metal chamber. The polarization of one of the satellite modes with the axial wavenumber $k_z - k_s$ (the lower horizontal dashed line) coincides qualitatively with that of the fundamental mode. Near the axis, the second satellite mode with the axial wavenumber $k_z + k_s$ (the upper horizontal dashed line) is polarized in the same manner as the AW, whereas the plasma region near the chamber wall is opaque to this mode.

We can see that the polarization of the satellite modes can differ from that of the fundamental mode. Depending on the relation between k_z, k_s, and $k_A(0)$, the mutual polarization of the fundamental and satellite modes may differ from what we have just analyzed. Note, in particular, that, if a dashed line does not cross the hatched region, then the corresponding satellite mode propagates as a surface wave.

5. SECOND-ORDER APPROXIMATION

Now, we solve the Maxwell equations in the second-order approximation in the small parameters ε and $\bar{\varepsilon}$. Second-order corrections to the amplitude of the fundamental harmonic of the wave electric field can be expressed in terms of the magnetic field in the same manner as those in the first-order approximation [see (18) and (19)]:

$$E_r^{(2)} = -\frac{\omega}{ck_\perp^2}\left(\frac{m}{r}B^{(2)} + G^{(2)}(r) + \mu\left[\frac{dB^{(2)}}{dr} + F^{(2)}(r)\right]\right), \quad (29)$$

$$E_\varphi^{(2)} = -\frac{i\omega}{ck_\perp^2}\left(\mu\left[\frac{m}{r}B^{(2)} + G^{(2)}(r)\right] + \frac{dB^{(2)}}{dr} + F^{(2)}(r)\right), \quad (30)$$

where the second-order functions $G^{(2)}(r)$ and $F^{(2)}(r)$ are

$$\begin{aligned} F^{(2)}(r) &= -\frac{\omega}{c}\frac{\varepsilon_2^{(1)}}{2}(E_r^{(+)} + E_r^{(-)}) - \frac{\bar{\epsilon}N_Z m}{2r}(E_r^{(+)} - E_r^{(-)}) \\ &\quad - i\left[\frac{\omega}{c}\frac{\varepsilon_1^{(1)}}{2} - \frac{\epsilon N_Z m l}{2k_s r^2}\right](E_\varphi^{(+)} + E_\varphi^{(-)}) \\ &\quad - \frac{\omega}{c}\left(\varepsilon_2^{(2)} + \frac{\varepsilon_2^{(0)}}{4}\left(\bar{\epsilon}^2 - \frac{\epsilon^2 l^2}{k_s^2 r^2}\right)\right)E_r^{(0)} \\ &\quad - i\left[\frac{\omega}{c}\varepsilon_1^{(2)} - \frac{\epsilon^2 N_Z m l}{2k_s r^2}\right]E_\varphi^{(0)}, \end{aligned} \quad (31)$$

$$\begin{aligned} G^{(2)}(r) &= \frac{\omega}{c}\frac{\varepsilon_1^{(1)}}{2}(E_r^{(+)} + E_r^{(-)}) - \frac{N_Z}{2}\frac{d\bar{\epsilon}}{dr}(E_r^{(+)} - E_r^{(-)}) \\ &\quad - \frac{\bar{\epsilon}N_Z}{2}\left(\frac{dE_r^{(+)}}{dr} - \frac{dE_r^{(-)}}{dr}\right) + i\left[\frac{\omega}{c}\frac{\varepsilon_2^{(1)}}{2} + \frac{N_Z}{2}\frac{d}{dr}\left(\frac{\epsilon l}{k_s r}\right)\right] \\ &\quad \times (E_\varphi^{(+)} + E_\varphi^{(-)}) + \frac{i\epsilon N_Z l}{2k_s r}\left(\frac{dE_\varphi^{(+)}}{dr} + \frac{dE_\varphi^{(-)}}{dr} + \epsilon\frac{dE_\varphi^{(0)}}{dr}\right) \\ &\quad + \frac{\omega}{c}\varepsilon_1^{(2)}E_r^{(0)} + iN_Z\frac{d}{dr}\left(\frac{\epsilon^2 l}{2k_s r}\right)E_\varphi^{(0)} \\ &\quad + i\frac{\omega}{c}\left[\varepsilon_2^{(2)} - \frac{\varepsilon_2^{(0)}}{4}\left(\bar{\epsilon}^2 - \frac{\epsilon^2 l^2}{k_s^2 r^2}\right)\right]E_\varphi^{(0)}. \end{aligned} \quad (32)$$

The equation for the correction $B^{(2)}$ to the amplitude of the fundamental harmonic of the axial magnetic field of the wave is similar in structure to equation (15) for the fundamental-harmonic amplitude $B^{(0)}$, but its right-hand side is nonzero:

$$\begin{aligned} &\frac{1}{r}\frac{d}{dr}\left(\frac{r}{k_\perp^2}\frac{dB^{(2)}}{dr}\right) \\ &\quad + \left(1 - \frac{m^2}{k_\perp^2 r^2} + \frac{m}{r}\frac{d}{dr}\left(\frac{\mu}{k_\perp^2}\right)\right)B^{(2)} = \mathcal{L}^{(2)}(r), \end{aligned} \quad (33)$$

where

$$\begin{aligned} \mathcal{L}^{(2)}(r) &= -\frac{1}{r}\frac{d}{dr}\left[\frac{r}{k_\perp^2}(\mu G^{(2)}(r) + F^{(2)}(r))\right] \\ &\quad + \frac{m}{k_\perp^2 r}(G^{(2)}(r) + \mu F^{(2)}(r)). \end{aligned} \quad (34)$$

Equation (33) can also be solved by the method of varying a constant:

$$B^{(2)}(r) = A^{(2)} f_0(r) + g^{(2)}(r). \quad (35)$$

Here, $A^{(2)}$ is an integration constant and $g^{(2)}(r)$ is a particular solution to the inhomogeneous equation (33):

$$g^{(2)}(r) = D_1(r) f_0(r) + D_2(r) \tilde{f}_0(r), \quad (36)$$

where

$$D_1(r) = -\int_b^r \mathcal{L}^{(2)}(r) \tilde{f}_0(r) W_0^{-1}(f_0, \tilde{f}_0) dr, \quad (37)$$

$$D_2(r) = \int_0^r \mathcal{L}^{(2)}(r) f_0(r) W_0^{-1}(f_0, \tilde{f}_0) dr, \quad (38)$$

$\tilde{f}_0(r)$ is a solution to equation (15) that is linearly independent of $f_0(r)$ and has a singularity at $r = 0$, and the Wronskian W_0 of the functions $\tilde{f}_0(r)$ and $f_0(r)$ is $W_0(f_0, \tilde{f}_0) = f_0(r) df_0(r)/dr - \tilde{f}_0(r)\, df_0(r)/dr$.

In the second-order approximation, the boundary conditions give the following dispersion relation for an MHD wave in the helical magnetic field (1):

$$D^{(0)} + D^{(2)} = 0. \quad (39)$$

We seek a solution to (39) in the form $\omega = \omega_0 + \delta\omega$, where

$$\delta\omega = -D^{(2)}(\partial D^{(0)}/\partial\omega)^{-1}\Big|_{\omega = \omega_0} \quad (40)$$

and the second-order term $D^{(2)}$ is

$$D^{(2)} = \frac{k_\perp c}{\omega}\Bigg[\frac{l\epsilon}{2k_s b}(E_r^{(+)} - E_r^{(-)}) + \frac{i\bar{\epsilon}^2}{4k_s^2}\frac{d^2E_\varphi^{(0)}}{dr^2} + \left(\frac{i\epsilon\bar{\epsilon}}{2k_s}\left(1 + \frac{l^2}{k_s^2 b^2}\right) - \frac{i\bar{\epsilon}^2}{4k_s^2 b}\right)\frac{dE_\varphi^{(0)}}{dr} + \frac{i\bar{\epsilon}}{2k_s}\left(\frac{dE_\varphi^{(+)}}{dr} + \frac{dE_\varphi^{(-)}}{dr}\right) + -\frac{il^2(\bar{\epsilon}^2 - \epsilon^2)}{4k_s^2 b^2}E_\varphi^{(0)}\Bigg] + \frac{m\mu}{k_\perp b}g^{(2)} + \frac{1}{k_\perp}\frac{dg^{(2)}}{dr} + \frac{\mu G^{(2)} + F^{(2)}}{k_\perp}\Bigg|_{r = b}. \quad (41)$$

If the dependence $D^{(0)}(\omega)$ is not specified analytically [e.g., when the distribution $f_0(r)$ of the fields is found numerically], then the derivative $\partial D^{(0)}/\partial\omega$ can be evaluated from perturbation theory [10]:

$$\frac{\partial D^{(0)}}{\partial\omega} = \frac{c}{i\omega\varepsilon_\perp}\Bigg(-\frac{m}{r}\varepsilon_2^{(0)}\tilde{f}_0(b)\int_0^b \frac{f_0\hat{\Omega}f_0}{W_0}dr + \frac{mf_0}{r}\frac{\partial\varepsilon_2^{(0)}}{\partial\omega} + \frac{\partial(\varepsilon_1^{(0)} - N_Z^2)}{\partial\omega}\frac{df_0}{dr} - (\varepsilon_1^{(0)} - N_Z^2)\frac{d\tilde{f}_0}{dr}\int_0^b \frac{f_0\hat{\Omega}f_0}{W_0}dr\Bigg)_{\substack{r = b \\ \omega = \omega_0}}. \quad (42)$$

Here, the operator $\hat{\Omega}$ is

$$\hat{\Omega}f_0 = \frac{1}{r\varepsilon_\perp(\varepsilon_1^{(0)} - N_Z^2)}\frac{\partial\varepsilon_\perp}{\partial\omega}\frac{\partial}{\partial r}\left[r(\varepsilon_1^{(0)} - N_Z^2)\frac{df_0}{dr}\right] + \frac{1}{r\varepsilon_\perp(\varepsilon_1^{(0)} - N_Z^2)}\frac{\partial}{\partial r}\left[r\frac{\partial(\varepsilon_1^{(0)} - N_Z^2)}{\partial\omega}\frac{df_0}{dr}\right] - \frac{1}{(\varepsilon_1^{(0)} - N_Z^2)}\frac{\partial(\varepsilon_1^{(0)} - N_Z^2)}{\partial\omega}\frac{\partial\varepsilon_\perp}{\partial r}\frac{df_0}{dr} - \frac{1}{\varepsilon_\perp}\frac{\partial^2\varepsilon_\perp}{\partial r\partial\omega}\frac{df_0}{dr} + \frac{mf_0}{r\varepsilon_\perp(\varepsilon_1^{(0)} - N_Z^2)}\frac{\partial\varepsilon_\perp}{\partial\omega}\frac{\partial\varepsilon_2^{(0)}}{\partial r} + \frac{mf_0}{r(\varepsilon_1^{(0)} - N_Z^2)}\frac{\partial^2\varepsilon_2^{(0)}}{\partial r\partial\omega} - \frac{mf_0}{r\varepsilon_\perp(\varepsilon_1^{(0)} - N_Z^2)}\frac{\partial\varepsilon_2^{(0)}}{\partial\omega}\frac{\partial\varepsilon_\perp}{\partial r} - \frac{m\varepsilon_2^{(0)}f_0}{r\varepsilon_\perp(\varepsilon_1^{(0)} - N_Z^2)}\frac{\partial^2\varepsilon_\perp}{\partial r\partial\omega} - \frac{m^2f_0}{r^2\varepsilon_\perp}\frac{\partial\varepsilon_\perp}{\partial\omega} - \frac{m^2f_0}{r^2(\varepsilon_1^{(0)} - N_Z^2)}\frac{\partial(\varepsilon_1^{(0)} - N_Z^2)}{\partial\omega} + \frac{2\omega^2f_0}{c^2(\varepsilon_1^{(0)} - N_Z^2)}\frac{\partial\varepsilon_\perp}{\partial\omega} + \frac{2k_\perp^2}{\omega}f_0, \quad (43)$$

$$\varepsilon_\perp = (\varepsilon_1^{(0)} - N_Z^2)^2 - (\varepsilon_2^{(0)})^2.$$

The constant $A^{(2)}$ in (35) cannot be found exclusively from the boundary conditions. On the other hand, the structure of the dispersion relation (39) and correction (40) are independent of $A^{(2)}$. To evaluate the constant $A^{(2)}$, we must use a condition similar to the normalization condition for the wave function in perturbation theory in quantum mechanics. In our problem, this condition implies that the electromagnetic wave energies calculated in the zero- and second-order approximations are equal to each other.

6. SIMPLE ANALYTIC ESTIMATES

We employ the results obtained to study how the nonuniformity of the confining magnetic field affects the dispersion properties of MHD waves in a stellarator plasma with a uniform density profile. In this case, equation (15) for $B^{(0)}$ has an exact solution: $f_0(r) = J_m(k_\perp, r)$, where $J_m(k_\perp r)$ is the Bessel function. We consider

the propagation of axisymmetric ($m = 0$) small-scale ($k_\perp b \gg 1$) MHD waves in an $l = 2$ stellarator with a large pitch of the helical winding ($k_s b \ll 1$), in which case we have

$$D^{(0)} = J_0'(k_\perp b) = -J_l(k_\perp b). \quad (44)$$

For FMS waves with frequencies above the ion cyclotron frequency ($\Omega = \omega/\omega_{ci} \gg 1$) and with a long axial wavelength [$k_z/k_s \ll (k_A b/\Omega)^2$], the dispersion relation has the solution

$$\omega_0 \approx j_{1,s} c/(bN_A), \quad (45)$$

$$\delta\omega \approx \frac{\varepsilon^2}{2(k_s b)^3}\left(\left(\frac{\omega_{pi} b}{c}\right)^2 + \frac{8}{k_s b}\right)\omega_0, \quad (46)$$

where $j_{1,s}$ is the sth root of the first-order Bessel function, $J_1(j_{l,s}) = 0$.

For Alfvén waves having frequencies on the order of the ion cyclotron frequency and propagating nearly along the magnetic field ($k_z \gg k_A, j_{l,s}/b$), the correction to the frequency

$$\omega_0 \approx [1 - (k_A/k_z)^2]\omega_{ci} \quad (47)$$

has the form

$$\frac{\delta\omega}{\omega_{ci}} \approx -\frac{\varepsilon^2}{24}\frac{k_z^2}{k_A^2}\left\{\left(\frac{k_z b}{j_{l,s}}\right)^2 + \frac{1}{2}\left(\frac{j_{l,s}}{k_s b}\right)^2\right\}. \quad (48)$$

In deriving this correction, we assumed that $(k_z/k_A)^2(k_z b/j_{l,s})^2 \times (k_s b)^2/24 \gg 1$.

7. CONCLUSION

We have studied the propagation of MHD waves in a plasma inhomogeneous in three dimensions in a straight stellarator. We have shown that the symmetry of the confining magnetic field and the smallness of the current in the helical winding make it possible to reduce the problem of MHD eigenmodes in a stellarator plasma inhomogeneous in three dimensions to a problem that is inhomogeneous in one (radial) direction and has a well-known solution. We have found the distribution of RF fields with allowance for the first-order additive corrections to the amplitudes of the satellite harmonics [see (18), (19), and (24)–(27)]. We have determined the correction $\delta\omega$ (40) to the eigenfrequency of an MHD wave and have shown that this correction is a second-order quantity in the parameter ε [see (1)], characterizing the smallness of the helical-coil currents in comparison with the currents flowing in the solenoidal coils, which produce the toroidal magnetic field. We have derived simple asymptotic expressions (46) and (48) for the correction $\delta\omega$ in the case of a plasma with a uniform density profile. The smallness of this correction, $|\delta\omega| \ll \omega_0$, makes it possible to estimate the applicability range of the model of a straight magnetic field in studying MHD waves in stellarators.

It is well known that, in an axial magnetic field, the spectra of MHD oscillations of a plasma cylinder are degenerate with respect to the sign of the axial wavenumber k_z, $\omega_0(-|k_z|) = \omega_0(|k_z|)$. Consequently, in the resonant case in which the axial wavelength of an MHD wave is twice as long as the pitch of the helical winding ($2k_z - k_s$) and the azimuthal wavenumber is equal to one-half of the poloidal number of the helical-field periods ($2m = l$), the correction $\delta\omega$ may become infinitely large, because expression (28) for $A^{(\pm)}$ contains a resonant denominator (the problem of how to make the spectra of MHD waves nondegenerate in the resonant case with the help of a rippled magnetic field was investigated by Girka *et al.* [12]). However, the correction does not become larger because of the difference in the eigenfrequencies of the waves with opposite signs of the azimuthal wavenumber. In order of magnitude, the nonreciprocity effect for MHD waves with opposite signs of m can be estimated as

$$\omega_0(+|m|) - \omega_0(-|m|) \sim \frac{l}{(k_A(0)b)^2}\frac{\omega_0 + \omega_{ci}^{(0)}}{\omega_{ci}^{(0)}}\omega_0. \quad (49)$$

If the nonreciprocity effect for an MHD wave whose fundamental mode satisfies the resonance conditions $2k_z = k_s$ and $2m = l$ is sufficiently weak [i.e., the difference in (49) is much smaller than correction (40) estimated for an axisymmetric mode], then the above analysis cannot be applied to this wave: the effect of the nonuniformity of the stellarator magnetic field on the eigenfrequency should be described using the perturbation theory for degenerate spectra, in which case the correction to the eigenfrequency introduced by the magnetic field nonuniformity turns out to be a small (first-order) quantity.

ACKNOWLEDGMENTS

This work was supported by the Ministry of Science and Technology of Ukraine, project no. 2-4/700.

REFERENCES

1. A. V. Longinov and K. N. Stepanov, *High-Frequency Plasma Heating*, Ed. by A. G. Litvak (AIP, New York, 1991), p. 93.
2. A. G. Elfimov, A. G. Kirov, and V. P. Sidorov, in *High-Frequency Plasma Heating* (IPF AN SSSR, Gorki, 1983), p. 211.
3. V. E. Golant and V. I. Fedorov, *Methods of High-Frequency Plasma Heating in Toroidal Fusion Devices* (Énergoatomizdat, Moscow, 1986), p. 197.
4. F. J. Paoloni, Phys. Fluids **18**, 640 (1975).
5. Equipe TFR, in *Proceedings of 3rd Symposium on Plasma Heating in Toroidal Devices, Varenna, 1976 (Lectures and Contrib. Papers)*, p. 43.

6. A. M. Messiaen, R. R. Weynants, V. P. Bhatnagar, *et al.*, in *Proceedings of Joint Varenna–Grenoble International Symposium on Heating in Toroidal Plasmas, Grenoble, 1978*, Vol. 2, p. 229.

7. A. V. Longinov, K. N. Stepanov, and V. A. Tsurikov, in *Proceedings of 7th International Conference on Plasma Physics and Controlled Nuclear Fusion Research, Innsbruck, 1978*, Nucl. Fusion Suppl. **2**, 583 (1979).

8. E. D. Volkov, V. A. Suprunenko, and A. A. Shishkin, *Stellarator* (Naukova Dumka, Kiev, 1983), p. 312.

9. I. A. Girka, V. I. Lapshin, and K. N. Stepanov, Fiz. Plazmy **23**, 23 (1997) [Plasma Phys. Rep. **23**, 19 (1997)].

10. I. A. Girka, and K. N. Stepanov, Ukr. Fiz. Zh. **37**, 69 (1992).

11. S. Yu. Karpov and S. N. Stolyarov, Usp. Fiz. Nauk **163**, 63 (1993).

12. I. O. Girka, V. I. Lapshin, and K. N. Stepanov, Fiz. Plazmy **24**, 1015 (1998) [Plasma Phys. Rep. **24**, 948 (1998)].

Translated by I. A. Kalabalyk

Plasma Physics Reports, Vol. 26, No. 1, 2000, pp. 41–45. Translated from Fizika Plazmy, Vol. 26, No. 1, 2000, pp. 44–48.

DUSTY PLASMA

Longitudinal Low-Frequency Waves in the Flows of Self-Gravitating Charged Dust Grains in an Electron–Ion Plasma

P. V. Bliokh and V. V. Yaroshenko

Institute of Radioastronomy, National Academy of Sciences of Ukraine, Krasnoznamennaya ul. 4, Kharkov, 310002 Ukraine

Received January 20, 1999; in final form, May 6, 1999

Abstract—A study is made of the features of wave processes in the individual flows of self-gravitating dust grains in a plasma and the electric and gravitational interactions in a system of several dusty plasma flows. It is shown that, in a dusty plasma, Debye screening can substantially weaken the electric coupling between the beams of self-gravitating grains, without affecting the gravitational forces between them, and that the electrostatic perturbations are exchanged between the grain flows via gravitational fields, as happens in vacuum. *© 2000 MAIK "Nauka/Interperiodica".*

1. INTRODUCTION

Flows of charged dust grains are frequently encountered in the universe. Characteristic examples of such flows are planetary rings and comet tails, in which the particles interact with each other via electric and gravitational fields. If the density of charged grains is sufficiently high, then they can be regarded as a plasma component; the plasma in which the gravitational interaction is important is called a self-gravitational dusty plasma (SGDP).

The problem of the interaction between two flows of an SGDP was studied by Gisler *et al.* [1] under the assumption that the flows are unbounded and interpenetrating. Such a simplified model is unsuitable when the distance between the beams is large, as is usually the case in the universe. In our earlier papers [2, 3], we analyzed waves in a system of spatially separated beams of an SGDP in vacuum.

On the other hand, in reality, the beams are propagating in a space that is filled with an ion–electron plasma, in which case the overall picture of the interaction between dusty plasma flows changes substantially, because Debye screening has no impact on the gravitational interaction and the wave perturbations of the grain density are exchanged between the flows via gravitational fields, as they do in vacuum.

We should also take into account the fact that the oscillations of the charged grain density give rise to electric fields. Consequently, if the distance between the flows is not too large, the gravitational perturbations in one of the flows (due to, e.g., a massive body flying nearby) will induce space-charge waves in each of the remaining flows. Our purpose here is to study such wave perturbations.

2. LOW-FREQUENCY ELECTRIC AND GRAVITATIONAL FIELDS INSIDE AND OUTSIDE THE FLOW OF AN SGDP

We consider a cylindrical beam of radius a. Let the density of the grains (each having mass M and charge Q) in the beam be N. We assume that the entire space (including the region occupied by the beam) is filled with an electron–ion plasma. Let the densities of the plasma particles (whose charges are $\pm e$ and masses are m_e and m_i) be n_e and n_i. We will be interested in the waves whose frequencies are low enough that the electron and ion densities obey the Boltzmann distributions

$$n_e = n_0 \exp(e\Psi_E + m_e\Psi_G)/T,$$
$$n_i = n_0 \exp(-e\Psi_E + m_i\Psi_G)/T,$$

where Ψ_E and Ψ_G are the electric and gravitational potentials and n_0 and T are the unperturbed density and temperature of the plasma electrons and ions. Since the electron and ion masses, m_e and m_i, are small in comparison with the grain mass, the related quantities in the Boltzmann distributions can be neglected. We also consider small perturbations with respect to which the problem can be linearized, so that

$$n_{e,i} \simeq n_0(1 \pm e\Psi_E/T).$$

Another simplifying assumption is that there exists a constant, infinitely strong magnetic field aligned with the beam axis. This allows us to consider only longitudinal displacements of the charged particles, so that the space-charge waves in the dust plasma component can be described by a conventional set of equations, which consists of the equation of motion

$$\frac{\partial V}{\partial t} + V_0\frac{\partial V}{\partial z} = -\frac{Q}{M}\frac{\partial \Psi_E}{\partial z} - \frac{\partial \Psi_G}{\partial z} + \frac{F_{\text{ext}}}{M}, \qquad (1)$$

1063-780X/00/2601-0041$20.00 © 2000 MAIK "Nauka/Interperiodica"

the continuity equation

$$\frac{\partial N}{\partial t} + \frac{\partial}{\partial z}(N_0 V + N V_0) = 0, \quad (2)$$

the Poisson equation for the electrostatic potential

$$\Delta \Psi_E = -4\pi[QN + e(n_i - n_e)] \simeq -4\pi QN - \lambda_D^{-2}\Psi_E \quad (3)$$

(where $\lambda_D = \sqrt{T/8\pi n_0 e}$ is the plasma Debye radius), and the Poisson equation for the gravitational potential

$$\Delta \Psi_G = 4\pi GMN \quad (4)$$

(where G is the gravitational constant).

The gravitational interaction between the grains is incorporated into our model by introducing the gravitational acceleration $(-\partial\Psi_G/\partial z)$ into the equation of motion and through Poisson's equation for the gravitational potential Ψ_G.

The beam is assumed to be straight and sufficiently thin (the corresponding restrictions on the beam radius will be formulated below). We assume that the oscillatory and unperturbed velocities of the particles, V and V_0, are all constant over the entire beam cross section and are directed along the z-axis. In the acceleration associated with the external force F_{ext}, we also take into account only the z-components of the electric and gravitational fields,

$$-(Q/M)\partial\Psi_{E,\,\text{ext}}/\partial z - \partial\Psi_{G,\,\text{ext}}/\partial z.$$

We consider the wave perturbations that are produced by a Fourier component of the external force $F_{\text{ext}}(\omega, k)\exp[i(kz - \omega t)]$. We single out the factor $\exp[i(kz - \omega t)]$ in V, N, Ψ_E, and Ψ_G and pass over from equations (1) and (2) to a set of two algebraic equations. To do this, we take into account the fact that the longitudinal electric field in a filamentary beam is proportional to the linear charge-density gradient $\pi a^2 QN$, so that we have $\partial\Psi_E/\partial z = i\gamma_E k\pi a^2 QN$. A similar relationship is valid for the gravitational field, $\partial\Psi_G/\partial z = i\gamma_G k\pi a^2 GMN$. Here, the dimensionless coefficients γ_E and γ_G should be found by solving Poisson's equations (3) and (4).

First, we single out the oscillating factor $\exp[i(kz - \omega t)]$ in Ψ_E and N in order to convert equation (3) to the form

$$\frac{1}{r}\frac{d}{dr}\left(r\frac{d\Psi_E}{dr}\right) - p^2\Psi_E = \begin{cases} -4\pi NQ & (r < a) \\ 0 & (r > a), \end{cases} \quad (5)$$

where $p^2 = k^2 + 1/\lambda_D^2$. For Fourier amplitudes, we adopt the same symbols Ψ_E and N that were used above for the corresponding complete functions.

Neglecting variations in N over the beam cross section, we can readily obtain general solutions to equations (5) in terms of the modified Bessel functions I_μ and K_μ:

$$\Psi_E = C_1 I_0(pr) + C_2 K_0(pr) + 4\pi QN/p^2, \quad r \le a,$$

$$\Psi_E = C_3 I_0(pr) + C_4 K_0(pr), \quad r \ge a.$$

The integration constants C_i are found from the boundary conditions $\Psi_E(0) \neq \infty$ and $\Psi_E(\infty) = 0$ and from the condition that $\Psi_E(r)$ and $\Psi_E'(r)$ be continuous at $r = a$. As a result, we obtain

$$\Psi_E = \frac{4\pi QN}{p^2}\left[1 - \frac{K_1(pa)}{W(pa)} I_0(pr)\right], \quad r \le a, \quad (6)$$

$$\Psi_E = \frac{4\pi QN}{p^2}\frac{I_1(pa)}{W(pa)} K_0(pr), \quad r \ge a \quad (7)$$

where $W(pa) = K_0(pa)I_1(pa) + K_1(pa)I_0(pa)$ is the Wronskian for equation (5) at $r = pa$.

The expansion of Ψ_E in the limit $r \longrightarrow 0$ and its asymptotic behavior in the limit $r \longrightarrow \infty$ are

$$\Psi_E\big|_{r\to 0} \simeq \frac{4\pi QN}{p^2}\left[1 - \frac{K_1(pa)}{W(pa)}\left(1 + \frac{p^2 r^2}{4}\right)\right], \quad (8)$$

$$\Psi_E\big|_{r\to \infty} \simeq \frac{4\pi QN}{p^2}\frac{I_1(pa)}{W(pa)}\sqrt{\frac{\pi}{2pr}}\exp(-pr). \quad (9)$$

From (8), we can readily evaluate Ψ_E at the beam axis at small $pa \ll 1$, $\Psi_E(0) = -2\pi QNa^2\ln(pa)$, and find the coefficient $\gamma_E = -2\ln(pa)$. We can also formulate the condition for the beam to be "filamentary," $\left|\frac{\Psi_E(0) - \Psi_E(a)}{\Psi_E(0) + \Psi_E(a)}\right| \sim -\frac{1}{\ln(pa)} \ll 1$, where the variations in $\Psi_E(r)$ over the beam cross section should be small. As a result, we arrive at the condition $pa \ll 1$ and, for long-wavelength perturbations such that $k \ll \lambda_D^{-1}$ and $p \approx \lambda_D^{-1}$, we obtain $a \ll \lambda_D$, which indicates that the beam radius should be much smaller than the plasma Debye radius. Under these conditions, the potential Ψ_E can be approximated by

$$\Psi_E \simeq -2\pi QNa^2\ln(pa), \quad r \le a, \quad (10)$$

$$\Psi_E \simeq 2\pi QNa^2\sqrt{\frac{\pi}{2pr}}\exp(-pr), \quad r \gg a. \quad (11)$$

Equation (4) for Ψ_G can be solved in an analogous manner for the relevant parameters. We present here only the expression for $\Psi_G(0)$ and the asymptotic behavior of the gravitational potential in the limit $r \longrightarrow \infty$:

$$\Psi_G(0) = 2\pi GMNa^2\ln(ka), \quad (12)$$

$$\Psi_G|_{r\to\infty} = -2\pi GMNa^2\sqrt{\frac{\pi}{2kr}}\exp(-kr). \qquad (13)$$

From (12), we get $\gamma_G = 2\ln(ka)$. For the gravitational field, the condition for the beam to be filamentary is less restrictive than that for the electrostatic field: the potential $\Psi_G(r)$ can be assumed to be uniform over the entire beam cross section if $ka \ll 1$.

Figure 1 shows profiles of the potentials $\Psi_E(r/a)$ and $\Psi_G(r/a)$ for different values of pa and ka.

Given the coefficients γ_E and γ_G, we can easily write out the desired set of algebraic equations corresponding to (1) and (2):

$$V(kV_0-\omega) + 2ka^2N\left(-\frac{Q^2}{M}\ln(pa) + M\ln(ka)\right)$$
$$= -k\left(\frac{Q}{M}\Psi_{E,\,\mathrm{ext}} + \Psi_{G,\,\mathrm{ext}}\right),$$
$$VkN_0 + N(kV_0-\omega) = 0.$$

Here, as before, the functions and the related Fourier amplitudes are denoted by the same symbols. These equations have the solution

$$N = \frac{k^2N_0}{D}\left(\frac{Q}{M}\Psi_{E,\,\mathrm{ext}} + \Psi_{G,\,\mathrm{ext}}\right),$$
$$V = -\frac{k(kV_0-\omega)}{D}\left(\frac{Q}{M}\Psi_{E,\,\mathrm{ext}} + \Psi_{G,\,\mathrm{ext}}\right), \qquad (14)$$

where $D = (\omega - kV_0)^2 - \frac{k^2a^2}{2}[\ln(ka)\omega_G^2 - \ln(pa)\omega_p^2]$ is the determinant of the algebraic equations and $\omega_p = (4\pi Q^2N_0/M)^{1/2}$ and $\omega_G = (4\pi GMN_0)^{1/2}$ are the Langmuir and Jeans frequencies of the beam grains.

First, note that a purely gravitational perturbation ($\Psi_{E,\,\mathrm{ext}} = 0$) gives rise to an alternating electric field in the beam. In fact, substituting N from (14) into the formula $E_z = \partial\Psi_E/\partial z = i\gamma_E k\pi a^2QN$ yields

$$E_z = \frac{-2i\ln(pa)k^3\pi a^2QN_0}{D}\Psi_{G,\,\mathrm{ext}}.$$

Second, self-gravitation manifests itself as free oscillations in the beam. The dispersion relation for the natural oscillations follows from the condition $D = 0$,

$$(\omega - kV_0)^2 - \frac{k^2a^2}{2}[\ln(ka)\omega_G^2 - \ln(pa)\omega_p^2] = 0, \qquad (15)$$

which gives

$$\omega = kV_0 \pm \left\{\frac{k^2a^2}{2}[\ln(ka)\omega_G^2 - \ln(pa)\omega_p^2]\right\}^{1/2}$$
$$= kV_0 \pm \omega_{p,\,\mathrm{eff}}.$$

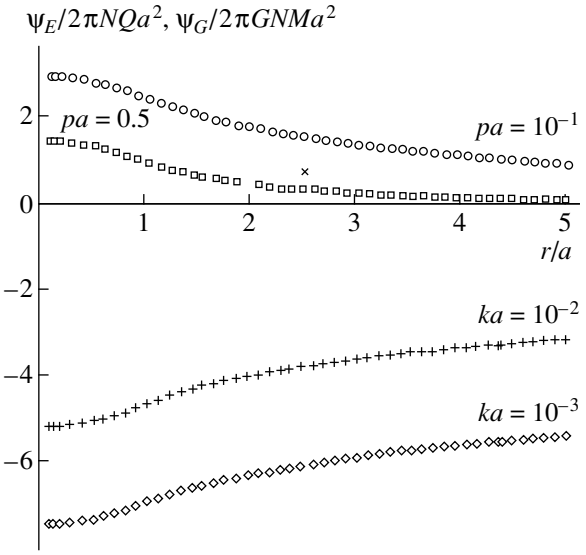

Fig. 1. Dimensionless potentials Ψ_E (above the abscissa) and Ψ_G (below the abscissa) versus the distance r/a for different values of pa and ka.

For $-\ln(pa)\omega_p^2 > \ln(ka)\omega_G^2$, this is the familiar dispersion relation but with a reduced effective Langmuir frequency of the beam. An interesting feature of the beam in an SGDP is the existence of a critical wavelength of perturbations, λ_{cr}, which corresponds to a zero effective Langmuir frequency of the beam ($\omega_{p,\,\mathrm{eff}} = 0$):

$$\lambda_{cr} \simeq \exp\left(-\frac{Q^2}{GM^2}\ln\left(\frac{a}{\lambda_D}\right)\right).$$

For $-\ln(pa)\omega_p^2 < \ln(ka)\omega_G^2$, the effective Langmuir frequency of the beam becomes imaginary, which corresponds to the Jeans instability of the beam with the growth rate $\nu = (ka/2)[-\ln(pa)\omega_p^2 + \ln(ka)\omega_G^2]^{1/2}$. The perturbations that are growing at this rate are carried away by the beam with the velocity V_0.

3. WAVE PERTURBATIONS IN A SYSTEM OF SEVERAL COLLINEAR BEAMS OF AN SGDP

Now, we analyze a more complicated system, i.e., one that consists of several narrow straight beams of charged dust grains of radius a. Let the beams be oriented along the z-axis and lie in the xz plane. Let the distance between neighboring beams be l. Since the entire space (including the regions occupied by the beams) is filled with a plasma, the beams interact with each other through electric and gravitational fields. We turn to formulas (10) and (11) to represent the electric potential of the resulting field inside the jth

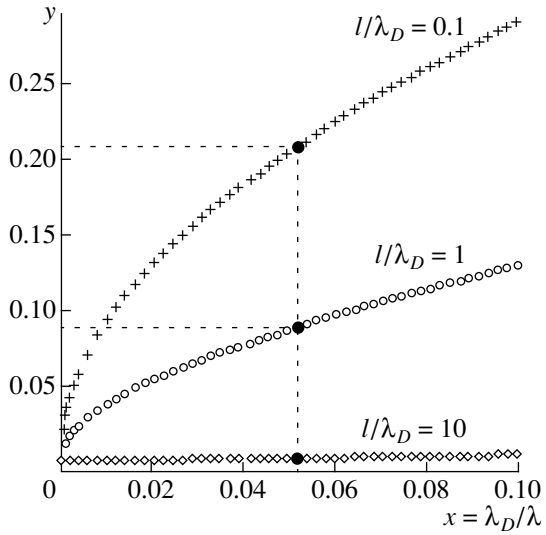

Fig. 2. The dependence $y(x) \sim \frac{N_2^F}{N_2^G}$ demonstrating a weakening of the electromagnetic forces with increasing the distance between the beams (the ratio l/λ_D).

beam as

$$\Psi_{E,j} \simeq -2\pi N_j Q a^2 \ln(pa) + \sum_{j\neq i} 2\pi Q N_i a^2 \sqrt{\frac{\pi}{2p|x_j - x_i|}} \exp(-p|x_j - x_i|), \quad (16)$$

where the first term on the right-hand side stems from the potential of the jth beam and the second term accounts for the contribution of the remaining beams (whose centers are at the points $x = x_i$ $(i \neq j)$) to the electric field at the point $x = x_j$. In order of magnitude, the number of electrically interacting beams is equal to λ_D/l.

The gravitational potential is described by a similar formula:

$$\Psi_{G,j} \simeq 2\pi G M N_j a^2 \ln(ka) - \sum_{j\neq i} 2\pi G M N_i a^2 \sqrt{\frac{\pi}{2k|x_j - x_i|}} \exp(-k|x_j - x_i|). \quad (17)$$

Note that the number of beams interacting gravitationally is larger and is proportional to $\sim\lambda/l \gg \lambda_D/l$ (of course, for long-wavelength perturbations, we have $\lambda \gg \lambda_D$).

A complete set of equations describing the longitudinal oscillations of interest to us consists of, first, the linearized equations of motion and the linearized continuity equations for dust grains in the beams [equations (1) and (2) should be written for each of the beams] and, second, equations (16) and (17), which couple the dust densities N_i in different beams and the electric and gravitational potentials, $\Psi_{E,j}$ and $\Psi_{G,j}$, in the selected beam. Since such a beam–plasma system is, as a rule, described by a very large number of equations, it cannot be analyzed directly from conventional approaches.

As a simple example, we consider two beams of an SGDP. Let V_{01} and V_{02} be the unperturbed velocities of the grain beams and N_{01} and N_{02} be their unperturbed densities. Let us assume that the external force $-(Q/M)\partial\Psi_{E,\text{ext}}/\partial z - \partial\Psi_{G,\text{ext}}/\partial z$ affects only the first beam. We can readily show that the perturbed density of each of the beams satisfies the set of algebraic equations

$$N_1 D_1 - N_2 \frac{k^2 a^2}{2}\left[\omega_{p1}^2 \sqrt{\frac{\pi}{2pl}}\exp(-pl) - \omega_{G1}^2 \sqrt{\frac{\pi}{2kl}}\exp(-kl)\right] = k^2 N_{01}\left(\frac{Q}{M}\Psi_{E,\text{ext}} + \Psi_{G,\text{ext}}\right), \quad (18)$$

$$N_2 D_2 - N_1 \frac{k^2 a^2}{2}\left[\omega_{p2}^2 \sqrt{\frac{\pi}{2pl}}\exp(-pl) - \omega_{G2}^2 \sqrt{\frac{\pi}{2kl}}\exp(-kl)\right] = 0, \quad (19)$$

where D_1 and D_2 are the determinants of the sets of equations describing the perturbations in each of the beams in an SGDP:

$$D_i = (\omega - kV_{0i})^2 + \frac{k^2 a^2}{2}[\ln(ka)\omega_{Gi}^2 - \ln(pa)\omega_{pi}^2], \quad i = 1, 2.$$

Although the external force acts only upon the first beam, the perturbation of its density,

$$N_1 = \frac{k^2 N_{01} D_2}{D_0}\left(\frac{Q}{M}\Psi_{E,\text{ext}} + \Psi_{G,\text{ext}}\right),$$

gives rise to electric and gravitational fields in the second beam, which, in turn, perturb its density,

$$N_2 = \frac{k^4 a^2 N_{01}}{2D_0}\left(\frac{Q}{M}\Psi_{E,\text{ext}} + \Psi_{G,\text{ext}}\right) \times\left[\omega_{p2}^2 \sqrt{\frac{\pi}{2pl}}\exp(-pl) - \omega_{G2}^2 \sqrt{\frac{\pi}{2kl}}\exp(-kl)\right], \quad (20)$$

where D_0 is the determinant of equations (18) and (19),

$$D_0 = D_1 D_2 - \frac{\pi k^4 a^4}{8}\left[\omega_{p1}^2 \sqrt{\frac{1}{pl}}\exp(-pl) - \omega_{G1}^2 \sqrt{\frac{1}{kl}}\exp(-kl)\right] \times\left[\omega_{p2}^2 \sqrt{\frac{1}{pl}}\exp(-pl) - \omega_{G2}^2 \sqrt{\frac{1}{kl}}\exp(-kl)\right].$$

According to (20), the perturbations of the density in the first beam induce the density perturbations in the second beam via electric and gravitational fields, so that we can write $N_2 = N_2^E + N_2^G$; moreover, the ratio

$$\frac{N_2^E}{N_2^G} \sim \frac{\omega_{p2}^2}{\omega_{G2}^2}\sqrt{k\lambda_D}\exp[-l(p-k)]$$

$$\sim \frac{Q^2}{GM^2}\sqrt{\frac{\lambda_D}{\lambda}}\exp\left[-\frac{l}{\lambda_D}\left(1-\frac{\lambda_D}{\lambda}\right)\right]$$

decreases as the distance l between the beams increases. We introduce the dimensionless variables $y = \frac{N_2^E}{N_2^G}\frac{GM^2}{Q^2}$ and $x = \frac{\lambda_D}{\lambda}$. Figure 2 shows the dependence $y(x)$ for different distances between the beams: $l = 0.1\lambda_D$, $l = \lambda_D$, and $l = 10\lambda_D$. We can see that, as l increases, the electromagnetic interaction between the beams sharply weakens, so that the wave perturbations of the density of the first beam perturb the density of the second beam mainly via gravitational fields.

Hence, Debye screening can substantially weaken electric coupling between the beams of dust grains in an SGDP, without affecting the gravitational forces, which thus might become dominant at distances as long as $l \gg \lambda_D$, even though the electric fields play a governing role in the interaction between closely spaced beams.

REFERENCES

1. G. R. Gisler, Q. Rushdy Ahmand, and E. R. Wollman, IEEE Trans. Plasma Sci. **20**, 922 (1992).
2. P. V. Bliokh, V. G. Sinitsin, and V. V. Yaroshenko, *Dusty and Self-Gravitational Plasmas in Space* (Kluwer, Dordrecht, 1995).
3. P. V. Bliokh and V. V. Yaroshenko, Astron. Zh. **62**, 569 (1985) [Sov. Astron. **29**, 330 (1985)].

Translated by O. E. Khadin

Plasma Physics Reports, Vol. 26, No. 1, 2000, pp. 46–53. Translated from Fizika Plazmy, Vol. 26, No. 1, 2000, pp. 49–56.

PLASMA INSTABILITIES

Excitation of Low-Frequency Electrostatic Oscillations in a Collisionless Plasma with an Anisotropic Ion Distribution

T. M. Burinskaya and E. M. Indenbom

Institute for Space Research, Russian Academy of Sciences, ul. Profsoyuznaya 84/32, GSP-7, Moscow, 117810 Russia

Received December 28, 1998; in final form, April 22, 1999

Abstract—The stability of an anisotropic ion distribution with unoccupied regions (holes) in velocity space is studied. Such distributions are expected to form near the neutral plane of the Earth's magnetotail. It is shown that, in such systems, electrostatic waves can be excited. The growth rate and propagation direction of these oscillations are determined by the parameters characterizing the ion hole, as well as by the relation between the electron and ion temperatures. The solution to the quasilinear equation for the waves propagating perpendicular to the current sheet is found, and the energy of the excited oscillations as a function of the parameters of the ion hole is evaluated. © *2000 MAIK "Nauka/Interperiodica".*

1. INTRODUCTION

Studies of the particle dynamics in a collisionless plasma have shown that the nonadiabatic motion of ions in the magnetic field reversal region leads to the formation of non-Maxwellian ion distributions [1–4]. Near the neutral sheet, such distributions are characterized by the presence of unoccupied (or strongly depleted) regions (holes) in velocity space, which are produced because ions with open (Speiser) trajectories leave the region of a low magnetic field. The specific property of this distribution function is an unusual orientation (with respect to the magnetic field) of the ion hole in velocity space. In contrast to the classical loss cone (whose axis is directed along the magnetic field), the unoccupied region typical of the velocity distribution function in question lies in the vicinity of the plane perpendicular to the magnetic field; moreover, this region is asymmetric with respect to the magnetic field direction. An analysis of the experimental data obtained when the Galileo spacecraft traveled near the current sheet of the Earth's magnetotail at distances from 35 to 87 Earth radii confirmed the non-Maxwellian nature of the ion distribution function, as well as the presence of ion holes in velocity space [5].

Previous investigations carried out for a narrow hole in velocity space [6] have shown that such functions are sources of free energy for the excitation of electrostatic oscillations, which, in turn, can affect physical processes in the plasma near the neutral sheet. The purpose of this study is to investigate the excitation of electrostatic oscillations in the neutral sheet of the Earth's magnetotail due to the presence of ion holes of arbitrary size in velocity space.

2. FORMULATION OF THE PROBLEM

Numerical simulation of the particle motion in the field of the Earth's magnetotail given by the Tsyganenko model [7] showed that the ion orbits in the plasma sheet are mainly of the closed type. Particles with such orbits repeatedly intersect the magnetic field reversal region; as a result, their distribution becomes isotropic and they fill the major part of phase space. The rest of the ions have strongly elongated orbits that are extended toward the Earth and, consequently, are efficiently carried away from the system. The rate of particle exchange between these two regions of phase space is relatively low [8]; this leads to the formation of ion holes in velocity space. The distribution function obtained by numerical calculations [1, 2] is plotted schematically in Fig. 1a. Here, we use the Sun–Earth magnetic coordinate system, in which the x-axis is directed along the Earth–Sun line, the z-axis is in the South–North direction (which is perpendicular to the current sheet), and the direction of the y-axis is chosen such that it forms a right-hand triple with the x- and z-axis. In order to describe such an ion distribution in velocity space, the distribution function is usually assumed to be Maxwellian in the region occupied by particles with closed trajectories. In our model, we assume that, outside this region, the ions are absent, because they are efficiently carried away from the system. The separating surface is taken to be a one-sheet hyperboloid with the angular parameter θ_0 and radius v_0; in the azimuthal direction, the separating surface is limited by the angle φ_0. In the spherical coordinate system (v, θ, φ), where the azimuthal angle φ is reckoned from the y-axis, this distribution function can be repre-

1063-780X/00/2601-0046$20.00

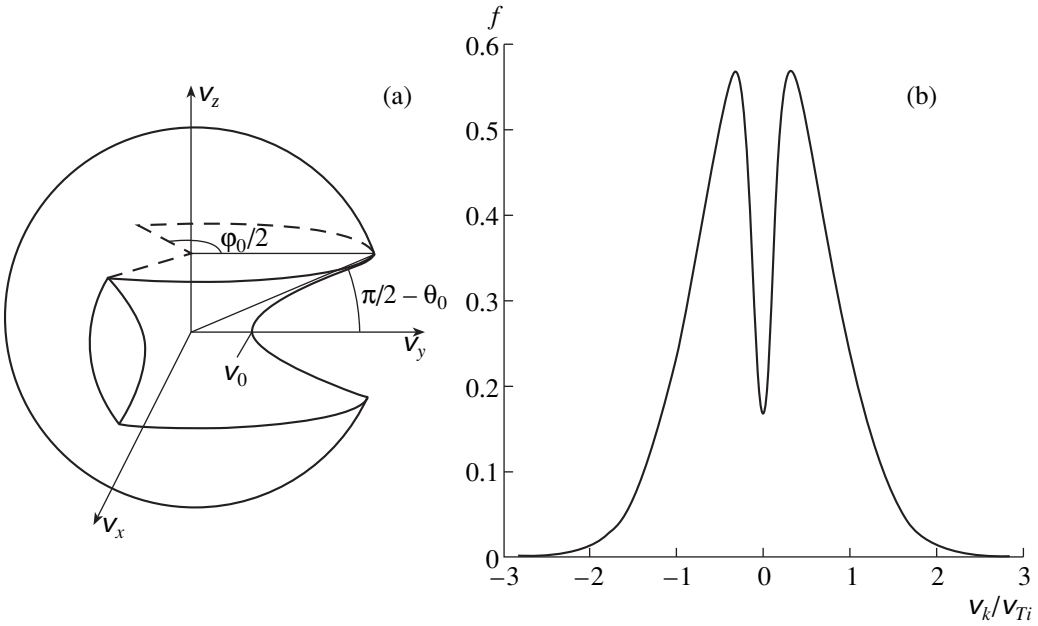

Fig. 1. (a) Sketch of a 3D ion distribution function with a hole in velocity space in the Sun–Earth magnetic coordinate system. Near the current sheet, the magnetic field is assumed to be directed from the South to the North (i.e., $B \approx B_z$). (b) Ion distribution function integrated with respect to v_x and v_y for waves propagating along the magnetic field: $\theta_0 = 80°$, $\varphi_0 = 270°$, and $v_0/v_{Ti} = 0.1$.

sented as

$$F_i(v, \theta, \varphi) = \begin{cases} 0 \quad \text{for} \quad |\varphi| < \varphi_0/2, \quad v^2\left(1 - \dfrac{\cos^2\theta}{\cos^2\theta_0}\right) \geq v_0^2 \\ \dfrac{\alpha n_i}{\pi^{3/2} v_{Ti}^3} e^{-v^2/v_{Ti}^2} \quad \text{in the opposite case.} \end{cases} \quad (1)$$

Here, $\alpha = \left(1 - \dfrac{\varphi}{2\pi} e^{-v_0^2/v_{Ti}^2} \cos\theta_0\right)^{-1}$ is the normalization coefficient and n_i and v_{Ti} are the density and thermal velocity of ions. In the model in question, the electrons are assumed to be Maxwellian with temperature T_e and density n_e. From the quasineutrality condition, it follows that $n_e = n_i = n_0$.

We assume that the plasma is uniform along all of the spatial coordinates. As follows from the results of the linear theory presented below, the characteristic wavelength of electrostatic oscillations excited due to the presence of ion holes in velocity space is on the order of several ion Debye lengths. Thus, the results obtained are applicable when the neutral-sheet thickness and the characteristic spatial scale of nonuniformities are substantially larger than the above value.

The ions and electrons can be considered unmagnetized, because, in the vicinity of the magnetic field reversal region, the ion gyrofrequency Ω_i is well below the ion plasma frequency ω_{pi} and $k_z v_z > \Omega_e$ (here, **k** is the characteristic wave vector of the excited oscillations and Ω_e is the electron gyrofrequency). Therefore, we can neglect the contribution from the electron rotation in the magnetic field to the plasma permittivity as compared to the contribution from the electron thermal motion.

3. LINEAR THEORY

3.1. Excitation of Waves Propagating along the Magnetic Field

From the numerical solution of the general dispersion relation (see Section 3.2), it follows that, when the ion hole in velocity space is sufficiently narrow in the polar direction, the waves with the wave vector directed along the *z*-axis have the largest growth rate. It is well known that a decisive role in the dynamics of electrostatic oscillations is played by the reduced (one-dimensional) distribution function obtained from the three-dimensional function by integrating with respect to the velocities perpendicular to the wave vector. In our case, for the reduced ion distribution function, we obtain

$$f_i(v_z) = \frac{\alpha n_0}{\sqrt{\pi} v_{Ti}} e^{-v_z^2/v_{Ti}^2} - \frac{\alpha n_{ir}}{\sqrt{\pi} v_{Tir}} e^{-v_z^2/v_{Tir}^2}, \quad (2)$$

where $v_{Ti} = \sqrt{2T_i/m_i}$ is the ion thermal velocity, $v_{Tir} = v_{Ti}\cos\theta_0$, and n_{ir} is given by the relation

$$n_{ir} = n_0(\varphi_0/2\pi)\cos\theta_0 e^{-v_0^2/v_{Ti}^2}.$$

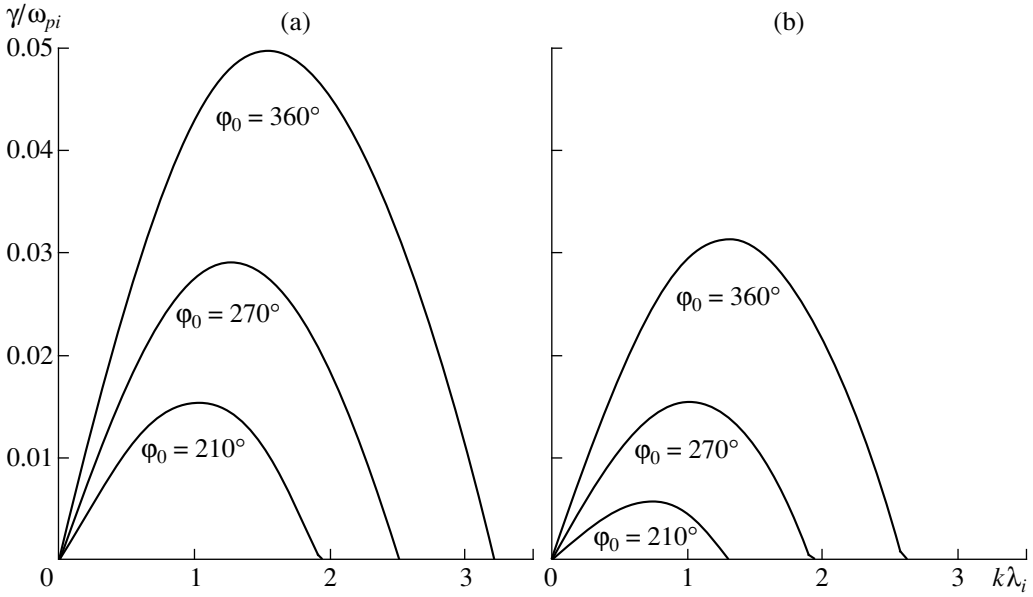

Fig. 2. Instability growth rate γ/ω_{pi} as a function of the wavenumber $k\lambda_i$ for waves propagating along the magnetic field for $T_i/T_e = 4$, $\theta_0 = 86°$, and different values of φ_0 at v_0/v_{Ti} = (a) 0 and (b) 0.5.

A typical reduced ion function $f_i(v_z)$ is shown in Fig. 1b.

By substituting the ion and electron distribution functions into the Penrose criterion [9], we obtain the criterion for the excitation of electrostatic waves in the z direction

$$\frac{\alpha\varphi_0}{2\pi\cos\theta_0}e^{-v_0^2/v_{Ti}^2} > \alpha + k_z^2\lambda_i^2 + \frac{T_i}{T_e}, \qquad (3)$$

where λ_i is the ion Debye length. From this criterion, it follows that, for $T_i > T_e$, the electrostatic oscillations are unstable at sufficiently small values of $\cos\theta_0$. Thus, we can assume that $\omega \ll kv_{Te}$ and $kv_{Ti}\cos\theta_0 \ll \omega \ll kv_{Ti}$. In this limit, the dispersion relation for electrostatic oscillations has the form

$$1 + \frac{1}{k_z^2\lambda_e^2} + \frac{\alpha}{k_z^2\lambda_i^2} + \frac{\alpha\varphi_0}{2\pi}\frac{\omega_{pi}^2\cos\theta_0}{\omega^2} = 0. \qquad (4)$$

The last term in this relation, which describes the contribution from the ion hole in velocity space, is analogous to the ion contribution in the limit of cold ions but has the opposite sign. It follows from here that there exists a solution with a zero real part of the frequency and the growth rate

$$\gamma = \omega_{pi}k_z\lambda_i\sqrt{\frac{\alpha\varphi_0\cos\theta_0}{2\pi(\alpha + k_z^2\lambda_i^2 + T_i/T_e)}}. \qquad (5)$$

In order to study the growth rate as a function of the parameters of the ion distribution (θ_0, φ_0, and v_0), we numerically solved the general dispersion equation. Figure 2 shows the growth rate normalized to the ion plasma frequency as a function of the wavenumber normalized to the reciprocal of the ion Debye length. The curves show the numerically calculated growth rate for different values of φ_0 at a fixed value of θ_0. The ratio between the ion and electron temperatures is taken to be four, which is typical of the Earth's magnetotail. From these figures, it is clearly seen that the growth rate decreases monotonically with both increasing v_0/v_{Ti} and decreasing φ_0; in both cases, the region of the wavenumbers corresponding to the instability decreases.

The greatest growth rate is attained for the angular parameter θ_0 of the ion hole in velocity space close to 90°. Figure 3 shows the values of the growth rate calculated numerically for different θ_0. The narrower the ion hole, the shorter the wavelength of excited oscillations. This is in agreement with estimate (3) for the maximum wavenumber of unstable oscillations obtained from the Penrose criterion.

3.2. Excitation of Waves Propagating Obliquely to the Magnetic Field

In order to study the stability of waves propagating obliquely to the magnetic field, it is necessary to calculate the corresponding reduced distribution function $f_i(v_k)$ for each wave vector. This function is equal to the integral of the 3D distribution function in velocity space over the plane perpendicular to the wave vector and passing through the point $v_k\mathbf{k}/|\mathbf{k}|$. In this case, the complete dispersion relation in the electrostatic limit is

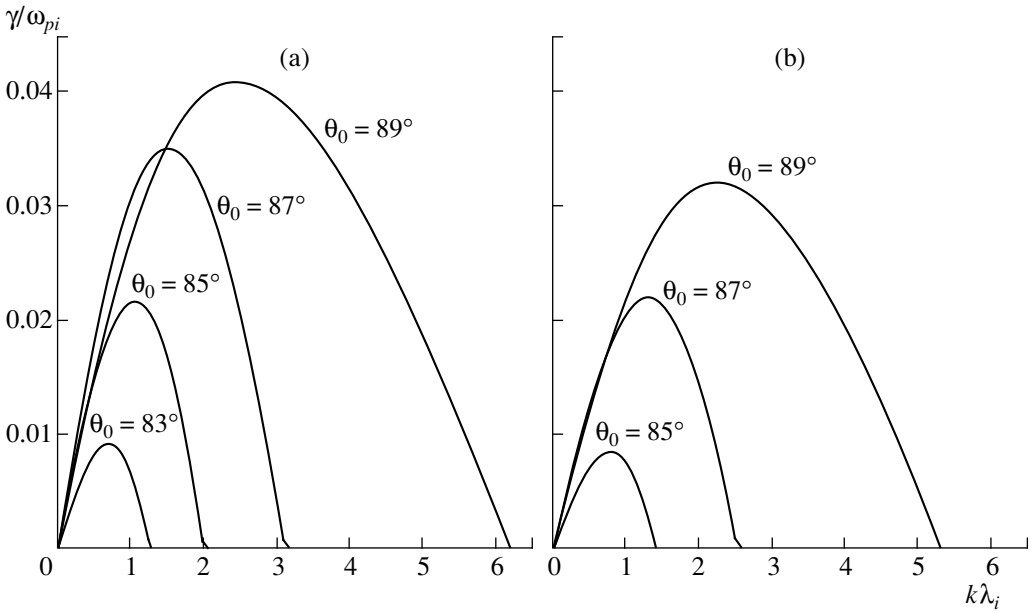

Fig. 3. Instability growth rate γ/ω_{pi} as a function of the wavenumber $k\lambda_i$ for waves propagating along the magnetic field for $T_i/T_e = 4$, $v_0/v_{Ti} = 0.1$, $\varphi_k = 0°$, and different values of θ_0 at φ_0 = (a) 270° and (b) 210°.

reduced to

$$1 + \frac{1}{k^2\lambda_e^2} - \frac{4\pi e^2}{M}\int_{-\infty}^{+\infty}\frac{f_i(v_k)dv_k}{(\omega - kv_k)^2} = 0. \qquad (6)$$

In order to find the range of the wave-vector angles θ_k at which electrostatic oscillations are unstable and determine how the parameters governing the shape of the ion velocity distribution affect the stability, dispersion relation (6) was solved under the assumption that the first term in this relation was small compared to the other terms. This means that we consider oscillations with wavelengths larger than the electron Debye length but much smaller than the electron gyroradius. In this case, the growth rate is proportional to k. Figure 4 shows the contours of the growth rate γ normalized to kv_{Ti} in the (θ_0, θ_k) plane (the ion-hole angular parameter versus the wave-vector polar angle). It is seen that, if the ion hole is sufficiently narrow in the polar direction and criterion (3) is satisfied, the maximum growth rate corresponds to oscillations with the wave vector parallel to the z-axis ($\theta_k = 0°$). If criterion (3) does not hold, but the angle θ_0 is still close to $\pi/2$, only the waves propagating obliquely to the magnetic field are unstable. A comparison of Figs. 4a and 4b plotted for the same plasma parameters (except for the ratio between the ion and electron temperatures) shows that the ratio T_i/T_e plays a decisive role in the onset of the instability. A double increase in this ratio leads to a drastic decrease in the size of the instability region. For the waves propagating along the magnetic field, this follows directly from criterion (3). The change of the parameters φ_0 and v_0/v_{Ti} of the ion distribution also leads to an appreciable change in the size of the instability region. Nevertheless, if the hole is axially symmetric (i.e., $\varphi_0 = 360°$), the effect of the temperature ratio is not very strong. With the same change in the temperature ratio as in the case of an asymmetric hole, the size of the instability region with respect to θ_k for an axially symmetric hole changes only slightly, although the magnitude of the growth rate appreciably decreases, as was shown in [10], in which the case of an axially symmetric hole was studied. When the symmetry around the magnetic field is disturbed ($\varphi_0 < 360°$), the size of the instability region decreases rapidly with decreasing φ_0. This dependence is seen from a comparison of Figs. 4b and 5a, which are plotted for the same plasma parameters, except for φ_0; the parameter φ_0 changes from 270° in Fig. 4b to 230° in Fig. 5a. The contours of γ/ω_{pi} in Fig. 5b were obtained by solving the general dispersion relation (6), including its first term, which was omitted in the other calculations. The curves are plotted in the (k_y, k_z) plane for $\theta_0 = 88°$. As follows from Fig. 5a, this value of θ_0 corresponds to the maximum value of the growth rate. The results presented in Fig. 5b show that the characteristic wavelength along the magnetic field is one order of magnitude less than the characteristic wavelength in the transverse direction.

Studies of the influence of the axial wave-vector angle φ_k on the excitation of electrostatic oscillations show that, if the ion hole is sufficiently narrow in the polar direction, the value of the growth rate changes slightly over the entire interval of angles φ_k. The corre-

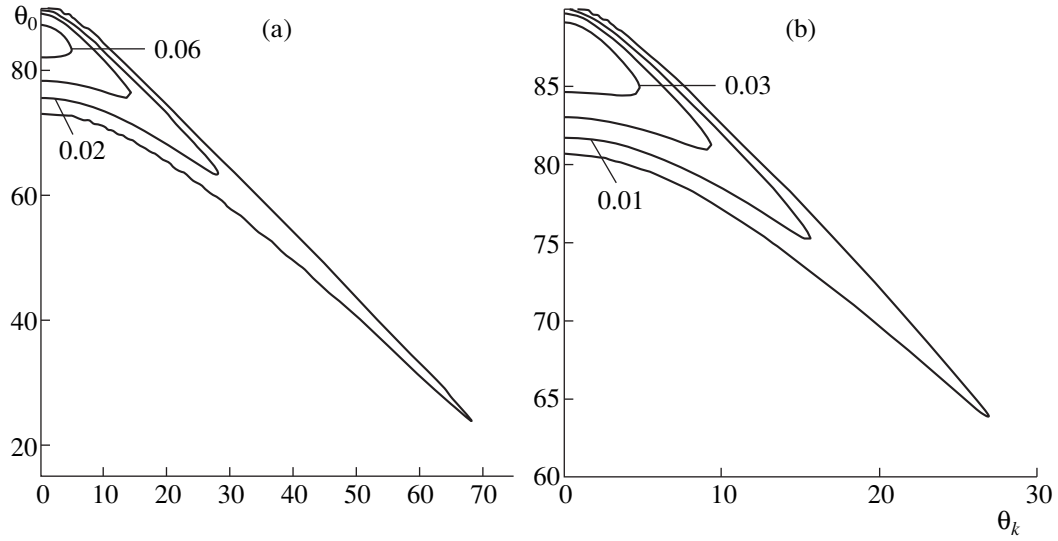

Fig. 4. Contours of the growth rate γ/kv_{Ti} in the (θ_k, θ_0) plane (the polar wave-vector angle vs. the ion-hole angular parameter) for $v_0/v_{Ti} = 0.1$, $\varphi_0 = 270°$, $\varphi_k = 0°$ at $T_i/T_e =$ (a) 2 and (b) 4.

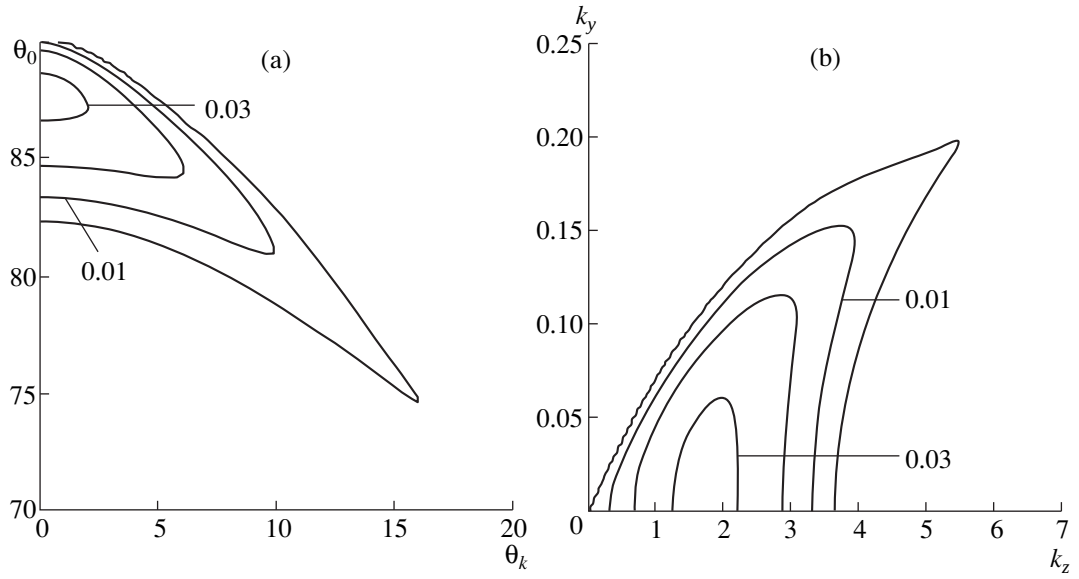

Fig. 5. Contours of the growth rate γ for $T_i/T_e = 4$, $v_0/v_{Ti} = 0.1$, $\varphi_0 = 230°$, $\varphi_k = 0°$ obtained from the solution of the general dispersion relation (6): (a) contours of γ/kv_{Ti} in the (θ_k, θ_0) plane and (b) contours of γ/ω_{pi} in the (k_y, k_z) plane for $\theta_0 = 88°$.

sponding numerical results are presented in Fig. 6a. For a sufficiently large width of the ion hole in the polar direction, when the waves propagating obliquely to the magnetic field are excited, the maximum growth rate increases with the axial angle φ_k, approaching 90°. In this case, the polar wave-vector angle θ_k corresponding to the maximum growth rate decreases. This dependence is clearly seen in Fig. 6b plotted for the same plasma parameters as in Fig. 6a, except for $\theta_0 = 70°$. It should be noted that the dependence of the growth rate on the axial angle φ_k is symmetric with respect to $\varphi_k = 90°$ because of the symmetry of the distribution function with respect to the $(v_y v_z)$ and $(v_x v_y)$ planes.

4. QUASILINEAR THEORY

The above results, obtained in the linear theory, show that the ion distribution functions (of the type shown in Fig. 1) with unoccupied regions in velocity space are unstable with respect to the excitation of electrostatic oscillations. Obviously, the influence of nonlinear effects on the wave dynamics increases with increasing the oscillation amplitude. The most impor-

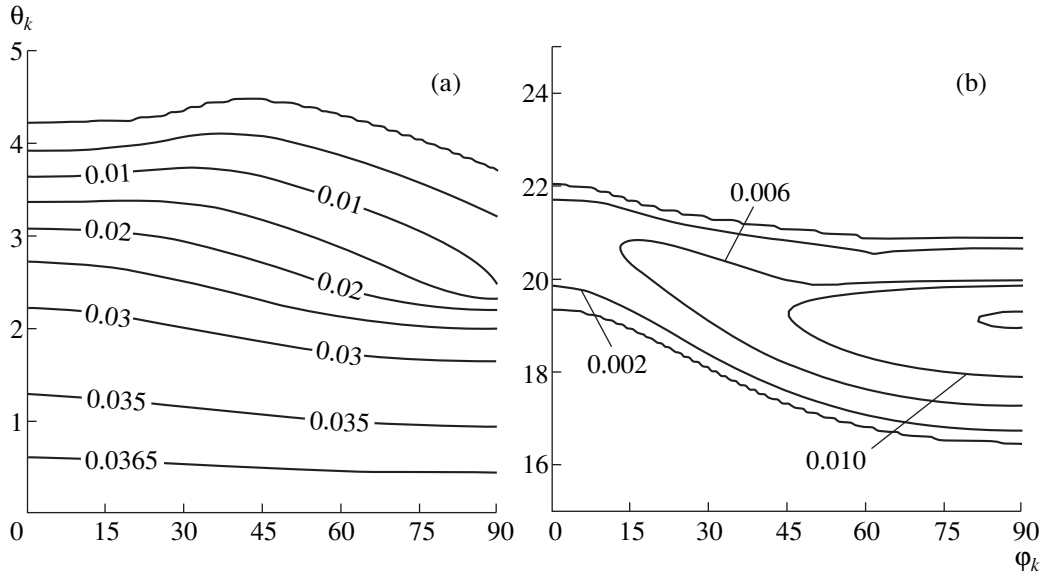

Fig. 6. Contours of the growth rate γ/kv_{Ti} in the (θ_k, φ_k) plane (the polar wave-vector angle vs. the azimuthal wave-vector angle) for $T_i/T_e = 4$, $v_0/v_{Ti} = 0.1$, $\varphi_0 = 270°$ at θ_0 = (a) 88° and (b) 70°.

tant nonlinear interaction in the system is the wave–particle interaction leading to a change in the ion distribution function. Since, in the case of the ion-hole instability, the excitation of oscillations is not related to the resonant wave–particle interaction and $\gamma(k) \ll kv_{Ti}$, we can use the quasilinear theory in the limit of nonresonant diffusion in velocity space. In this paper, we present the results of a quasilinear analysis only for waves propagating along the magnetic field, i.e., for the case when the ion hole in velocity space is located near θ close to 90°. In this case, the waves are excited in the direction almost parallel to the magnetic field; consequently, it is sufficient to study the relaxation of the reduced ion distribution function (2). According to [11], the ion diffusion in the velocity component v_z is described by the equation

$$\frac{\partial f_i}{\partial t} = \frac{e^2}{M^2}\frac{\partial}{\partial v_z}\sum_k \frac{d}{dt}\frac{1}{k^2 v_z^2}|E_k|^2\frac{\partial f_i}{\partial v_z}. \qquad (7)$$

This equation describes the interaction of all of the ions with a wave, but the efficiency of interaction is different for ions with different v_z. From equation (7), it follows in particular that the coefficient of quasilinear diffusion is substantially higher for ions with $v_z \longrightarrow 0$.

By introducing dimensionless variables

$$\varepsilon = \frac{e^2}{v_{Ti}^4 M^2}\sum_k \frac{|E_k|^2}{k^2}, \quad v = \frac{v_z}{v_{Ti}}, \qquad (8)$$

we can solve equation (7) in terms of the initial reduced ion distribution function (2) to obtain

$$f_i(\varepsilon, v) = \frac{\alpha n_0}{v_{Ti}} \times\left(G(\varepsilon, v) - e^{-v_0^2/v_{Ti}^2}\frac{\varphi_0}{2\pi}G\left(\frac{\varepsilon}{\cos^4\theta_0}, \frac{v}{\cos\theta_0}\right)\right), \qquad (9)$$

where

$$G(\varepsilon, v) = \frac{2^{1/4}\Gamma(3/4)}{\pi}|v|^{3/2} \times\int_0^\infty d\chi\chi^{1/4}J_{-3/4}(\chi v^2)e^{-4\chi^2\varepsilon}(1+\chi^2)^{-3/4}$$

and $J(x)$ is the Bessel function of the first kind.

From equation (9), it follows that, as the wave energy increases, a plateau is formed in the ion distribution function near $v_z = 0$. The wave energy increases as long as the ion distribution remains unstable with respect to the excitation of electrostatic oscillations. In order to estimate the saturation oscillation energy, we make use of the Penrose criterion [9], according to which a plasma with ion distribution (9) and Maxwellian electrons is unstable with respect to the excitation of electrostatic oscillations if and only if the following condition is satisfied:

$$\frac{\varphi_0}{2\pi}\frac{\alpha}{\cos\theta_0}e^{-v_0^2/v_{Ti}^2}I\left(\frac{\varepsilon}{\cos^4\theta_0}\right) - \alpha I(\varepsilon) > k^2\lambda_i^2 + \frac{T_i}{T_e}, \qquad (10)$$

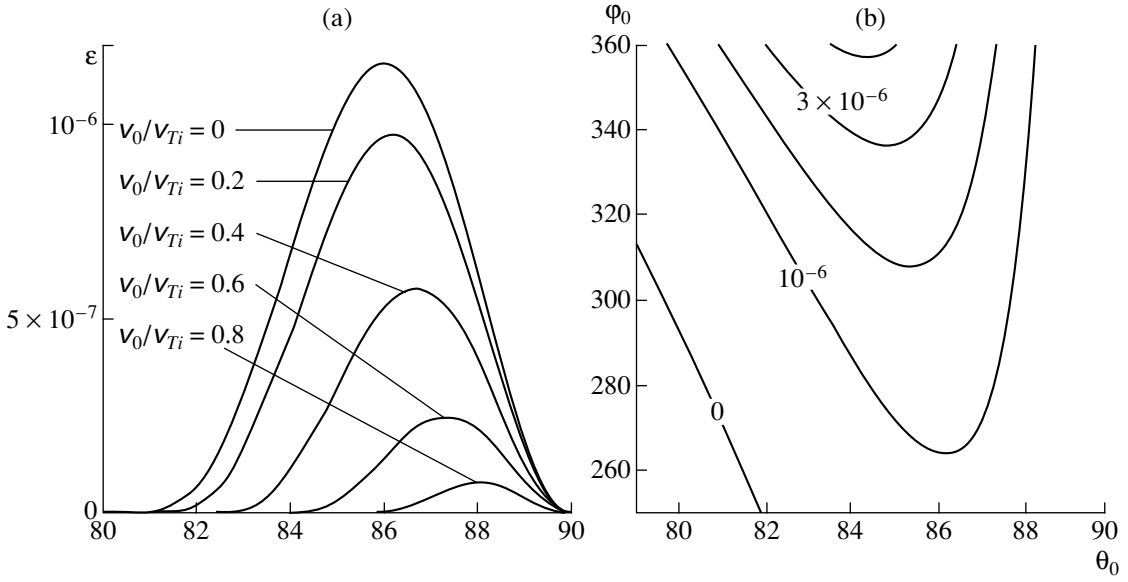

Fig. 7. (a) Normalized oscillation energy ε [see (8)] for the waves with $\theta_k = 0°$ as a function of the ion-hole angular parameter θ_0 for $T_i/T_e = 4$, $\varphi_0 = 270°$, and different values of v_0/v_{Ti}. (b) Contours of the normalized oscillation energy ε in the (θ_0, φ_0) plane for $v_0/v_{Ti} = 0.1$ and $T_i/T_e = 4$.

where

$$I(\varepsilon) = -\frac{1}{2}\int_{-\infty}^{+\infty} \frac{dv_z}{v_z}\frac{\partial G(\varepsilon, v_z)}{\partial v_z}.$$

From equations (9) and (10), we obtain that the saturation level leading to the formation of a plateau in the reduced ion distribution function in the region $0 \le v_z \le v_{Ti}$ is about $\varepsilon \approx \cos^4\theta_0$. Figure 7a shows ε in the state of a saturated instability as a function of the angular parameter θ_0 of the initial ion distribution for different values of $v_0/v_{Ti} = 0$, 0.2, 0.4, 0.6, and 0.8. Figure 7b shows the level of the saturation energy ε in the (φ_0, θ_0) plane. As was expected, the saturation oscillation energy strongly depends on the parameters of the ion hole in velocity space. Estimates show that, for plasma parameters typical of the neutral sheet of the Earth's magnetotail, the amplitude of the wave electric field can attain the value of the dawn–dusk electric field observed in this spatial region.

5. CONCLUSION

We have studied the stability of nongyrotropic ion distribution functions that can be formed in the neutral sheet of the Earth's magnetosphere against the excitation of electrostatic oscillations. The results obtained show that a plasma consisting of Maxwellian electrons and ions with the distribution function of the type shown in Fig. 1 is unstable against the excitation of electrostatic oscillations in a wide range of parameters of the ion hole in velocity space. When the ion hole is sufficiently narrow in the polar angle θ, electrostatic waves propagating along the magnetic field have the largest growth rate. The real part of the frequency of these waves is vanishingly small. As the angular parameter θ_0 of the hole decreases, the angle between the wave vector and the magnetic field at which the growth rate is maximum increases. The increase in the width of the ion hole in the polar direction also leads to an increase in the real part of the frequency. The typical wave frequency for the parameters of Fig. 5a is on the order of $0.1\omega_{pi}$ for waves with polar angle θ_k larger than 10°. The maximum growth rate for obliquely propagating oscillations is expected for waves propagating at the azimuthal angle $\varphi_k = 90°$. Our investigation showed that the excitation of waves propagating obliquely to the magnetic field is very sensitive to the plasma parameters. In particular, the plasma stability strongly depends on the ratio between the electron and ion temperatures. This effect is most pronounced in plasmas with a distorted symmetry of the ion distribution with respect to the magnetic field. The parameter φ_0 also strongly affects the size of the instability region for oscillations propagating obliquely to the magnetic field. Thus, we can conclude that the ion distribution with a hole in velocity space that is sufficiently wide in the polar angle can be stable against the excitation of electrostatic oscillations; however, the question of the stability of such distributions against the excitation of electromagnetic waves remains open.

The results obtained show that, when waves propagating along the magnetic field are excited (in other words, for a sufficiently narrow ion hole in velocity space), variations in the plasma parameters do not have such a strong effect on the system stability as in the case

of waves propagating obliquely to the magnetic field. Thus, the ion distribution functions under study can be an efficient source of electrostatic activity in the current sheet of the Earth's magnetotail. Apparently, as the oscillation amplitude grows, the role of nonlinear effects increases. In our case, the main nonlinear effect is the wave–particle interaction, which alters the initial ion distribution. The obtained solution to the equation for the quasilinear diffusion shows that the system is stabilized due to the trapping of low-energy ions and the formation of a plateau in the hole region of the initial reduced ion distribution. The saturation level of the excited oscillations is determined by the plasma parameters. For parameters typical of the neutral sheet of the Earth's magnetospheric tail, the amplitude of the saturated oscillations can attain the value of the dawn–dusk electric field. Obviously, in the quasisteady state, a balance must occur between the quasilinear ion diffusion in velocity space and the ion loss due to escape along the open trajectories. This loss was not taken into account in this study. Thus, we can expect that, in actual systems, the saturation level of electrostatic oscillations may be higher than that estimated by quasilinear theory.

ACKNOWLEDGMENTS

This work was supported in part by the Russian Foundation for Basic Research (project nos. 96-15-96723 and 97-02-16489) and INTAS (grant no. 96-2346).

REFERENCES

1. L. Zelenyi, A. Galeev, and C. F. Kennel, J. Geophys. Res. **95**, 3871 (1990).
2. M. Ashour-Abdalla, J. Büchner, and L. M. Zelenyi, J. Geophys. Res. **96**, 1601 (1991).
3. G. R. Burkhart, J. F. Drake, P. B. Dusenbery, and T. W. Speiser, J. Geophys. Res. **97**, 13799 (1992).
4. R. L. Kaufmann and C. Lu, J. Geophys. Res. **98**, 15 447 (1993).
5. L. A. Frank, W. R. Paterson, and M. G. Kivelson, J. Geophys. Res. **99**, 14863 (1994).
6. T. Burinskaya, D. Schriver, and M. Ashour-Abdalla, Geophys. Res. Lett. **21**, 2083 (1994).
7. N. A. Tsyganenko, Planet. Space Sci. **37**, 5 (1989).
8. D. L. Holland and J. Chen, Geophys. Res. Lett. **18**, 1579 (1991).
9. O. Penrose, Phys. Rev. **3**, 258 (1960).
10. T. Burinskaya, V. Pivovarov, E. Indenbom, *et al.*, J. Geophys. Res. **101**, 17337 (1996).
11. A. A. Galeev and R. Z. Sagdeev, in *Reviews of Plasma Physics*, Ed. by M. A. Leontovich (Atomizdat, Moscow, 1973; Consultants Bureau, New York, 1979), Vol. 7.

Translated by A. D. Smirnova

Plasma Physics Reports, Vol. 26, No. 1, 2000, pp. 54–61. Translated from Fizika Plazmy, Vol. 26, No. 1, 2000, pp. 57–64.

NONLINEAR PHENOMENA

Single-Mode Magnetic Structures in a Plasma with Anisotropic Pressure

V. Yu. Bychenkov*, A. I. Golubev, N. A. Ismailova**, M. D. Kamchibekov**, V. A. Terekhin**, V. T. Tikhonchuk*, and E. V. Uvarov****

**Lebedev Institute of Physics, Russian Academy of Sciences, Leninskiĭ pr. 53, Moscow, 117924 Russia*
***Russian Federal Nuclear Center, All-Russia Research Institute of Experimental Physics, Sarov, Nizhni Novgorod oblast, 607200 Russia*

Received November 4, 1998; in final form, March 20, 1999

Abstract—The equations of vortex electron anisotropic hydrodynamics are used to show that, in a plasma with anisotropic pressure, the Weibel instability of short-wavelength perturbations gives rise to a large-amplitude quasi-harmonic magnetic field varying periodically as a function of time. The computed field parameters agree well with the proposed analytic estimates. *© 2000 MAIK "Nauka/Interperiodica".*

1. INTRODUCTION

The study of nonlinear relaxation processes in systems that are far from equilibrium is an important problem in the physics of a rarefied nonequilibrium plasma. Since the collision frequency in such a plasma is low, the relaxation of plasma particles to an equilibrium distribution may be accompanied by the onset of various instabilities, during which the collective nonlinear properties of the plasma are especially pronounced.

Nonequilibrium plasma systems in which relaxation processes are governed by the excitation of intense longitudinal fields and their nonlinear interaction have been investigated very thoroughly. The literature on the systems that are unstable against transverse electromagnetic fields is much less extensive. Among such systems, we can mention, e.g., a plasma with an anisotropic electron energy distribution (an anisotropic plasma) [1].

So far, anisotropic plasmas have been studied using either a kinetic approach [2– 5] or approximate hydrodynamic models [6–10]. Bychenkov *et al.* [6] developed a quasi-hydrodynamic model based on the equations of vortex electron anisotropic hydrodynamics (VEAH). The choice of such a simplified approach, which was called the VEAH model, was motivated by the complexity of the kinetic plasma description. In order to make the proposed model adequate for the kinetic approach, it was constructed with allowance for the rich store of data acquired in modeling plasma processes in the context of collisionless hydrodynamics. The VEAH model for a collisionless plasma [6] makes it possible to analyze the dynamic properties of the electron plasma component with an anisotropic energy distribution (anisotropic pressure) using the set of equations for the magnetic field induction B_i and the electron pressure tensor P_{ij}.

Solutions to the VEAH equations (especially in the long-wavelength approximation, in which they take on a simpler form) were studied both analytically and numerically [6–10]. Bychenkov *et al.* [7] found that the results obtained by numerically solving the problem of the onset of long-wavelength ($kc/\omega_p \ll 1$, where k is the wavenumber, c is the speed of light, and ω_p is the plasma frequency) magnetic perturbations in a nonequilibrium unstable plasma with the help of the VEAH equations agree qualitatively with the results obtained from the kinetic modeling carried out with a bi-Maxwellian electron distribution [5]. We should, however, emphasize that both the applicability range of the VEAH equations and the class of problems to which they are applicable should be studied in more detail. This, primarily, refers to regimes in which the short-wavelength ($kc/\omega_p \sim 1$) Weibel instability forces perturbations to grow at the highest rates and which have not yet been studied in detail.

Our aim here is to further develop the theory of the nonlinear dynamics of the Weibel instability. We will investigate a short-wavelength regime by applying a relatively simple analytical model and by solving the VEAH equations numerically.

2. RESULTS OF NUMERICAL MODELING

In the one-dimensional approximation in which all of the quantities depend solely on x and only the y-component of the magnetic field and the xx-, xz-, and zz-elements of the pressure tensor are nonzero, the

1063-780X/00/2601-0054$20.00

VEAH equations have the form

$$\frac{\partial}{\partial t}\left(\Omega - \frac{\partial^2\Omega}{\partial x^2}\right) = \frac{\partial^2 P_{xz}}{\partial x^2}, \quad \frac{\partial P_{xx}}{\partial t} = -2P_{xz}\Omega,$$
$$\frac{\partial P_{zz}}{\partial t} = 2P_{xz}\left(\Omega - \frac{\partial^2\Omega}{\partial x^2}\right), \qquad (1)$$
$$\frac{\partial P_{xz}}{\partial t} = (P_{xx} - P_{zz})\Omega - P_{xx}\frac{\partial^2\Omega}{\partial x^2}.$$

Here, the dimensionless magnetic field Ω is expressed in units of $\sqrt{4\pi P_*}$, and the stress tensor elements, the coordinate, and the time are normalized, respectively, to P_*, c/ω_p, and $c/\omega_p\sqrt{P_*/m_e n_e}$, where m_e is the electron mass, n_e is the electron density, and P_* is an arbitrary normalizing pressure.

The VEAH equations (1) have the integral of motion $\det P_{ij} = P_{xx}P_{zz} - P_{xz}^2 = C(x)$ and the energy integral

$$\int dx\left(\Omega^2 + \left(\frac{\partial\Omega}{\partial x}\right)^2 + P_{xx} + P_{zz}\right) = \text{const}.$$

We solved equations (1) with the VEAH code (see Appendix). We imposed periodic boundary conditions at the boundaries of a region with the dimension $L = 4\pi$. At the initial instant, we set $P_{zz} = P_\perp = 1$, $P_{xx} = P_\parallel = 0.25$, and $P_{xz} = 0$. The magnetic field was chosen in the form of a spatially periodic perturbation $\Omega = \varepsilon\cos kx$ with the amplitude $\varepsilon = 10^{-2}$. In simulations, we varied the perturbation wavenumber k.

According to the linear theory of Weibel instability, a small initial perturbation of the magnetic field grows exponentially with time,

$$\Omega = \varepsilon\cosh[\gamma(k)t]\cos kx, \qquad (2)$$

at the rate

$$\gamma(k) = k\sqrt{\frac{P_\perp}{1+k^2} - P_\parallel}. \qquad (3)$$

Relationship (3) implies that the instability domain in wavenumber space is limited by the condition $k < k_M$ (where $k_M = \sqrt{P_\perp/P_\parallel - 1} = 1.73$) and the growth rate is maximum, $\gamma_m = 0.5$, at $k = k_m = 1$. In the region $k > k_M$, in which the growth rate $\gamma(k)$ is purely imaginary, the solutions for the magnetic-field perturbation Ω with a small initial amplitude are finite and can be obtained from linear theory.

In calculations, we varied k in the range $0 < k < k_M$, in which the solutions are unstable. Our simulations were aimed at revealing the characteristic features of unstable solutions in the nonlinear stage (for the magnetic field amplitudes $\Omega \sim 1$). An analysis of the numerical results allows us to draw the following two conclusions.

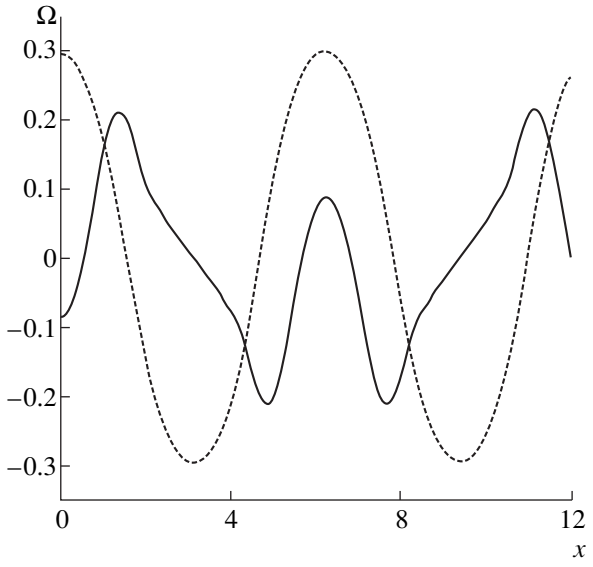

Fig. 1. Spatial profiles of the magnetic field at $t = 50$ for $k = 0.5$ (solid curve) and $k = 1$ (dashed curve).

(i) In the range $k_M/3 < k < k_M$, the solution depends on the spatial coordinate in a quasi-harmonic fashion over a fairly long time interval; the regimes in which the solutions behave in such a manner will be referred to as single-mode regimes.

(ii) In the range $0 < k < k_M/3$, the magnetic field, which is initially harmonic in character, is rapidly distorted because of the onset of higher harmonics, whose amplitudes grow to a level comparable with the amplitude of the initial mode.

Figure 1 illustrates spatial profiles of $\Omega(x)$ for two qualitatively different cases $k = 1$ and $k = 0.5$ at $t = 50$, which corresponds to sufficiently long time scales ($t \geq 20\gamma^{-1}$). In the long-wavelength case $k = 0.5$, the initial harmonic profile $\Omega(x)$ is seen to be distorted, whereas, in the short-wavelength case $k = 1$, it remains essentially unchanged.

The structure of the VEAH equations implies that, in the nonlinear stage, the instability causes the generation of odd spatial harmonics of the magnetic field with the wavenumbers $k_d = (2n+1)k$ ($n = 1, 2, \ldots$). From the necessary condition for stability of an arbitrary harmonic with wavenumber k_* ($k_* > k_M$), we obtain that all of the higher harmonics are stable if $\min\{k_d\} > k_M$. Consequently, the conditions under which the single-mode regime exists are $k < k_M$ and $\min\{k_d\} > k_M$, which can be rewritten as $k_M/3 < k < k_M$ by virtue of $\min\{k_d\} = 3k$. This conclusion was confirmed by our numerical simulations.

Figure 2 shows the time evolution of several Fourier harmonics of the magnetic field. In the short-wave-

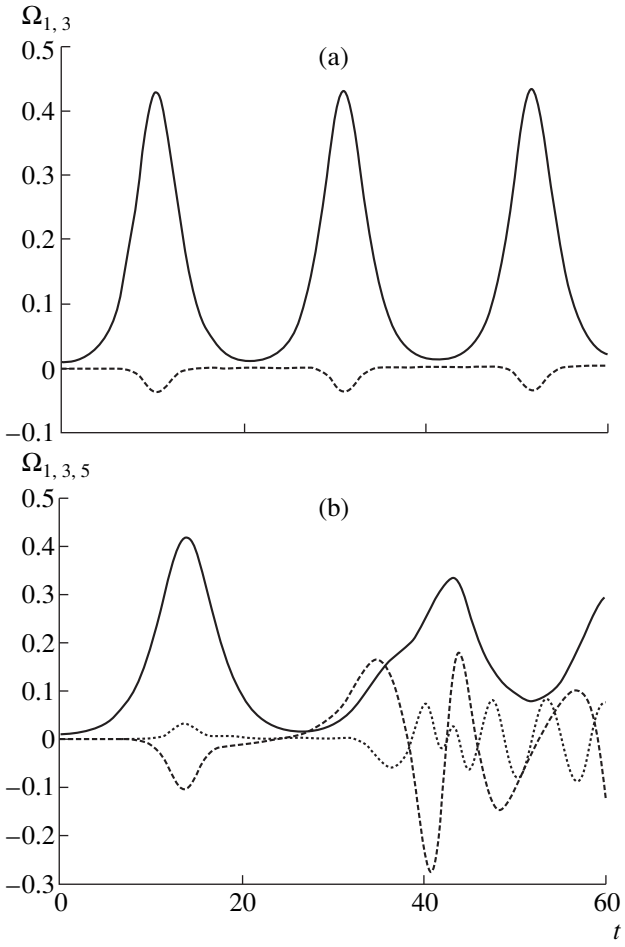

Fig. 2. Time evolution of the amplitudes of the spatial Fourier harmonics of the magnetic field in (a) the short-wavelength case, $k = 1$, and (b) the long-wavelength case, $k = 0.5$. The solid curve corresponds to the fundamental harmonic and the dashed and dotted curves, to the third and fifth harmonics, respectively.

length case $k = 1$ (Fig. 2a), the amplitudes of the Fourier harmonics are seen to be small in comparison with the amplitude of the seed perturbation, whereas the third-harmonic amplitude in the long-wavelength case $k = 0.5$ (Fig. 2b) grows rapidly and becomes comparable with the initial mode amplitude. Our simulations revealed a distinct boundary (at approximately $k_M/3$) between the long-wavelength and short-wavelength regimes in the space of wavenumbers k.

We consider the problem of the stability of a magnetic structure against small perturbations in the form of small-amplitude (noisy) harmonics in the single-mode regime. At first glance, it seems that the development of noisy harmonics should be described in terms of the linear theory of Weibel instability. In particular, if their wavenumbers are in the range $0 < k < k_M$, then they seem to grow at the rate (3). However, we will show below that, although the amplitudes of the noisy harmonics are small, linear theory fails to predict their time evolution because of the rapid growth of the fundamental mode amplitude. Let the initial magnetic perturbation be specified as $\Omega = \varepsilon_1\cos(kx) + \varepsilon_2\cos(2kx) + \varepsilon_3\cos(3kx)$, where the quantities ε_1, ε_2, and ε_3 differ in order of magnitude and the wavenumbers k are adjusted to lie within the instability domain $k < k_M/3$. A series of numerical simulations was carried out for $\varepsilon_1 = \varepsilon_2 = 10^{-8}$, $\varepsilon_3 = 10^{-2}$, and $k = 1/3$. As before, the initial pressure components were set to be $P_\perp = 1$ and $P_\parallel = 0.25$. Consequently, the third harmonic, which grows at the highest rate $\gamma_m = 0.5$, can be regarded as being fundamental, whereas the first and second harmonics, which are also within the instability domain, play the role of noisy harmonics. Figure 3 shows the time evolution of the amplitudes $\Omega_{1,2,3}(t)$ of the first three Fourier harmonics of the magnetic perturbation. We can see that, although the amplitudes of the noisy harmonics are small, they can be described in the linear approximation only when the fundamental mode is far from being saturated. That is why the time scales on which the single-mode regime breaks down turn out to be somewhat longer than those obtained from the prediction of the linear theory for the rate with which the noisy harmonics grow.

Our simulations revealed an interesting regime in which the time behavior of the fundamental mode with a wavenumber k lying in the range $k_M/3 < k < k_M$ depends on the initial amplitude of the stable noisy harmonic with $k_f = 3k$ ($k_f > k_M$). This regime is illustrated in Fig. 4, which shows the time evolution of $\Omega_{1,3}(t)$ for $k = 1$, $\varepsilon_1 = 10^{-3}$, and $\varepsilon_3 = 10^{-3}$, 5×10^{-3}, and 10^{-2}. At $\varepsilon_3 = 10^{-3}$, the amplitude $\Omega_1(t)$ varies periodically but does not change sign throughout the entire computation time. However, even at $\varepsilon_3 = 5 \times 10^{-3}$, the evolution of the first magnetic-field harmonic becomes more complicated. Consequently, varying the initial amplitude of the stable short-wavelength noisy harmonic makes it possible, in principle, to control the time evolution of the magnetic structure in the single-mode regime.

Hence, our simulations based on the VEAH model in which the initial magnetic perturbation is assumed to be harmonic revealed two essentially different regimes of Weibel instability. In the first regime, which refers to a short-wavelength ($k_M/3 < k < k_M$) initial perturbation, the spatial profile of the magnetic field is quasi-harmonic and the magnetic-field amplitude evolves in a strictly periodic fashion. In the presence of small-amplitude seed noisy harmonics with wavenumbers lying inside the instability domain, the harmonic structure of the magnetic field breaks down as time elapses. However, we have shown that linear theory gives incorrect estimates for the time during which the regular magnetic structure in this regime is disrupted: the magnetic field has been found to remain quasi-harmonic over time scales significantly longer than the characteristic time scale of the Weibel instability.

The time evolution of a long-wavelength ($0 < k < k_M/3$) initial perturbation in the course of Weibel insta-

bility is radically different. Higher harmonics that are generated in the nonlinear stage (the wavenumber $3k$ of the lowest of these harmonics turns out to lie within the instability domain) rapidly destroy the initial harmonic structure of the magnetic field. As a result, the picture of the process eventually becomes fairly complicated and stochastic.

3. ANALYTICAL MODEL

Now, we present a simple analytical model capable of describing the features of the plasma dynamics that were revealed with the help of the VEAH equations. It is natural to search for a spatially periodic solution to equations (1) in the form of a Fourier expansion in the x-coordinate, keeping a finite number of harmonics. We set

$$\Omega = \Omega_1\cos(kx) + \Omega_2\cos(2kx) + \Omega_3\cos(3kx),$$

$$P_{xz} = R_0 + R_1\cos(kx) + R_2\cos(2kx) + R_3\cos(3kx),$$

$$P_{xx} = A_0 + A_1\cos(kx) + A_2\cos(2kx) + A_3\cos(3kx),$$

$$P_{zz} = B_0 + B_1\cos(kx) + B_2\cos(2kx) + B_3\cos(3kx),$$

where the functions Ω_i, R_i, A_i, and B_i depend only on the time t.

Substituting these expressions into the basic equations (1) and neglecting the highest harmonics yields the following set of ordinary differential equations for Ω_i, R_i, A_i, and B_i:

$$\dot\Omega_1 = -\frac{k^2}{1+k^2}R_1, \quad \dot\Omega_2 = -\frac{4k^2}{1+4k^2}R_2,$$

$$\dot\Omega_3 = -\frac{9k^2}{1+9k^2}R_3, \quad \dot A_0 = -R_1\Omega_1 - R_2\Omega_2 - R_3\Omega_3,$$

$$\dot A_1 = -(2R_0 + R_2)\Omega_1 - (R_1 + R_3)\Omega_2 - R_2\Omega_3,$$

$$\dot A_2 = -(R_1 + R_3)\Omega_1 - 2R_0\Omega_2 - R_1\Omega_3,$$

$$\dot A_3 = -R_2\Omega_1 - R_1\Omega_2 - 2R_0\Omega_3,$$

$$\dot B_0 = R_1\Omega_1(1+k^2) + R_2\Omega_2(1+4k^2) + R_3\Omega_3(1+9k^2),$$

$$\dot B_1 = (2R_0 + R_2)\Omega_1(1+k^2) + R_1\Omega_2(1+4k^2),$$

$$\dot B_2 = (R_1 + R_3)\Omega_1(1+k^2) + 2R_0\Omega_2(1+4k^2) + R_1\Omega_3(1+9k^2),$$

$$\dot B_3 = R_2\Omega_1(1+k^2) + R_1\Omega_2(1+4k^2) + 2R_0\Omega_3(1+9k^2), \quad (4)$$

$$\dot R_0 = (1/2)[A_1\Omega_1(1+k^2) + A_2\Omega_2(1+4k^2) + A_3\Omega_3(1+9k^2) - B_1\Omega_1 - B_2\Omega_2 - B_3\Omega_3],$$

$$\dot R_1 = [A_0(1+k^2) - B_0]\Omega_1 + (1/2)[A_2\Omega_1(1+k^2) + (A_1 + A_3)\Omega_2(1+4k^2) + A_2\Omega_3(1+9k^2) - (B_1 + B_3)\Omega_2 - B_2(\Omega_1 + \Omega_3)],$$

$$\dot R_2 = [A_0(1+4k^2) - B_0]\Omega_2 + (1/2)[(A_1 + A_3)\times\Omega_1(1+k^2) + A_1\Omega_3(1+9k^2) - (B_1 + B_3)\Omega_1 - B_1\Omega_3],$$

$$\dot R_3 = [A_0(1+9k^2) - B_0]\Omega_3 + (1/2)[A_2\Omega_1(1+k^2) + A_1\Omega_2(1+4k^2) - B_2\Omega_1 - B_1\Omega_2].$$

We supplement these equations with the initial conditions

$$\Omega_1 = \varepsilon_1, \quad \Omega_2 = \varepsilon_2, \quad \Omega_3 = \varepsilon_3,$$

$$R_0 = R_1 = R_2 = R_3 = 0, \quad A_0 = a_0,$$

$A_1 = A_2 = A_3 = 0$, $B_0 = b_0$, $B_1 = B_2 = B_3 = 0$. In the linear approximation, equations (4) yield the condition $b_0 > a_0(1 + (nk)^2)$ for the nth harmonic to be unstable with the growth rate

$$\gamma_n^2 = \frac{(nk)^2}{1+(nk)^2}(b_0 - a_0(1 + (nk)^2)).$$

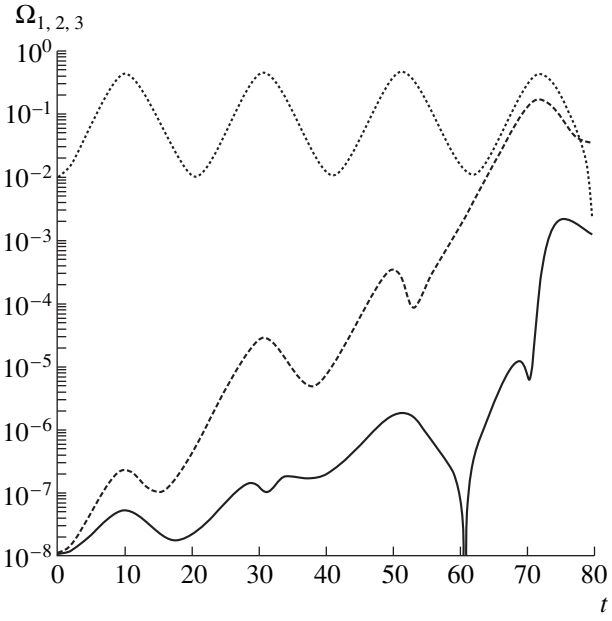

Fig. 3. Time evolution of the amplitudes of the first three harmonics of the magnetic field at $k = 1/3$, $\varepsilon_1 = \varepsilon_2 = 10^{-8}$, and $\varepsilon_3 = 0.01$. The solid curve corresponds to Ω_1 and the dashed and dotted curves, to Ω_2 and Ω_3, respectively.

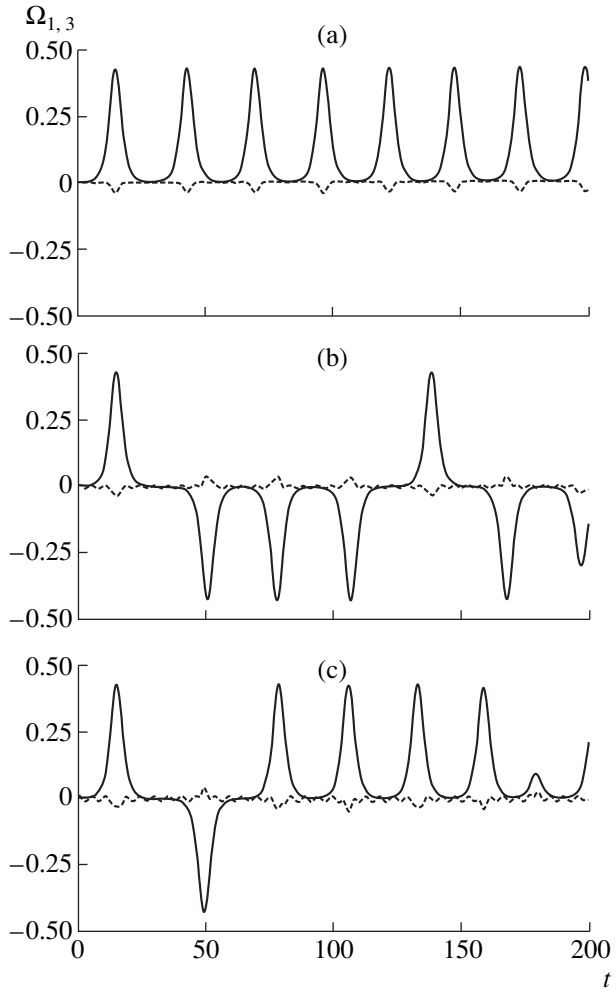

Fig. 4. Time evolution of the amplitudes $\Omega_{1,3}$ of the Fourier harmonics of the magnetic field at $k = 1$, $\varepsilon_1 = 0.001$, and $\varepsilon_2 = 0$ for different values of ε_3 = (a) 0.001, (b) 0.005, and (c) 0.01. The solid and dashed curves correspond to the first and third harmonics, respectively.

We consider a solution to equations (4) with the initial conditions

$$\Omega_1|_{t=0} = \varepsilon, \quad \Omega_2|_{t=0} = \Omega_3|_{t=0} = 0.$$

We can show that, under these conditions, the second harmonic is not generated and the amplitudes of the first and third harmonics satisfy the equations

$$\begin{aligned}\ddot{\Omega}_1 &= -\frac{k^2}{1+k^2}\{[(1+k^2)(A_0 + A_2/2) - (B_0 + B_2/2)]\Omega_1 \\ &\quad + (1/2)[(1+9k^2)A_2 - B_2]\Omega_3\}, \\ \ddot{\Omega}_3 &= -\frac{9k^2}{1+9k^2}\{[(1+9k^2)A_0 - B_0]\Omega_3 \\ &\quad + (1/2)[(1+k^2)A_2 - B_2]\Omega_1\},\end{aligned} \tag{5}$$

which will be solved iteratively. Setting $\Omega_3 = 0$ and turning to the relationships

$$A_0 = a_0 + (1/2)(1+k^{-2})(\Omega_1^2 - \varepsilon^2),$$

$$A_2 = (1/2)(1+k^{-2})(\Omega_1^2 - \varepsilon^2),$$

$$B_0 = b_0 - (1/2)(2+k^2+k^{-2})(\Omega_1^2 - \varepsilon^2),$$

$$B_2 = -(1/2)(1+k^2+k^{-2})(\Omega_1^2 - \varepsilon^2),$$

which follow from the equations for $A_{0,2}$ and $B_{0,2}$, we obtain the equation for Ω_1,

$$\ddot{\Omega}_1 - [\gamma_1^2 - (3/2)(1+k^2)(\Omega_1^2 - \varepsilon^2)]\Omega_1 = 0, \tag{6}$$

and, in the first approximation, the equation for Ω_3,

$$\begin{aligned}\ddot{\Omega}_3 - \left[\gamma_3^2 - \frac{9(1+k^2)(1+5k^2)}{1+9k^2}(\Omega_1^2 - \varepsilon^2)\right]\Omega_3 \\ = -\frac{9(1+k^2)}{2(1+9k^2)}(\Omega_1^2 - \varepsilon^2)\Omega_1.\end{aligned} \tag{7}$$

The first integral of equation (6) is

$$(\dot{\Omega}_1)^2 = \frac{3(1+k^2)}{4}(\Omega_1^2 - \varepsilon^2)\left(\varepsilon^2 + \frac{4\gamma_1^2}{3(1+k^2)} - \Omega_1^2\right).$$

Integrating this expression again, we obtain the solution for the first harmonic of the magnetic field in terms of an elliptic integral:

$$\frac{\sqrt{3(1+k^2)}}{2}t = \int_{\varepsilon}^{\Omega_1} \frac{dy}{\sqrt{(y^2 - \varepsilon^2)(\Omega_{1\max}^2 - y^2)}}. \tag{8}$$

Consequently, the first-harmonic amplitude, which is found to be a bounded periodic function of time, varies in the range

$$\varepsilon^2 < \Omega_1^2 < \Omega_{1\max}^2 = \varepsilon^2 + \frac{4\gamma_1^2}{3(1+k^2)}$$

with the period

$$T = \frac{4}{\sqrt{3(1+k^2)}} \int_{\varepsilon}^{\Omega_{1\max}} \frac{dy}{\sqrt{(y^2 - \varepsilon^2)(\Omega_{1\max}^2 - y^2)}}.$$

For the parameter values $a_0 = 0.25$, $b_0 = 1$, $\varepsilon_0 = 10^{-2}$, and $k = 1$, which correspond to the initial parameter values presented in the previous section, we obtain $\Omega_{1\max} = 0.41$ and $T = 20.4$. This agrees well with the results of solving equations (1) numerically. Figure 5 shows the time evolution of $\Omega_{1,3}(t)$ traced by solving equations (5) with the initial conditions $k = 1$, $\varepsilon_1 = 10^{-2}$, and $\varepsilon_3 = 0$. A qualitative agreement with the numerical results

illustrated in Fig. 2a justifies the use of the single-mode approximation.

For $\varepsilon \ll 1$, the approximate solution (6) can be written in explicit form:

$$\Omega_1(t) = \sum_{n=0}^{\infty} \frac{\Omega_{1\max}}{\cosh(\Omega_{1\max}\sqrt{3(1+k^2)/4}(t-t_n))},$$

where $t_n = (n + 1/2)T$. As ε decreases, the distance between the maxima increases according to the law $T \sim \ln(\Omega_{1\max}/\varepsilon)$, and the soliton-like character of the solution becomes more and more pronounced. For small ε, the function Ω_1 is very different from zero in narrow intervals around t_n. Equation (7) implies that, outside these intervals, the evolution of $\Omega_{1,3}$ can be described by linear theory, whereas, inside them, Ω_1 and Ω_3 are closely coupled.

Now, we consider the evolution of the magnetic structure in a single-mode regime in which the initial magnetic perturbation is represented by two noisy harmonics whose amplitudes are of the same order of magnitude and by the fundamental harmonic. Assuming, for definiteness, that the third harmonic plays the role of the fundamental one, we set

$$\varepsilon_1 = \varepsilon_2 \ll \varepsilon_3.$$

Omitting small higher order quantities in equations (4), we can write the equation for the quasi-stable magnetic field harmonic,

$$\ddot{\Omega}_3 + \frac{9k^2}{1+9k^2}\Big[a_0(1+9k^2) - b_0 + \Big(1+\frac{1}{9k^2}\Big)(1+9k^2)(\Omega_3^2 - \varepsilon_3^2)\Big]\Omega_3 = 0,$$

(whose solution we have already analyzed) and the set of coupled equations for the amplitudes of the noisy harmonics,

$$\ddot{\Omega}_1 = -\frac{k^2}{1+k^2}\Big[A_0(1+k^2) - B_0 + \frac{1+9k^2}{2}\Omega_3^2\Big]\Omega_1 + \frac{k^2}{1+k^2}\frac{\Omega_3}{2}\Big[(1+9k^2)\varepsilon\varepsilon_3 + \frac{2+k^2}{1+k^2}B_2\Big],$$

$$\ddot{\Omega}_2 = -\frac{4k^2}{1+4k^2}\Big[A_0(1+4k^2) - B_0 + \frac{1+9k^2}{2}\Omega_3^2\Big]\Omega_2 + \frac{4k^2}{1+4k^2}\frac{\Omega_3}{2}\Big[(1+9k^2)\varepsilon\varepsilon_3 + \frac{2(1+2k^2)}{1+4k^2}B_1\Big],$$

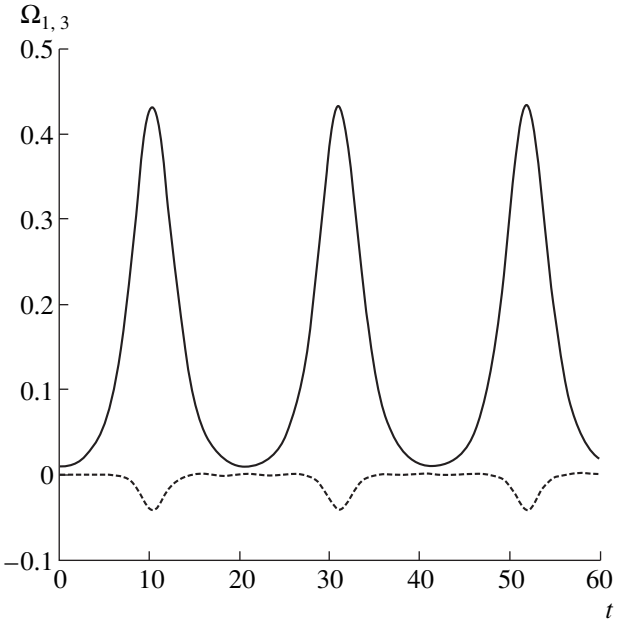

Fig. 5. Time evolution of the amplitudes $\Omega_{1,3}$ of the Fourier harmonics of the magnetic field in accordance with the solutions to equations (5) at $k = 1$, $\varepsilon_1 = 0.01$, and $\varepsilon_3 = 0$. The solid and dashed curves correspond to Ω_1 and Ω_3, respectively.

$$\dot{B}_1 = -\Big(1+\frac{1}{4k^2}\Big)\dot{\Omega}_2\Omega_3(1+9k^2) - \Big(1+\frac{1}{9k^2}\Big)\dot{\Omega}_3\Omega_2(1+4k^2),$$

$$\dot{B}_2 = -\Big(1+\frac{1}{k^2}\Big)\dot{\Omega}_1\Omega_3(1+9k^2) - \Big(1+\frac{1}{9k^2}\Big)\dot{\Omega}_3\Omega_1(1+k^2),$$

with the initial conditions $\Omega_1 = \Omega_2 = \varepsilon$, $\dot{\Omega}_1 = \dot{\Omega}_2 = 0$, and $B_1 = B_2 = 0$. Here, A_0 and B_0 are known functions of Ω_3,

$$A_0 = a_0 + \frac{1}{2}\Big(1+\frac{1}{9k^2}\Big)(\Omega_3^2 - \varepsilon_3^2),$$

$$B_0 = b_0 - \frac{1}{2}\Big(1+\frac{1}{9k^2}\Big)(1+9k^2)(\Omega_3^2 - \varepsilon_3^2).$$

When the fundamental harmonic amplitude is far from being maximum, the equation set we have obtained splits into independent equations corresponding to the linear approximation. However, for $\Omega_3 \sim \Omega_{3\max}$, the equations derived are coupled through the Ω_3-dependent functions A_0, B_0, B_1, and B_2, in which case the time evolution of the noisy harmonics differs from that predicted by linear theory, even though their amplitudes are relatively small.

4. CONCLUSION

In studying the dynamics of a Weibel plasma, we have revealed a single-mode regime of the generation of an intense magnetic field whose amplitude changes periodically as a function of time. This regime refers to a short-wavelength periodic initial perturbation, in which case the excited higher spatial harmonics are stable in the linear approximation.

In practice, the phenomenon we have investigated is of interest from the standpoint of the possibility of amplifying weak periodic magnetic fields, without disturbing their harmonic spatial structure.

Strictly speaking, such an amplified magnetic signal can exist only for a finite time, because it is unstable against long-wavelength modes. However, the characteristic "lifetime" of the amplified signal is significantly longer than the time scale on which its amplitude varies and even more so the time scale on which the Weibel instability develops. This circumstance allows us to speak of the existence of single-mode magnetic structures in plasmas with anisotropic electron pressure.

ACKNOWLEDGMENTS

This work was supported in part by the International Science and Technology Center (project no. 310) and the Russian Foundation for Basic Research (project nos. 96-02-16707-a and 96-02-16165-a).

APPENDIX

Numerical Scheme

In order to minimize the number of indices, we introduce the new notation $P_{xx} = u$, $P_{zz} = v$, $P_{xz} = W$, and $\varphi = \Omega - \frac{\partial^2 \Omega}{\partial x^2}$, in which the VEAH difference equations have the form

$$\frac{\partial \varphi}{\partial t} = \frac{\partial^2 W}{\partial x^2}, \quad \frac{\partial W}{\partial t} = u\varphi - v\Omega,$$
$$\frac{\partial u}{\partial t} = -2W\Omega, \quad \frac{\partial v}{\partial t} = 2W\varphi. \tag{A.1}$$

Bychenkov *et al.* [7] solved the VEAH equations numerically using an explicit three-layer scheme of second-order accuracy in time and space. However, our test simulations have shown that the condition for the scheme to be stable puts rather stringent restrictions on the time step. We solved equations (A.1) numerically with the following fairly reliable and quite effective algorithm.

Let the mesh $\omega = \{x_i, i = 1, 2, \ldots, N, x_1 = 0, x_N = L\}$ be specified on the closed interval $[0, L]$ and let all of the quantities in (A.1) be assigned to the mesh points. Equations (A.1) are approximated by the difference scheme

$$\frac{\varphi_i^{n+1} - \varphi_i^n}{\Delta t} = \alpha \delta W_i^{n+1} + (1-\alpha)\delta W_i^n \quad (2 \le i \le N-1),$$
$$\frac{u_i^{n+1} - u_i^n}{\Delta t} = -(W_i^{n+1} + W_i^n)\Omega_i \quad (1 \le i \le N),$$
$$\frac{v_i^{n+1} - v_i^n}{\Delta t} = (W_i^{n+1} + W_i^n)\varphi_i \quad (1 \le i \le N),$$
$$\frac{W_i^{n+1} - W_i^n}{\Delta t} = \frac{1}{2}[(u_i^{n+1} + u_i^n)\varphi_i - (v_i^{n+1} + v_i^n)\Omega_i] \tag{A.2}$$
$$(1 \le i \le N),$$
$$\varphi_i = \Omega_i - \delta\Omega_i,$$
$$\Omega_i = \beta\Omega_i^{n+1} + (1-\beta)\Omega_i^n.$$

Here, δW_i and $\delta\Omega_i$ denote the difference analogues of the second derivative, e.g.,

$$\delta\Omega_i = \frac{2}{x_{i+1} - x_{i-1}}\left[\frac{\Omega_{i+1} - \Omega_i}{x_{i+1} - x_i} - \frac{\Omega_i - \Omega_{i-1}}{x_i - x_{i-1}}\right];$$

and α and β are certain given parameters lying in the interval $0 \le (\alpha, \beta) \le 1$. In order to be closed, equations (A.2) should be supplemented with the boundary conditions for $i = 1$ and N. For a uniform mesh with a spatial step h, the scheme is accurate to the second order in h. For $\alpha = \beta = 0.5$, the scheme is also accurate to the second order in Δt. For other α and β values, it is accurate to $O(\Delta t + h^2)$.

We can readily see that, for any β value, the integral of motion (see Section 2) for the difference equations is exactly conserved, as is the case with the VEAH equations. At $\alpha = \beta = 0.5$, the energy conservation law is also satisfied for the difference scheme on a spatially uniform mesh ω. An analysis of the stability of the difference scheme shows that, if the step h of the mesh ω is chosen to satisfy the condition $\sin^2(kh/2)/(kh/2)^2 \simeq 1$ for the k values of interest to us, then the stability and instability domains for the difference scheme in wavenumber space will essentially coincide with those for the differential equations in the VEAH model.

REFERENCES

1. E. S. Weibel, Phys. Rev. Lett. **2**, 83 (1959).
2. R. L. Morse and C. W. Nielson, Phys. Fluids **14**, 830 (1971).
3. R. C. Davidson and D. A. Hammer, Phys. Fluids **14**, 1452 (1971).

4. R. C. Davidson and D. A. Hammer, Phys. Fluids **15**, 317 (1972).

5. V. Yu. Bychenkov, V. N. Novikov, V. P. Silin, and V. T. Tikhonchuk, Fiz. Plazmy **17**, 463 (1991) [Sov. J. Plasma Phys. **17**, 272 (1991)].

6. V. Yu. Bychenkov, V. P. Silin, and V. T. Tikhonchuk, Fiz. Plazmy **15**, 706 (1989) [Sov. J. Plasma Phys. **15**, 407 (1989)]; Phys. Lett. A **138**, 127 (1989); Zh. Éksp. Teor. Fiz. **98**, 1269 (1990) [Sov. Phys. JETP **71**, 709 (1990)].

7. V. Yu. Bychenkov, V. N. Novikov, and V. P. Silin, Fiz. Plazmy **17**, 830 (1991) [Sov. J. Plasma Phys. **17**, 485 (1991)].

8. V. P. Silin, Phys. Lett. A **160**, 201 (1991).

9. V. Yu. Bychenkov and V. N. Novikov, Fiz. Plazmy **23**, 726 (1997) [Plasma Phys. Rep. **23**, 670 (1997)].

10. F. Pegoraro, S. V. Bulanov, F. Califano, and M. Lontano, Phys. Scr. **63**, 262 (1996).

Translated by O. E. Khadin

Plasma Physics Reports, Vol. 26, No. 1, 2000, pp. 62–69. Translated from Fizika Plazmy, Vol. 26, No. 1, 2000, pp. 65–72.

NONLINEAR PHENOMENA

Dissipation-Free Jumps for the Magnetosonic Branch of Cold Plasma Motion

I. B. Bakholdin

Keldysh Institute of Applied Mathematics, Russian Academy of Sciences, Miusskaya pl. 4, Moscow, 125047 Russia

Received May 29, 1998; in final form, January 21, 1999

Abstract—Dissipation-free jumps are studied in a hydrodynamic model of a cold plasma moving at about magnetosonic speed. The jumps described by the generalized Korteweg–de Vries equation, which possesses similar nonlinear and dispersion properties, are considered. In particular, jumps with emission and solitonlike jumps are considered. The assumption that our model possesses jumps of the same type as those for the generalized Korteweg–de Vries equation is justified by numerically investigating the problem of the decay of an initial discontinuity in a cold plasma. An analytic method is described that makes it possible to predict the structure of such jumps in the general case. © *2000 MAIK "Nauka/Interperiodica".*

1. BASIC MODEL

One-dimensional motion of a cold quasineutral plasma is described by the set of equations [1]

$$\begin{aligned}
&\frac{\partial n}{\partial t} + \frac{\partial (nu)}{\partial x} = 0,\\
&\frac{du}{dt} + n^{-1}\frac{\partial}{\partial x}[(B_y^2 + B_z^2)/2] = 0,\\
&\frac{dv}{dt} - n^{-1}B_x\frac{\partial B_y}{\partial x} = -R_e^{-1}\frac{d}{dt}\left(n^{-1}\frac{\partial B_z}{\partial x}\right),\\
&\frac{dw}{dt} - n^{-1}B_x\frac{\partial B_z}{\partial x} = R_e^{-1}\frac{d}{dt}\left(n^{-1}\frac{\partial B_y}{\partial x}\right),\\
&\frac{dB_y}{dt} - B_x\frac{\partial v}{\partial x} + B_y\frac{\partial u}{\partial x} = R_i^{-1}\frac{\partial}{\partial x}\left(\frac{dw}{dt}\right),\\
&\frac{dB_z}{dt} - B_x\frac{\partial w}{\partial x} + B_z\frac{\partial u}{\partial x} = -R_i^{-1}\frac{\partial}{\partial x}\left(\frac{dv}{dt}\right),
\end{aligned} \tag{1}$$

where $\frac{d}{dt} = \frac{\partial}{\partial t} + u\frac{\partial}{\partial x}$, x is an independent variable, n is the ion density, $\mathbf{B} = (B_x, B_y, B_z)$ is the magnetic induction, and $\mathbf{v} = (u, v, w)$ is the ion velocity. These quantities are normalized, respectively, to the characteristic length l, the unperturbed plasma density n_0, the unperturbed magnetic field $\mathbf{B}_0$, and the Alfvén speed $V_A = |\mathbf{B}_0|/\sqrt{4\pi n_0(m_i + m_e)}$ (where m_i and m_e are the ion and electron masses). The dispersion parameters R_i and R_e are defined as $R_i = \omega_{ic}/\omega_0$ and $R_e = \omega_{ec}/\omega_0$, where ω_{ic} and ω_{ec} are the ion and electron cyclotron frequencies and $\omega_0 = V_A/l$ is the frequency characteristic of the phenomenon under discussion. For convenience, we can set l such that $\omega_0 = \sqrt{\omega_{ic}\omega_{ec}}$; consequently, we have $R_i = \sqrt{\omega_{ic}/\omega_{ec}}$ and $R_e = \sqrt{\omega_{ec}/\omega_{ic}} = \sqrt{m_i/m_e} \gg 1$. The magnetic field component B_x is constant (independent of x). In an unperturbed state, the unknown quantities n, u, v, w, B_x, B_y, and B_z are equal, respectively, to 1, 0, 0, 0, $\cos\theta$, $\sin\theta$, and 0. The wave is assumed to propagate along the x-axis at an angle θ to the magnetic induction vector.

The dispersion curve $\omega = \omega(k)$ for the linearized version of these equations consists of magnetosonic and Alfvén branches; in the case of waves propagating from left to right, the phase velocities for these branches are [1]

$$\begin{aligned}
V = [&\sqrt{(1+\cos\theta)^2 + \{(R_eR_i^{-1} + R_iR_e^{-1})\cos^2\theta + \sin^2\theta + 2\cos\theta\}R_i^{-1}R_e^{-1}k^2}\\
&\pm\sqrt{(1-\cos\theta)^2 + \{(R_eR_i^{-1} + R_iR_e^{-1})\cos^2\theta + \sin^2\theta + 2\cos\theta\}R_i^{-1}R_e^{-1}k^2}]/[2(1 + R_i^{-1}R_e^{-1}k^2)].
\end{aligned} \tag{2}$$

A linearized version of the basic equations also describes degenerate slow magnetosonic (SMS) branches (corresponding to the double root $\omega = 0$). Here, we are interested in wave phenomena associated with the fast magnetosonic (FMS) branch. Figure 1 shows the dispersion curves of magnetosonic waves propagating from left to right in a hydrogen plasma. The curves are plotted in the frame running from left to

1063-780X/00/2601-0062$20.00 © 2000 MAIK "Nauka/Interperiodica"

right at a speed equal to unity (i.e., at the speed of long-wavelength magnetosonic waves) for $\theta = 1.555$ and 1.535, for which the computations described in Section 4 were carried out. The dashed curve represents the Alfvén branch, which essentially coincides with the straight line $\omega/k = -1$ in the interval of k values in Fig. 1. For $\theta > \theta_c = \tan^{-1}(\sqrt{R_e/R_i} - \sqrt{R_i/R_e})$, the magnetosonic branch (curve *1* in Fig. 1) has no inflection points at $k > 0$; this corresponds to solitary waves [2]. For $\theta < \theta_c$, the magnetosonic branch (curve *2* in Fig. 1) has an inflection point at $k > 0$, so that solitary waves are absent (they can exist only in the asymptotic approximation [3]). The initial profiles of the shape of a solitary wave are smeared as time elapses due to the appearance of short-wavelength emission [4] at the wavelength that, in the first approximation, is determined by the value k_* at the point where the dispersion curve intersects the straight line $U = \omega/k$, where U is the speed of a solitary wave.

2. DISSIPATION-FREE JUMPS

Let us illustrate the dissipation-free jump using as an example the following two numerical self-similar solutions [5] to a simple equation similar to the generalized Korteweg–de Vries (KdV) equation:

$$a_t + aa_x + b_3 a_{xxx} + b_5 a_{xxxxx} = 0. \qquad (3)$$

2.1. Solution with a Solitonlike Jump

In the region between two states a_1 and a_2 (in the wave zone), the solution is oscillatory in nature. At one of the boundaries of the wave zone, a sequence of the wave maxima passes over to a sequence of solitary waves as $t \longrightarrow +\infty$. At the other boundary, the amplitude with which the solution oscillates gradually approaches zero. As time elapses, the solution for the wave zone acquires the nature of a self-similar solution: the wave envelope depends on x/t. The jump in question has no structure in the common sense; however, a solitary wave at the boundary can be formally regarded as the jump structure. The state on one side of the jump is described by the set of averaged equations for the wave zone, and the state on the other side, by the conventional simplified equation $a_t + aa_x = 0$. Note that the related solution to the conventional KdV equation was called the nonsteady structure of a collisionless shock wave and was studied by Gurevich and Pitaevskiĭ [6]. Here, we will say a few words about the terminology: although such a solution is, as a whole, nonlocal and depends on time, it is time-independent at the boundary of the wave zone. In our study, any localized transitions between homogeneous, periodic, quasiperiodic, and stochastic states are regarded as jumps.

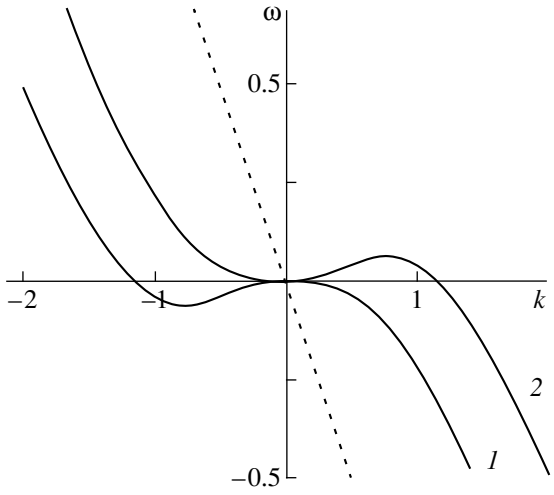

Fig. 1. Dispersion curves for a cold plasma.

2.2. Solution with a Jump with Emission

In this case, the wavelength at the corresponding boundary of the wave zone is finite. The solution has a local jump: on one side of the jump, the state is homogeneous, and the state on the other side corresponds to a homogeneous periodic wave. The wave zone includes a homogeneous wave subzone whose length increases with time and a subzone of the centered simple wave envelope (where the wave amplitude falls off to zero).

Solitonlike jumps can be captured by numerically solving the problem of the decay of an initial discontinuity only when $b_2 b_3 < 0$ (if the amplitude of the initial discontinuity is sufficiently small), and jumps with emission appear only when $b_5 \neq 0$, regardless of the signs of the coefficients (if the amplitude of the initial discontinuity is sufficiently large). For $b_3 = 0$ and $b_5 \neq 0$, only solutions describing jumps with emission can be obtained. For $b_2 b_3 > 0$ and for a small amplitude of the initial discontinuity, the solutions describe jumps with an unsteady structure.

With the cold-plasma model adopted here, we can employ asymptotic methods to derive the conventional KdV equation for the entire parameter range under consideration and the generalized KdV equation with $b_3 = 0$ at $\theta = \theta_c$ [1]. Qualitatively, the shape of the dispersion curve of the magnetosonic branch for $\theta < \theta_c$ coincides with that obtained from equation (3) at $b_1 b_2 > 0$ (in the region $k > 0$, the dispersion curve has an inflection point) and, for $\theta > \theta_c$, it coincides with that obtained at $b_1 b_2 < 0$ (the dispersion curve has no inflection point). As will be shown in Section 5, the type of jump structure is governed by the shape of the dispersion curve; consequently, we can expect that the full model can also yield solitonlike jumps and jumps with emission. In Section 5, we describe the method used to predict whether the solutions with these jumps might exist in the general case. A factor such as the presence of an

inflection point on the dispersion curve in the region $k > 0$ plays an important role in this method, which was originally tested with jumps in the case of waves whose envelope is described by the nonlinear third-order Schrödinger equation [7]:

$$A_t + ib_2A_{xx} + b_3A_{xxx} + i|A|^2A = 0. \quad (4)$$

The dispersion curve for the hydrodynamic version of this equation [8] consists of two branches, one of which has an inflection point and the other has no inflection point.

Plasma-related computation results can be analyzed based on the results obtained from equations (3) and (4), because they allow for a much faster numerical solution of the problem, thereby making it possible to carry out simulations over longer time intervals. Qualitatively, the solutions obtained from all three of the models are similar in shape.

3. NUMERICAL METHOD

In order for the desired numerical solutions to possess conservative properties used to examine the time-independent solutions (see Section 5), it is necessary to use conservative numerical schemes. The previous analysis [4, 9], which was carried out on the basis of nonconservative schemes, yielded conventional jumps without emission instead of solitary waves, which contradicts the theory. We convert the basic equations into the form

$$\frac{\partial n}{\partial t} + \frac{\partial nu}{\partial x} = 0,$$

$$\frac{\partial nu}{\partial t} + \frac{\partial}{\partial x}\left(nu^2 + \frac{B_y^2 + B_z^2}{2}\right) = 0,$$

$$\frac{\partial nv}{\partial t} + \frac{\partial}{\partial x}\left(-R_e^{-1}R_i^{-1}\frac{\partial^2 v}{\partial x\partial t} + nuv - B_xB_y + R_e^{-1}\left(B_x\frac{\partial w}{\partial x} - B_z\frac{\partial u}{\partial x} - R_i^{-1}\left(\frac{\partial u}{\partial x}\frac{\partial v}{\partial x} + u\frac{\partial^2 v}{\partial x^2}\right)\right)\right) = 0,$$

$$\frac{\partial nw}{\partial t} + \frac{\partial}{\partial x}\left(-R_e^{-1}R_i^{-1}\frac{\partial^2 w}{\partial x\partial t} + nuw - B_xB_z - R_e^{-1}\left(B_x\frac{\partial v}{\partial x} - B_y\frac{\partial u}{\partial x} + R_i^{-1}\left(\frac{\partial u}{\partial x}\frac{\partial w}{\partial x} + u\frac{\partial^2 w}{\partial x^2}\right)\right)\right) = 0, \quad (5)$$

$$\frac{\partial B_y}{\partial t} + \frac{\partial}{\partial x}\left(-R_e^{-1}R_i^{-1}n^{-1}\frac{\partial^2 B_y}{\partial x\partial t} + B_yu - B_xv - R_i^{-1}n^{-1}\left(B_x\frac{\partial B_z}{\partial x} + R_e^{-1}\left(u\frac{\partial^2 B_y}{\partial x^2} + \frac{\partial u}{\partial x}\frac{\partial B_y}{\partial x}\right)\right)\right) = 0,$$

$$\frac{\partial B_z}{\partial t} + \frac{\partial}{\partial x}\left(-R_e^{-1}R_i^{-1}n^{-1}\frac{\partial^2 B_z}{\partial x\partial t} + B_zu - B_xw + R_i^{-1}n^{-1}\left(B_x\frac{\partial B_y}{\partial x} - R_e^{-1}\left(u\frac{\partial^2 B_z}{\partial x^2} + \frac{\partial u}{\partial x}\frac{\partial B_z}{\partial x}\right)\right)\right) = 0.$$

Equations (5) were solved numerically with the help of a three-layer staggered scheme with second-order accuracy in time. We denote the numbers of the time layers by the superscripts and the numbers of the mesh points in space by subscripts. Equations (5) are regularized: each of them contains the time derivative of only one quantity, except for the quantity n, which is found explicitly. The regularization allows us to solve four implicit difference equations for nv, nw, B_y, and B_z independently.

The results obtained were tested against the results of computations based on a two-layer scheme with first-order accuracy in time. The results from two- and three-layer schemes were found to differ insignificantly because of a short time step. Unlike the three-layer scheme, the two-layer scheme is applicable to the basic equations with dissipative terms.

The first-order derivatives can obviously be approximated by

$$f_x \longrightarrow (f_{i+1} - f_{i-1})/2\Delta x,$$
$$f_t \longrightarrow (f^{m+1} - f^{m-1})/2\Delta t.$$

In order for the desired numerical solutions to possess symmetry properties used in the theory presented in Section 5, the derivatives with respect to x should be approximated using centered difference schemes. We present the prescriptions for approximating even and odd higher order conservative derivatives:

$$(gf_x)_x \longrightarrow ((g_{i+1} + g_i)(f_{i+1} - f_i) - (g_i + g_{i-1})(f_i - f_{i-1}))/2\Delta x^2,$$
$$(gf_xh_x)_x \longrightarrow ((g_{i+1} + g_i)(f_{i+1} - f_i)(h_{i+1} - h_i) - (g_i + g_{i-1})(f_i - f_{i-1})(h_i - h_{i-1}))/2\Delta x^3,$$
$$(gf_{xt})_x \longrightarrow (((g_{i+1}^m + g_i^m)(f_{i+1}^{m+1} - f_i^{m+1}) - (g_i^m + g_{i-1}^m)(f_i^{m+1} - f_{i-1}^{m+1}))/2\Delta x^2 - ((g_{i+1}^m + g_i^m)(f_{i+1}^{m-1} - f_i^{m-1}) - (g_i^m + g_{i-1}^m)(f_i^{m-1} - f_{i-1}^{m-1}))/2\Delta x^2)/2\Delta t,$$
$$(gf_{xx})_x \longrightarrow (g_{i+1}(f_{i+2} + f_i - 2f_{i+1}) - g_{i-1}(f_{i-2} + f_i - 2f_{i-1}))/2\Delta x^3,$$

where f, g, and h are arbitrary unknowns. These complicated prescriptions are aimed at reducing the error variance in using the calculation scheme and at ensuring stability. The time step Δt was chosen to be on the order of $\sim\Delta x^3$, because four of the total six equations for the system modeled here are similar to the KdV equations.

The implicit discrete equations were solved iteratively:

$$f^{m+1,j+1} = f^{m+1,j} + c_f F_f(f^{m+1,j}, f^{m-1}, n^m, u^m, v^m, w^m, B_y^m, B_z^m),$$

$$f^{m+1,0} = f^{m-1},\ f \longrightarrow nv, nw, B_y, B_z,$$

where F_f is the finite-difference approximation of the corresponding equation and j is the number of the iteration step. We stopped the iteration procedure when $|f^{m+1,j+1} - f^{m+1,j}| \le \epsilon$, where ϵ is the desired accuracy of the calculations. The appropriate values of c_f were chosen based on the results of numerical calculations: large values of this quantity cause the iteration procedure to diverge; for small c_f values, the iteration procedure is slowly converging.

The problems of the formation of a solitary wave at $\theta > \theta_c$ and the decay of a solitary wave at $\theta < \theta_c$ [4, 9] were used as test problems. Test simulations revealed that our calculation scheme is very effective. Since the scheme conserves the symmetry and conservative properties of the basic model, a constant-amplitude solitary wave forms on the mesh in the course of calculations (clearly, when the model admits solutions of the solitary wave type). A similar approach was successfully applied to waves described by a third-order Schrödinger equation [5, 8] and by a fifth-order KdV equation [10].

The physical constants used in our study correspond to a hydrogen plasma, $R_e^{-1} = 0.023$.

4. NUMERICAL RESULTS

The input parameters were chosen to be similar to the parameters of solitary waves [9]; the only difference was that $\cosh^{-2}$ was replaced by tanh and the antisymmetric unknowns w and B_z (see Section 5) were set to zero:

$$B_y = \sin\theta + a_0,\quad a_0 = \mu\tanh[(x - x_0)/L],$$
$$u = (B_y^2 - \sin^2\theta)/(2V),\quad n^{-1} = 1 - u/V, \qquad (6)$$
$$V = 1 + \mu.$$

In the examples presented below, the small parameter μ is equal to $\mu = -0.05$. The value of L is unimportant, because we are interested in a self-similar solution for long times. The frame of reference in which the calculations were carried out moved at a relative speed equal to unity (i.e., at the speed of long-wavelength magnetosonic waves in an unperturbed state).

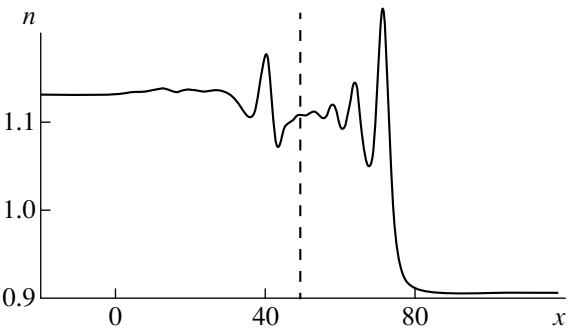

Fig. 2. Illustration of the method for singling out a magnetosonic jump.

Our simulations showed that, after a certain time, the initial discontinuity decays into two FMS waves, two Alfvén waves, and an SMS wave (see Fig. 2, $t = 40$, $x_0 = 75$). In the rest frame, in the unperturbed state, the Alfvén velocities of long-wavelength waves are equal to $\pm\cos\theta$ and the velocity of SMS waves equals zero. Since $\theta = 1.555 \approx \pi/2$ in the example in Fig. 2, all these velocities either vanish or are close to zero, thereby making it impossible to single out the Alfvén wave.

From this point on, we can regard the parameters of a decaying FMS wave in the corresponding part of the calculation region as the initial parameters for the new problem of the decay of an initial magnetosonic discontinuity. In Fig. 2, the vertical dashed line denotes the x value at which the calculation region is cut in order to single out the magnetosonic discontinuity. We supplemented our numerical code with subprograms that provide the possibility for arbitrarily enlarging or reducing (if necessary) the calculation region. For a reduced calculation region, the input parameter values required to specify the boundary conditions were replaced by the instantaneous parameter values at the cut. In the new part of the enlarged calculation region, the values of all of the parameters were set equal to their values at the corresponding boundary.

Note that, in the model described above, an SMS wave is degenerate and experiences no dispersion. Unlike the scheme used in [4], our scheme simulates a fictitious phenomenon—the onset and growth of short-wavelength waves—because of the numerical errors in the course of calculations, even if the computations are carried out for an artificially singled out FMS wave. However, our scheme is free of this drawback when applied to the set of equations for a plasma with hot electrons, in which case we also examined magnetosonic jumps. Introducing the term $b^2 n_x$ (where b is the speed of an SMS wave for $\theta = 0$) into the second equation in (1) allows us to eliminate this drawback even for low b values, thereby correcting for the scheme on the basis of physical considerations. An effective mathematical way of correcting our model is to supplement the first equation in (1) with the coefficient d in front of the term $(un)_x$ such that $d \longrightarrow 1$ as $\Delta x \longrightarrow 0$. Since our

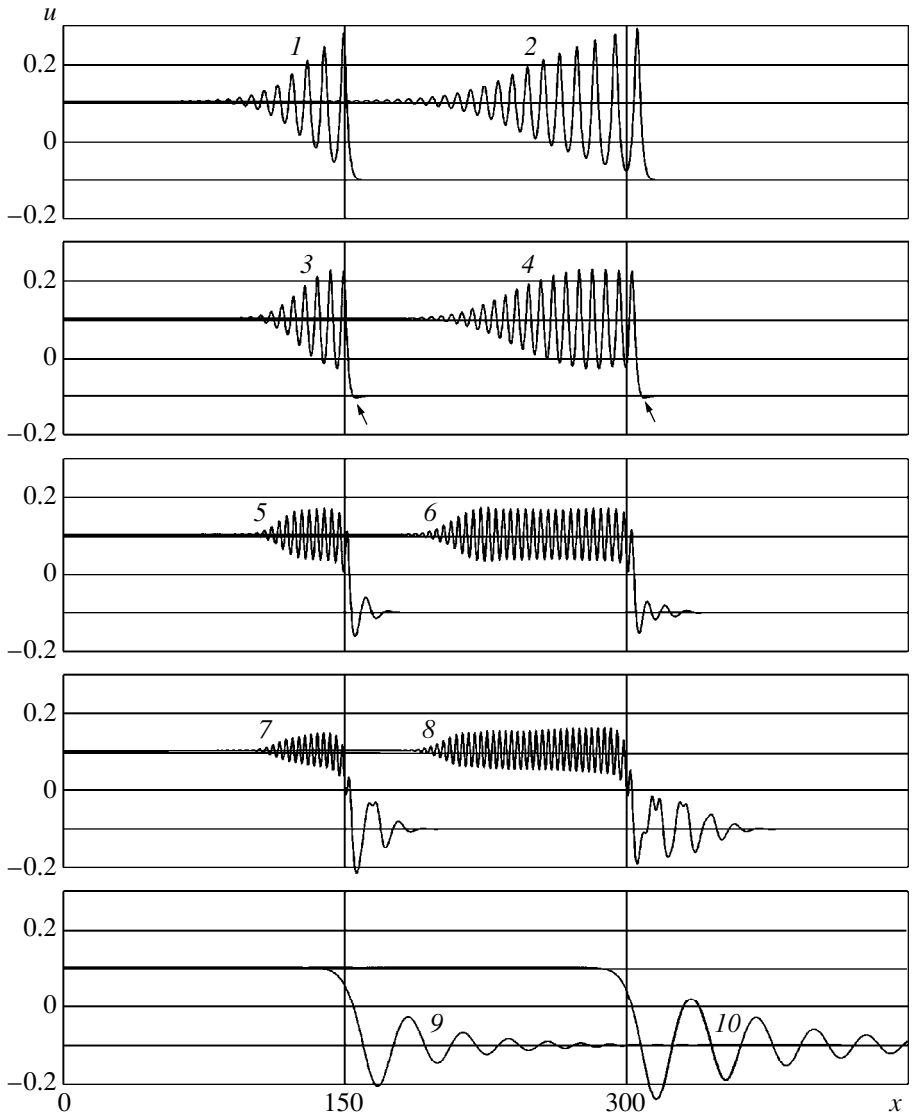

Fig. 3. Representative plots of symmetric quantities (e.g., u) for different values of θ at different times.

computations are quasisteady in character, such a correction has essentially no impact on the jumps in simulating magnetosonic waves.

Our numerical analysis is aimed at clarifying how the parameter θ affects the type of jump. Figures 3 and 4 show representative plots of u and B_z for the same amplitude of the initial discontinuity and for the following values of θ close to θ_c (from top to bottom): $\theta = 1.555 > \theta_c$, $\theta = 1.547 \approx \theta_c$, $\theta = 1.535 < \theta_c$, $\theta = 1.530 < \theta_c$, and $\theta = 1.500$ (which is significantly smaller than θ_c). The curves marked by odd numbers are plotted at the time $t = 150$, and the curves marked by even numbers are plotted at $t = 300$. The plots were obtained for $x_0 = 0$ in the rest frame. The plots for the remaining symmetric and antisymmetric unknowns (see Section 5) are similar in shape to those in Figs. 3 and 4.

Based on the theory presented in Section 5, we can expect that, for $\theta = 1.555$ (curves *1* and *2*), a solitonlike jump will arise in the course of simulation. For $\theta = 1.547$ (curves *3* and *4*) and $\theta = 1.535$ (curves *5* and *6*), a jump with emission forms. In the first case, the amplitude of the emitted wave is large enough for the solution to differ insignificantly from that describing a solitonlike jump. A spatially damped oscillation marked by an arrow to the right of the jump in Figs. 3 and 4 provides evidence that the k values for the related homogeneous state behind the jump are complex (see Section 5). In the second case, the amplitude of the emitted wave is smaller: a sequence of several spatially damped oscillations is seen to the right of the jump. Since the solution describing these damped oscillations with a sufficiently large amplitude exists for θ values near the point of transition to jumps with an unsteady structure, the sim-

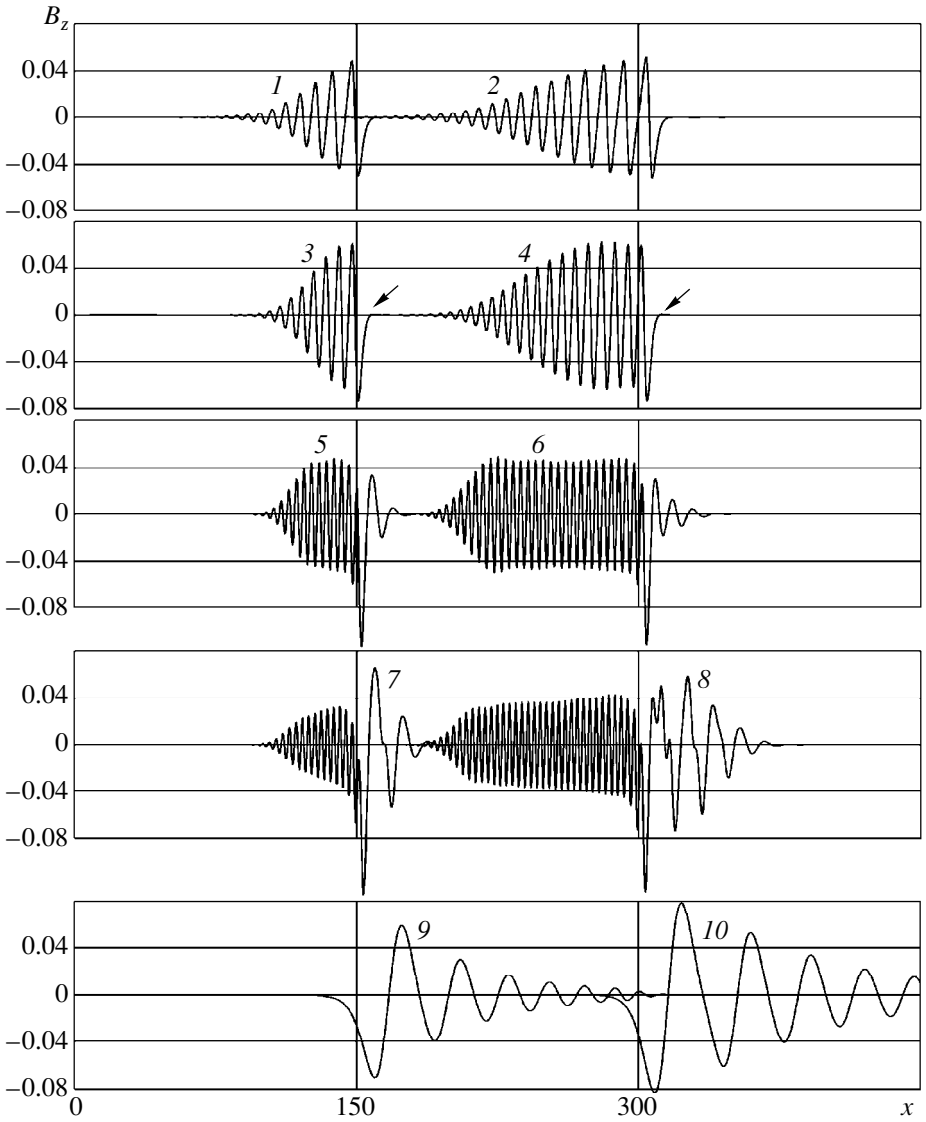

Fig. 4. Representative plots of antisymmetric quantities (e.g., B_z) for different values of θ at different times.

ulation of the process of establishing a steady regime takes a long time. For θ = 1.530 (curves *7* and *8*), the solution is seen to describe a jump with an unsteady structure and two waves in the expanding wave zone to the right of the jump. Note that, for θ = 1.5, which is sufficiently smaller than θ_c (curves *9* and *10*), solitonlike jumps are theoretically impossible, in which case, however, the effect of high-order dispersion is insignificant, so that we can actually regard the jump illustrated by curves *9* and *10* as a solitonlike jump, because the amplitude of short-wavelength waves emitted to the left is negligibly small. For even smaller values of θ in comparison with the critical value θ_c, the amplitude of the waves emitted in the case of small-amplitude jumps should presumably decrease according to an exponential law, as in the problem of emission of a small-amplitude solitary wave [9, 10].

5. PREDICTION OF THE POSSIBLE TYPES OF JUMPS

Now, we describe how to predict the possible types of time-independent solutions characterizing the structure of jumps [5, 7]. We will consider only those types of solutions that are related to the model under study. We are especially interested in the problem of the jump structure. My paper [5] was, in particular, aimed at justifying the evolutional character of the jumps; i.e., I proved that all of the desired boundary conditions at the jumps can be obtained by solving the problem of the jump structure. The evolutional character of the jumps implies that they are stable; consequently, they may be observed in numerical and physical experiments.

Let the model be based on a conservative set of symmetric equations that are reversible in time. Integrating these equations once yields the set of time-dependent

equations whose solutions describe steady jumps. Introducing additional unknowns, we can represent this set of time-dependent ordinary differential equations as a set of equations $u_{qx} = F_q(\mathbf{u})$, which are invariant under the transformation ($x \longrightarrow -x$, $u_q \longrightarrow u_q$) for $q = 1, \ldots, 2n - 1$ (symmetric unknowns) and under the transformation $u_q \longrightarrow -u_q$ for $q = 2, \ldots, 2n$ (antisymmetric unknowns). This procedure (which can be applied to any physically meaningful set of equations that are reversible in time) is used to prove the existence of solitary and generalized solitary waves with the help of the central manifold method [2–4, 10]. Here, we are dealing with a set of unknowns (v, w, B_y, B_z); the unknowns n and u are eliminated, because the first two equations contain only first-order derivatives. The set of unknowns for equation (3) is $\{q_i\} = a, a_x, a_{xx}, a_{xxx}$.

The existence assertions, which will be given below, are all valid for sets of equations of arbitrary order. The numerical errors introduced by the calculation scheme are equivalent to incorporating higher order derivatives with respect to x into the basic equations. Consequently, these assertions also justify the fact that our numerical and analytic method for revealing different types of jump structures is insensitive to the approximation errors.

The geometric approach presented here is based on the fact that, if the summarized dimensionality of two subspaces of a space coincides with the dimensionality of the space itself, then, in the standard case, the subspaces can have either one point of intersection, a finite number of these points, or a denumerable set of them. Additionally, if the vector tangent to both of the subspaces exists at the point of their intersection and if their summarized dimensionality exceeds the dimensionality of the space by unity, then, in the standard case, the subspaces may have a line of intersection. This situation takes place if both subspaces are composed of certain sets of the phase trajectories of a dynamic system. We will call such subspaces the phase subspaces. We consider two subspaces composed of the phase trajectories $\{\mathbf{u}(x), -\infty < x < +\infty\}$ that pass through the ϵ-vicinity of the point C at $x = x_0$ and are either bounded or periodic at $+\infty$. We denote these subspaces by $S(C, \epsilon; |\mathbf{u}| < M, x \longrightarrow +\infty)$ and $S(C, \epsilon; \mathbf{u}(x + T) \longrightarrow \mathbf{u}(x), x \longrightarrow +\infty)$, respectively. The value of x_0 is unimportant here, because the solution is defined to within the phase shift.

We linearize the basic equations about the homogeneous states on both sides of the jump. We consider the related dispersion curves $\omega = \omega(k)$ (the dispersion relation is obtained through the substitution $\sim\exp[i(kx - \omega t)]$) and the equations for the wavelengths of the time-independent solutions, $R(U, k) = 0$, where U is the jump speed. The equation $R(U, k) = 0$ has $2n$ roots; moreover, we have $k_{2r} = -k_{2r-1}$ ($r = 1, \ldots, n$). The solution to the set of time-dependent linearized equations depends on $2n$ parameters c_j and is represented as $\mathrm{Re}(\sum_{j=1}^{2n} c_j \exp ik_j x)$. The waves growing as $x \longrightarrow +\infty$ refer to $\mathrm{Im}(k_j) < 0$, the waves growing as $x \longrightarrow -\infty$ are related to $\mathrm{Im}(k_j) > 0$, and purely periodic waves correspond to real values of k_j. Below, we will assume that nonlinear versions of the sets of equations under discussion possess the same qualitative features; the only difference is that the waves may be growing only in the vicinity of the equilibrium point, whereas, far from the equilibrium point, their amplitudes may remain finite.

Let a jump propagate at a speed U, which corresponds to the straight line $U = \omega/k$ on the (ω, k) plane. In analyzing the possible types of jumps, it is important to know the number of its intersections with the dispersion curve. Below, in counting the number of intersections, we will neglect the intersection at the origin of the coordinates, corresponding to $k = 0$, which is already accounted for as a constant of integration of the basic equations. Also, the symmetry of the dispersion curve allows us to count only the intersections for $k > 0$. At each intersection, the equation $R(U, k) = 0$ has two real roots with opposite signs. Since the parts of the dispersion curve are different on both sides of the jump, the number of intersections to the left of the jump can differ from that to the right of the jump.

Let the straight line not intersect the dispersion curve, in which case no real roots correspond to the equilibrium point C_1 under consideration: there are only n roots with $\mathrm{Im}(k) < 0$ (the waves that are growing as x increases) and n roots with $\mathrm{Im}(k) > 0$ (damped waves). We consider the subspaces $S_1 = S(C_1, \epsilon; \mathbf{u} \longrightarrow C_1, x \longrightarrow -\infty)$ and $S_2 = \{\mathbf{u}, u_{2i} = 0\}$, each having dimensionality n. Since the summarized dimensionality of these subspace is equal to $2n$, they generally have either one point of intersection, a finite number of these points, or a denumerable set of them. By virtue of the symmetry of the basic equations, each intersection corresponds to a solitary wave, and the point of intersection corresponds to the hump of a solitary wave. In our model, a solitary wave can be used to characterize the jump structure only for $\theta > \theta_c$. In this case, the dispersion branch has no inflection points at $k > 0$, and, when the jump speed is slightly above the magnetosonic speed, there is no intersection and the roots are purely imaginary. If the straight line does not intersect the dispersion branch for $\theta < \theta_c$, then the roots are complex and a so-called 1 : 1 soliton is possible [10]. However, since the related solution has many humps, it cannot be used to characterize the structure of the jump at hand.

Let us consider two equilibrium points such that the straight line $\omega = kU$ does not intersect the dispersion curve for one of them (C_1) and intersects the curve only once for the other (C_2). The number of growing waves at the equilibrium point C_1 is n, and their number at the point C_2 is $n - 1$. The subspaces $S_1 = S(C_1, \epsilon_1; \mathbf{u} \longrightarrow C_1, x \longrightarrow -\infty)$ and $S_2 = S(C_2, \epsilon_2; \mathbf{u}(x + T) \longrightarrow \mathbf{u}(x), x \longrightarrow +\infty)$ are phase subspaces of dimensionalities n and $n + 1$, respectively; their summarized dimensionality is

$2n + 1$. In this case, they generally have either one line of intersection, a finite number of these lines, or a denumerable set of them. A jump with emission corresponds to a line of intersection. In our model, such a jump is possible for both ranges $\theta < \theta_c$ and $\theta > \theta_c$.

Numerical solutions to the problem of the decay of the initial discontinuity described by the generalized KdV equation and the Schrödinger equation show that, in fourth-order dynamic systems, a jump with emission can occur only when all of the k values are complex at the point C_1. This can, in principle, be explained by looking at the phase diagrams of a fifth-order KdV equation in the cross section (a, a_x) of phase space such that $a_{xx} = 0$ and $a_{xxx} = 0$ at $x = 0$. In the case of complex k values, the phase trajectories that originate from the point C_1 are spiral in character and loop a region around this point. In the case of imaginary k values, generalized separatrices appear on the phase diagram and the point C_2 is seen as if it occurs in isolation. Since phase trajectories cannot cover this isolated region, no solution describing a jump with emission can exist. Our numerical experiments showed that, in the case of a jump accompanied by the emission of a wave, the roots are also complex for a plasma (the presence of damped oscillations on one of the sides of the jump; see curves *3–6* in Figs. 3, 4).

We can similarly show that, in the general case, there are no solitary waves in the presence of a point of intersection, in which case, however, a solitary wave with a superimposed periodic wave can exist. In general dissipation-free models, a jump without wave zones (an analog of a shock wave in gas dynamics) is also absent. However, models with a more pronounced nonlinearity show that, in the absence of intersections, a discontinuity (at which it is necessary to specify an additional boundary condition) may also occur between homogeneous states on each side of the jump; this discontinuity (kink) is an analog of a combustion shock [7, 9], which goes beyond the scope of our model.

Our approach is also inapplicable to jumps with a steady structure accompanied by the emission of two or more waves. Such jumps should be analyzed with the help of sixth-order (and higher) dynamic models. That is why the jump structure obtained from our model for $\theta = 1.530$ is unsteady.

ACKNOWLEDGMENTS

I am grateful to A.G. Kulikovskiĭ for valuable remarks and to A.A. Barmin for fruitful discussions. This work was supported in part by the Russian Foundation for Basic Research (project no. 96-01-00991) and INTAS (grant no. 435-i-96).

REFERENCES

1. T. Kakutani and H. Ono, J. Phys. Soc. Jpn. **26**, 1305 (1969).
2. A. T. Il'ichev, Mat. Zametki **59**, 719 (1996).
3. A. Il'ichev, J. Plasma Phys. **55**, 181 (1996).
4. I. Bakholdin and A. Il'ichev, J. Plasma Phys. **60**, 569 (1998).
5. I. B. Bakholdin, Prikl. Mat. Mekh. **63**, 52 (1999).
6. A. V. Gurevich and L. P. Pitaevskiĭ, Zh. Éksp. Teor. Fiz. **65**, 590 (1973) [Sov. Phys. JETP **38**, 291 (1974)].
7. I. B. Bakholdin, Zh. Vychisl. Mat. Mat. Fiz. **38**, 1329 (1998).
8. I. B. Bakholdin, Izv. Akad. Nauk, Mekh. Zhidk. Gaza, No. 4, 111 (1994).
9. I. B. Bakholdin, Preprint No. 61, IPM RAN (Keldysh Inst. of Applied Mathematics, Russian Academy of Sciences) (1997).
10. I. Bakholdin and A. Il'ichev, Contemp. Math. **200**, 1 (1996).

Translated by G. V. Shepekina

Plasma Physics Reports, Vol. 26, No. 1, 2000, pp. 70–77. Translated from Fizika Plazmy, Vol. 26, No. 1, 2000, pp. 73–80.

BEAMS IN PLASMA

Numerical Model of a Plasma with a Monoenergetic Relativistic Electron Beam

Yu. A. Volkov and V. B. Krasovitskiĭ

Keldysh Institute of Applied Mathematics, Russian Academy of Sciences, Miusskaya pl. 4, Moscow, 125047 Russia

Received April 20, 1998

Abstract—The possibility of converting the energy of a low-density relativistic electron beam into the energy of a narrow Langmuir wave packet is demonstrated by numerical integration of the Vlasov and Poisson equations. It is shown that a small perturbation stops growing exponentially because the beam electrons are trapped by the wave, so that the wave-field energy is partially converted back into beam energy. Then, the beam slips out of resonance with the wave, and the energy exchange with the wave terminates almost completely. A detailed comparison is made between the results obtained in a one-dimensional (hydrodynamic) model of the beam instability with allowance for the plasma nonlinearity and the results of numerical simulations. The computed time evolution of the field energy is found to deviate substantially from the theoretical evolution, which is attributed to the decay of the primary oscillation spectrum in the numerical model. However, even with allowance for the internal kinetic processes in the plasma, the single-mode and numerical models give nearly the same energy losses of the beam in the asymptotic limit $t > 10^3 \omega_p^{-1}$ (where ω_p is the plasma frequency). © *2000 MAIK "Nauka/Interperiodica".*

1. INTRODUCTION

It is well known [1, 2] that, as the mass of the electrons in a low-density ($\nu = n_b/n_p \ll 1$) beam increases due to relativistic effects, the growth rate of the Langmuir oscillations decreases, $\delta \simeq \nu^{1/3}\omega_p/\gamma_0$, and their energy grows, $\langle E^2\rangle/4\pi \simeq \alpha n_b m v_0^2 \gamma_0$, in the narrow range $\Delta k/k_0 \simeq \nu^{1/3}/\gamma_0$ of the wavenumber spectrum (where $k_0 = \omega_p/v_0$, n_b and v_0 are the density and velocity of the beam, γ_0 is the relativistic factor, n_p is the plasma density, ω_p is the plasma frequency, and $\alpha = \gamma_0\nu^{1/3}$).

In the range of high energies ($\alpha \simeq 1$), the electrons are observed to accumulate in the accelerating phases of the wave. Although the effective mass of these electrons increases, their velocity remains close to the speed of light, and their positions inside the wave change only slightly. Consequently, a fraction of the energy of decelerated electrons is converted into the energy of accelerated electrons through the wave field, thereby reducing the efficiency for conversion of the beam energy into the energy of Langmuir waves [3–9].

In the range $\alpha > 1$, it is necessary to take into account not only the trapping of beam electrons by the wave but also a nonlinear decrease in the wave phase velocity, because strong electric fields change the waveguide properties of the plasma during the instability [11–17]. In the hydrodynamic approach, the dependence of the dielectric function on the field amplitude is governed either by the high-frequency pressure gradient during the steady injection of a beam into a plasma [11, 12] or by the change in the electron velocity in the wave field in the case of a homogeneous plasma [13–17].

The plasma heating that cannot be described in the hydrodynamic approach because of the asynchronous nature of electron oscillations was taken into account in numerical experiments [4, 5]. Particle-in-cell simulations of the plasma and beam showed that the nonlinear relaxation of a monoenergetic relativistic electron beam (REB) in a dense plasma occurs in three stages. In the first stage, the exponential growth of a small perturbation with the highest hydrodynamic rate results in the trapping of resonant electrons by the wave and in the saturation of an unstable mode at the first maximum of the field amplitude. The nonlinear phase oscillations of the trapped-electron bunches that arise in the second stage are accompanied by oscillations of the field amplitude and the onset of an oscillatory (modulational) instability, during which the short-wavelength perturbations ($k\lambda_d \le 1$, where λ_d is the Debye length) are damped via Landau damping and the wave field energy is converted into the energy of plasma electrons (ions). In the final stage of the instability, energy exchange between the beam and the plasma is almost completely absent.

We solve the Vlasov–Poisson set of equations in order to reproduce the results of numerical experiments [4, 5] and to compare them with the results obtained in the single-mode model [16], which takes into account the plasma nonlinearity in the hydrodynamic approach.

1063-780X/00/2601-0070$20.00 © 2000 MAIK "Nauka/Interperiodica"

Our calculations show that the numerical and theoretical time evolutions of the field energy coincide in the initial stage (when the field energy is growing exponentially) but differ substantially in the stage in which the primary spectrum decays. However, in the asymptotic limit $t > 10^3\omega_p^{-1}$, the energy losses of the beam in the kinetic and hydrodynamic models are found to be nearly the same.

2. SINGLE-MODE MODEL

In the single-mode model of the instability of a plasma with a low-density electron beam, all of the beam and plasma electrons interact with a narrow Langmuir wave packet:

$$E = \mathrm{Re}[E(t, x)\exp(ik_0x - \omega_0 t)]. \quad (1)$$

The interaction of an REB with a plasma is described by a nonlinear parabolic equation for the field amplitude $E(t, x)$, and the set of equations for the motion of the beam electrons [16]

$$\frac{v_g'}{2}\frac{\partial^2 E}{\partial x^2} + i\left(\frac{\partial}{\partial t} + v_g\frac{\partial}{\partial x}\right)E + \frac{\omega_p}{2}\left(\varepsilon + \frac{|E|^2}{E_{NL}^2}\right)E = -i\frac{4\pi e n_b v_0}{S}\sum_{s=1}^{S}\exp(-i\psi_s), \quad (2)$$

$$\frac{d^2\psi_s}{dt^2} = \frac{ek_0}{m\gamma_s^3}\mathrm{Re}[E(t, x_s)\exp(i\psi_s)],$$

where $\psi_s = k_0x_s(t) - \omega_0 t$, $x_s(t)$ is the coordinate of the sth beam electron, S is the number of beam electrons per wavelength $\lambda = 2\pi/k_0$, $\gamma_s = (1 - \dot{x}_s^2/c^2)^{-1/2}$,

$$\varepsilon = 1 - \omega_L^2/\omega_0^2, \quad \omega_L^2 = \omega_p^2 + (k_0v_T)^2,$$

$$v_g = k_0v_T^2/\omega_0, \quad v_g' = dv_g/dk_0,$$

$$v_T = (T/m)^{1/2}, \quad \omega_0 = k_0v_0,$$

and T is the plasma electron temperature.

In a homogeneous cold plasma, the nonlinear correction to the plasma frequency arises due to the change in the electron velocity in the wave electric field $E_{NL} = E_p$ (where $E_p^2 = (32\pi/3)n_pmc^2$) [16, 19], whereas, in an inhomogeneous heated plasma, the high-frequency pressure gradient is balanced by the kinetic pressure gradient and the static electric field when $E_{NL} = E_T$ (where $E_T^2 = 32\pi n_pT$) [18].

For a cold plasma ($T = 0$), equations (2) are ordinary differential equations with respect to time. In order to pass over to the limiting case of a linear beam dynamics, we expand the argument of the exponential function in small perturbations of the electron trajectories: $\psi_s = \psi_{s0} + \tilde{\psi}_s$, where $|\tilde{\psi}_s| \ll \psi_{s0}$. If $S \gg 1$ and the electrons are distributed uniformly over the spatial period of the wave ($\psi_{s0} = 2\pi s/S$), then equations (2) reduce to the hydrodynamic equations [16]

$$\frac{dE}{dt} - i\frac{\omega_p}{2}\left(\varepsilon + \frac{|E|^2}{E_p^2}\right)E = i4\pi e v_0\rho,$$

$$\frac{d^2\rho}{dt^2} = \frac{ek_0}{2m\gamma_0^3}E, \quad \rho = \frac{n_b}{S}\sum_{s=1}^{S}\tilde{\psi}_s\exp(-i\psi_{s0}), \quad (3)$$

where ρ is the depth of modulation of the beam density and $\gamma_0 = (1 - \beta_0^2)^{-1/2}$.

According to (3), the growth rate of the small perturbations is

$$\delta = \sqrt{3}(\nu/16)^{1/3}\omega_p/\gamma_0, \quad \omega_0 = \omega_p(1 - \delta/\sqrt{3}). \quad (4)$$

In the nonlinear stage, the trapping of the beam electrons by the wave causes the perturbation amplitude to saturate when

$$\rho/n_b \simeq ek_0E_m/m\gamma_0^3\delta^2 \simeq 1, \quad E_m^2 \simeq \alpha 8\pi n_bmv_0^2\gamma_0, \quad (5)$$

where $\alpha = \gamma_0\nu^{1/3} \ll 1$ [1, 2]. In the high-energy range, the first formula in (5) gives $\rho/n_b = \Omega_{ph}^2/\delta^2 \simeq \alpha^{-1/2}$ when the field amplitude reaches its maximum value $E_m \simeq (8\pi n_bmv_0^2\gamma_0)^{1/2}$. Consequently, for $\alpha^{1/2} \gg 1$, the beam motion satisfies linearized equations and the instability is suppressed by the plasma nonlinearity. In this energy range, passing over to dimensionless variables in the nonlinear equations (3) yields $E_m \sim \alpha^{-1}$.

The dotted curves in Figs. 1 and 2 illustrate numerical solutions to equations (2) obtained with 50 particles per wavelength for a cold plasma and a monoenergetic beam.

3. NUMERICAL EXPERIMENT

The set of equations for a plasma with an REB in a self-consistent field includes Poisson's equation and the Vlasov equations for the distribution functions f_α of the plasma and beam electrons

$$\frac{\partial E}{\partial x} = 4\pi\sum_\alpha e_\alpha\int f_\alpha dp,$$

$$\frac{\partial f_\alpha}{\partial t} + v\frac{\partial f_\alpha}{\partial x} + e_\alpha E\frac{\partial f_\alpha}{\partial p} = 0, \quad (6)$$

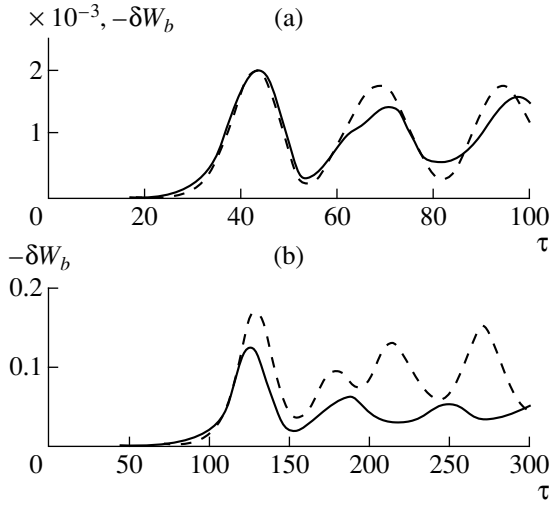

Fig. 1. Comparison between the results obtained in the kinetic (solid curves) and hydrodynamic (dashed curves) plasma models for a beam with the energy γ_0 = (a) 1.005 and (b) 3.

with summation over the electron species. Under the periodic boundary conditions, the energy integral is

$$\left\langle \frac{E^2}{8\pi} + \sum_{\alpha} \int mc^2 \gamma (f_\alpha - f_\alpha^{(0)}) dp \right\rangle = 0, \qquad (7)$$

where the angular brackets denote averaging over the perturbation wavelength $\lambda = 2\pi/k_0$, $f_{\alpha 0}$ is the initial distribution function of electrons of species α, and $\gamma = (1 + p^2/m^2c^2)^{1/2}$.

At the initial time $t = 0$, the electrons of a monoenergetic beam and the plasma electrons and ions are assumed to be distributed uniformly in space:

$$f_b^{(0)} = \sigma e \sum_{s=1}^{N_b} \delta(x - x_{bs}) \delta(p - p_0),$$
$$f_{e,i}^{(0)} = \pm \sigma e \sum_{s=1}^{N_{e,i}} \delta(x - x_{ps}) \delta(p), \qquad (8)$$

where $x_{\alpha s} = 2\pi s/N_\alpha k_0$, N_α is the number of particles of species α (the number of charged planes) per wavelength, σe is the surface electron density, and p_0 is the initial momentum of the beam electrons. The number of plasma ions, which are assumed to be immobile, is determined by the charge neutrality condition for the beam–plasma system, $N_i = N_e + N_b$.

The distribution functions

$$f_\alpha = \sigma \sum_s e_\alpha \delta[x - x_{\alpha s}(t)] \delta[p - p_{\alpha s}(t)] \qquad (9)$$

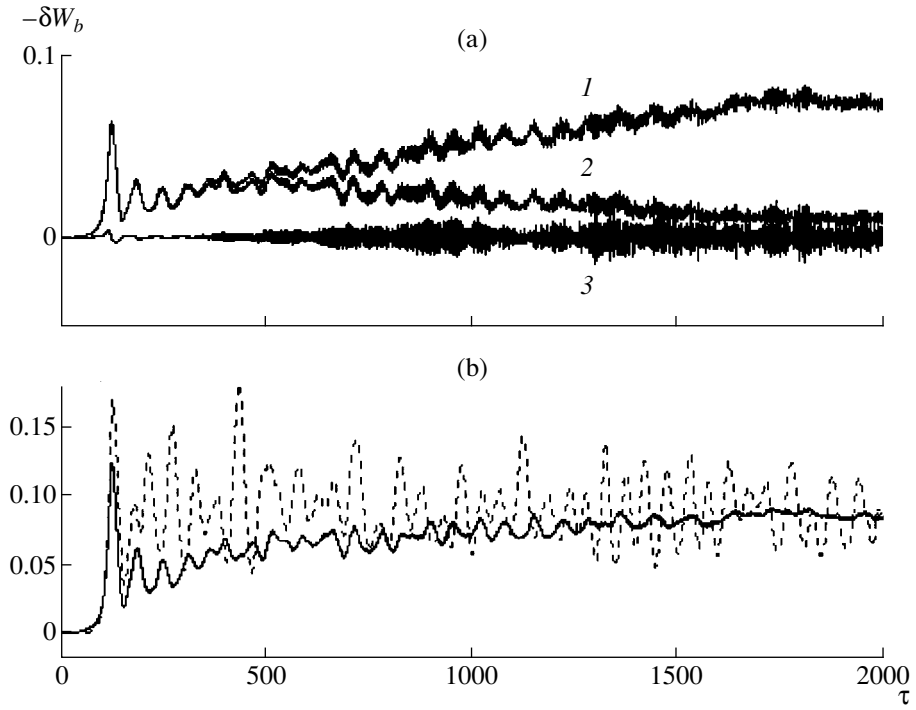

Fig. 2. Transition of the beam–plasma system to a quasisteady regime for $\gamma_0 = 3$: (a) the time evolutions of (*1*) the plasma energy W_p, (*2*) the field energy W_f, and (*3*) the power $\dot{W}_p$ and (b) the time evolutions of the energy $-\delta W_b$ lost by the beam. The solid curves are obtained in the kinetic model, and the dashed curves, in the hydrodynamic model.

(where $x_{\alpha s}$ and $p_{\alpha s}$ are the coordinate and momentum of the sth particle of species α) satisfy the initial conditions (8) and allow us to represent the energy integral (7) as

$$W_f + W_p + \delta W_b = 0, \quad W_f = \frac{\langle E^2 \rangle}{8\pi n_b mc^2 \gamma_0},$$
$$W_p = \frac{1}{N_b \gamma_0} \sum_{s=1}^{N_p} \gamma_{ps}, \quad \delta W_b = -1 + \frac{1}{N_b \gamma_0} \sum_{s=1}^{N_b} \gamma_{bs}, \tag{10}$$

where $n_b = \sigma N_b / l$ is the beam density, $mc^2\gamma_0$ is the initial beam energy, and l is the length of the space interval.

Below, we will present the results of numerical integration of the set of equations with a self-consistent field for a plasma with $N_p = 64512$ electrons and a monoenergetic beam consisting of $N_b = N_p/64$ relativistic electrons. Our computations were carried out with the dimensionless parameters

$$\tau = \omega_p t, \ L = \omega_p l / c, \ \beta_{\alpha s} = v_{\alpha s}/c = p_{\alpha s}/mc\gamma_{\alpha s}.$$

The length l of the space interval was chosen to be equal to the wavelength λ. We found that small perturbations ($W_f(0) \sim 10^{-6}$) with a wavelength above the threshold value were unstable and grew exponentially with time at the growth rate (4).

The computation results shown in Fig. 3a enable us to analyze the time evolution of the energy density $-\delta W_b = W_f + W_p$ of Langmuir oscillations for different beam energies. As γ_0 increases, the energy lost by the beam grows and becomes maximum at $\alpha \simeq 1$. In the energy range $\alpha > 1$, the fraction of the energy that is transferred from the beam to the plasma is reduced and the oscillation energy in the plasma increases slower because of a relativistic decrease in the growth rate $\delta \sim 1/\gamma_0$.

Figure 3b shows extremes of the function $-\delta W_{bm}$ that correspond to the first peak in the function $-\delta W_b(t)$. A comparison with the time-dependent solution to equations (2) shows that the oscillation energy obtained from the kinetic model of a plasma is lower than that evaluated from the hydrodynamic model.

An exponentially growing solution to equations (6) can be obtained under the conditions of the plasma and phase resonances, $\omega = \omega_p = (2\sigma k e^2 N_p/m)^{1/2}$ and $\omega = k v_0$. These conditions imply that the plasma frequency and the perturbation wavelength both depend on the beam velocity $v_0 = \beta_0 c$,

$$\omega_p = 2\pi c/\lambda, \ \lambda = \lambda_R \beta_0^2, \ \lambda_R = \pi mc^2/\sigma e^2 N_p. \tag{11}$$

Unlike the hydrodynamic model (2), in which the density is constant and $\lambda \sim \beta_0$, in the kinetic model, the number of particles N_p is fixed and the wavelength is proportional to the squared beam velocity, $\lambda \sim \beta_0^2$. The computed profiles $L(\beta_0)$ and $L(\gamma_0)$ shown in Fig. 4 agree fairly well with formula (11).

For a nonrelativistic beam ($\beta_0 = 0.1$), the plasma heating during the instability is insignificant and the time evolutions of $-\delta W_b(t)$ in Fig. 1a obtained from the kinetic and hydrodynamic models are fairly close to each other. For an REB with $\gamma_0 = 3$, the amplitude of the nonlinear phase oscillations of the field is markedly lower (Fig. 1b).

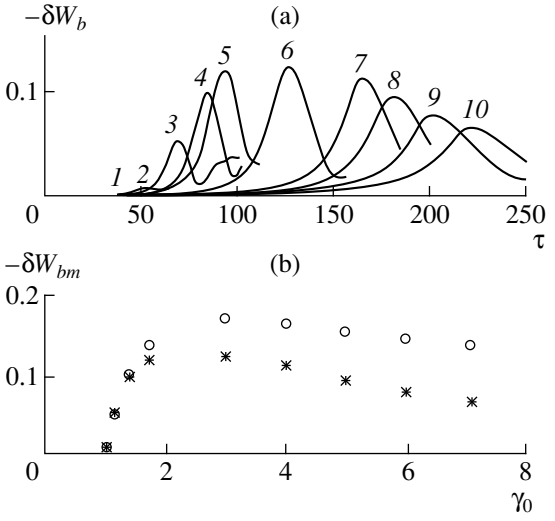

Fig. 3. (a) Energy density of Langmuir oscillations for a beam with the energy γ_0 = (*1*) 1.005, (*2*) 1.02, (*3*) 1.15, (*4*) 1.4, (*5*) 1.75, (*6*) 3, (*7*) 4, (*8*) 5, (*9*) 6, and (*10*) 7. (b) Maximum oscillation amplitude versus the beam energy in the kinetic (asterisks) and hydrodynamic (circles) plasma models.

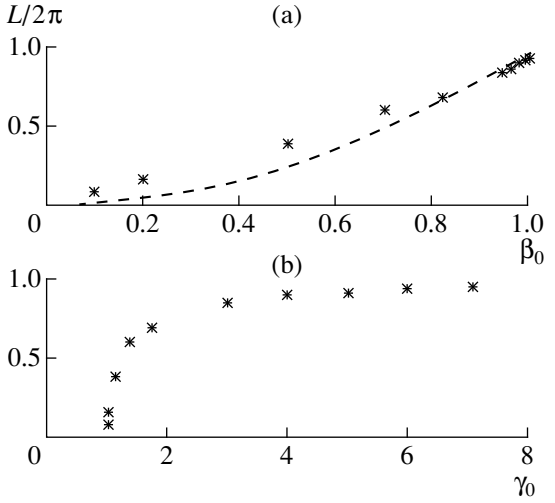

Fig. 4. The wavelength of the unstable mode as a function of (a) the beam velocity and (b) the beam energy. The dashed curve corresponds to the function β_0^2.

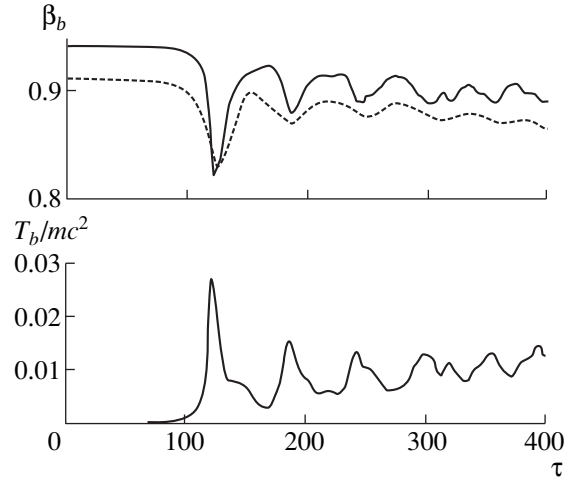

Fig. 5. Average beam velocity β_b and beam temperature T_b (in units of mc^2) for $\gamma_0 = 3$ as a function of time. The dashed curve corresponds to the phase velocity of a nonlinear wave.

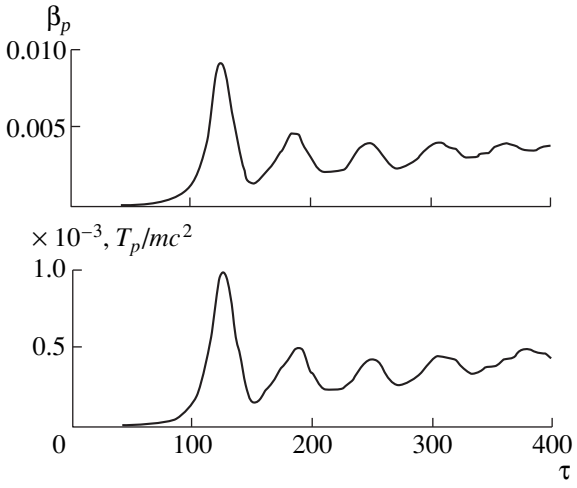

Fig. 6. Average plasma velocity β_p and plasma temperature T_p (in units of mc^2) for $\gamma_0 = 3$ as a function of time.

At $\tau \le 300$, the functions $W_f(\tau)$ and $W_p(\tau)$ are essentially the same and agree fairly well with the following formula in terms of macroscopic electrodynamics [19]:

$$W_f + W_p = \frac{d}{d\omega}(\omega\varepsilon)W_f \simeq 2W_f, \quad \varepsilon = 1 - \omega_p^2/\omega^2. \quad (12)$$

According to (12), under the resonance condition $\varepsilon = 0$, the energy lost by the beam is shared equally between the field and the plasma electrons. In a later stage, when the field energy W_f is converted into the energy W_p of the plasma electrons (Fig. 2a), the evolutions of these functions differ greatly from one another. In this stage of instability, the energy exchange between the beam and the wave is almost completely absent. In the final stage ($\tau > 1000$), the function $-\delta W_b = W_f + W_p$ approaches an asymptotic about which an analogous hydrodynamic solution to equations (2) oscillates nonlinearly (Fig. 2b). Note that the sum of the functions W_f and W_p shown in Fig. 2b experiences no small-scale oscillations, which means that they are periodic functions in τ.

The average velocity of the particles of species α is defined as

$$\beta_\alpha = \frac{1}{N_\alpha}\sum_{s=1}^{N_\alpha}\beta_{\alpha s}, \quad (13)$$

and their temperature coincides with the mean kinetic energy of a plasma flow moving with the velocity β_α,

$$T_\alpha/mc^2 = \frac{1}{N_\alpha}\sum_{s=1}^{N_\alpha}\frac{1-\beta_{\alpha s}\beta_\alpha}{(1-\beta_{\alpha s}^2)^{1/2}} - (1-\beta_\alpha^2)^{1/2}. \quad (14)$$

For a nonrelativistic plasma such that $\beta_{ps} \ll 1$ and $\beta_p \ll 1$, formula (14) can be simplified to $T_p = mc^2(\overline{\beta_{ps}^2} - \beta_p^2)/2$, where $\overline{\beta_{ps}^2}$ is the mean squared particle velocity.

In Figs. 5 and 6, plots are given of the functions $\beta_{b,p}(t)$ and $T_{b,p}(t)$, which describe the time relaxation of the directed velocity and temperature of the beam and plasma. In Fig. 5, the dotted curve shows the nonlinear wave phase velocity calculated from the empirical formula [12]

$$v_{ph}/v_0 = 1 - 2^{-4/3}[\nu^{1/3}/\gamma_0 + \sqrt{3}(W_f + W_p)]. \quad (15)$$

The plots shown in Fig. 7 illustrate the time evolution of the beam and plasma electron distribution functions, $f_b(\beta)$ and $f_p(\beta)$, in velocity space β for a beam with the initial energy $\gamma_0 = 3$. The electrons of each species α are divided into 50 groups with nearly equal electron velocities $\beta_{\alpha j}$. If the number of electrons of species αj is $n_{\alpha j}$, then, by definition, we have

$$f_{\alpha j} = \frac{n_{\alpha j}}{N_\alpha}, \quad (16)$$

where N_α is the number of particles of species α.

Before the time $\tau \approx 120$, at which the oscillation amplitude saturates, a tail of decelerated electrons forms on the beam distribution function. Thereafter, the oscillation energy is partially converted back into beam energy and the beam distribution function subsequently does not undergo any qualitative change (Fig. 7). The expansion of the plasma electron distribution function in velocity space illustrates electron heating by the field of the unstable mode.

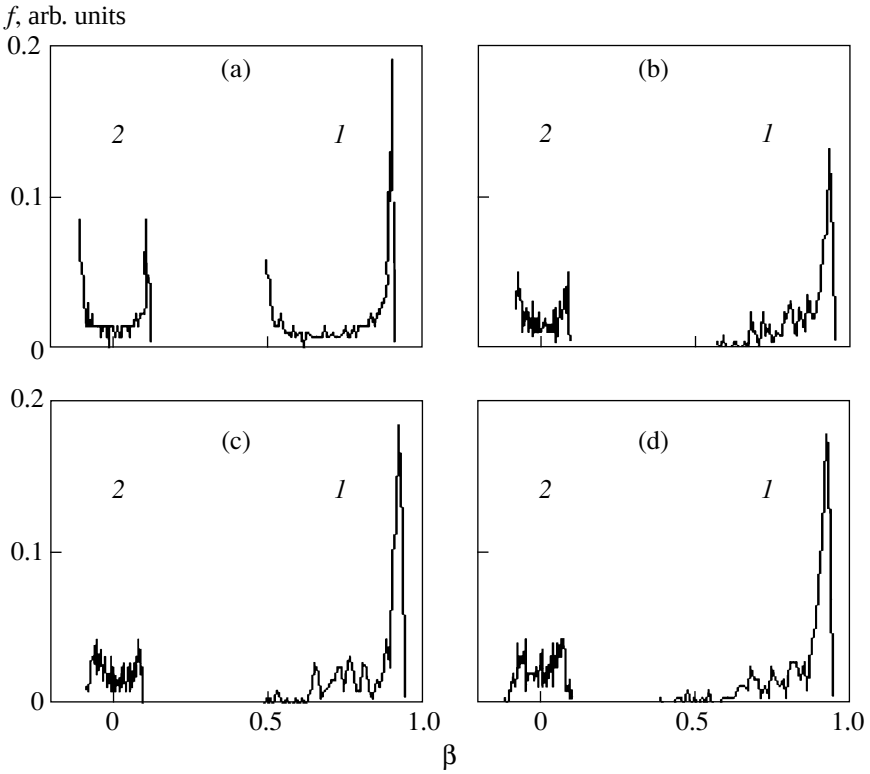

Fig. 7. Distribution functions of the (*1*) beam and (*2*) plasma electrons for $\gamma_0 = 3$ at different times τ = (a) 120, (b) 180, (c) 300, and (d) 360.

4. MODULATIONAL INSTABILITY

Numerical simulations show that, during the oscillatory instability of the primary spectrum, the energy of the plasma ions grows [4, 5] due to both the onset of a parametric instability and the decay of a pump wave into Langmuir and ion acoustic modes [8]. In the immobile-ion approximation, the field energy is converted into the energy of the plasma electrons because of the onset of the modulational instability of the wave (the self-compression of Langmuir wave packets in a heated plasma) [18].

Numerical integration shows that, in the stage of the high-frequency modulation of the wave amplitude, the energy exchange between the beam and the wave field is almost completely absent (Fig. 2). Consequently, following [18], we can find the growth rate of the modulational instability from the nonlinear parabolic equation without allowance for the trapped particles.

Setting the right-hand side of the first of equations (2) to zero, we represent the solution as

$$\begin{gathered} E = (E_0 + E_1 + iE_2)\exp(-i\Omega_0 t), \\ \Omega_0 = -(\omega_p/2)(\varepsilon + E_0^2/E_T^2), \\ E_1 \ll E_0, \quad E_2 \ll E_0, \quad E_1, E_2 \sim \exp(-i\Omega t + ikx), \\ E_T^2 = 32\pi n_p T. \end{gathered} \tag{17}$$

Substituting (17) into (2) yields the dispersion relation [18]

$$(\Omega - kv_g)^2 = \frac{\omega_p^2 k^2 \lambda_d^2}{4}(-Q_0 + k^2\lambda_d^2), \quad Q_0 = \frac{W}{n_p T}, \tag{18}$$

where $W = E_0^2/16\pi$ is the wave energy density, $v_g' = \omega_p \lambda_d^2$, λ_d is the Debye length, and $v_g \simeq v_T^2/v_0$. The dispersion relation (18) implies that the modes with wavenumbers $k^2\lambda_d^2 < Q_0$ are unstable. The maximum growth rate $\delta_{\text{mod}} = \text{Im}\,\Omega$ of the modulational instability is

$$\delta_{\text{mod}} = \omega_p Q_0/4, \quad k^2\lambda_d^2 = Q_0/2. \tag{19}$$

Numerical experiments in which the condition $Q_0 \simeq W_f/W_p \simeq 1$ holds over a sufficiently long time interval $T \leq 1000$ showed that the functions $W_f(T)$ and $W_p(T)$ become modulated at a high frequency, the modulation period being about $\delta_{\text{mod}}^{-1} = 4\omega_p^{-1}$ (Fig. 8). An increase in the amplitude of electron oscillations with $k\lambda_d > 0.1$ results in the energy transfer from the wave with $k_0 = \omega_p/v_0$ to short-wavelength oscillations. The secondary waves are damped via Landau damping, and their energy is converted into the energy of the plasma electrons [8].

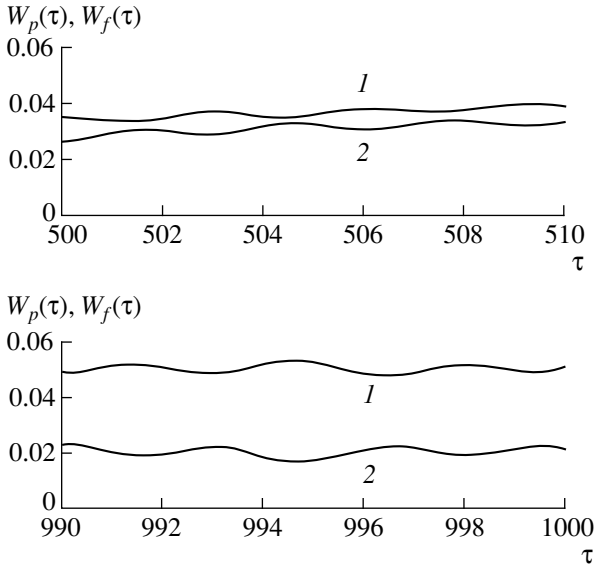

Fig. 8. Functions (*1*) $W_p(\tau)$ and (*2*) $W_f(\tau)$ over different time intervals (fragments of Fig. 2a).

5. THE MAIN RESULTS

Numerical integration of the Vlasov set of equations with a self-consistent field demonstrates the possibility of converting the energy of an REB into the energy of a regular Langmuir wave in a plasma. For a beam with $n_b/n_p = 1/64$ and $\gamma_0 = 3$ ($\alpha \approx 3/4$ and $\delta/\omega_p \approx 0.06$), the energy density of Langmuir oscillations amounts to approximately 12% of the beam energy density (Fig. 1b).

An analysis of the functions $W_p(\tau)$, $W_f(\tau)$, and $-\delta W_b(\tau)$ shows that the instability occurs in three stages (Fig. 2).

A small perturbation that increases exponentially with the hydrodynamic growth rate δ stops growing at the time $\tau \approx 120$, when the instability is suppressed by the trapping of beam electrons by the wave. By this time, the beam energy becomes minimum and a tail of decelerated electrons forms on the distribution function of the initially monoenergetic beam (Fig. 7). As the field passes through a maximum, the mean beam velocity and beam temperature undergo jumps, which correspond to the conversion of a fraction of the energy of directed electron motion into thermal plasma energy (Fig. 5).

In the second stage of the nonlinear relaxation of a beam in a plasma, the beam electrons are accelerated by the wave field and the field energy is partially converted back into beam energy. As a result, at $\tau > 120$, the mean beam velocity, first, increases and, then, experiences weakly damped oscillations. The oscillations of the beam and plasma temperatures are in antiphase with the oscillations of the directed beam velocity (Figs. 5, 6). Analyzing the shape of the beam distribution function shown in Fig. 7 at different times, we can conclude that only a small fraction of decelerated electrons in the tail of the distribution function interact with the wave.

In the final stage of evolution of the beam–plasma system ($\tau > 1000$), the energy exchange between the beam and the wave is almost completely absent. The field energy is converted into the energy of plasma electrons and the functions $W_f(\tau)$ and $W_p(\tau)$ differ greatly from each other. However, their sum $-\delta W_b(\tau) = W_f(\tau) + W_p(\tau)$, describing the energy lost by the beam, approaches an asymptotic about which the analogous nonlinear solution found in [16] oscillates (Fig. 2b).

The fact that the sum of the functions $W_f(\tau)$ and $W_p(\tau)$ experiences no high-frequency oscillations indicates that the modulation of the primary wave amplitude is regular. Figure 8 shows the fragments of Fig. 2a at different times. The modulation period is on the order of the inverse growth rate of the modulational instability.

The density and energy of REBs used in our simulations correspond to the parameters of the HDZP-II experimental device (University of Nevada, Reno, USA).

ACKNOWLEDGMENTS

We are grateful to F. Wittenberg and B. Bauer for providing us with information about the HDZP-II device and to M.V. Maslennikov and V.V. Vedenyapin for fruitful discussions.

REFERENCES

1. Ya. B. Faĭnberg, V. D. Shapiro, and V. I. Shevchenko, Zh. Éksp. Teor. Fiz. **57**, 966 (1969) [Sov. Phys. JETP **30**, 528 (1970)].
2. R. I. Kovtun and A. A. Rukhadze, Zh. Éksp. Teor. Fiz. **58**, 1709 (1970) [Sov. Phys. JETP **31**, 915 (1970)].
3. N. G. Matsiborko, I. N. Onischenko, V. D. Shapiro, and V. I. Shevchenko, Plasma Phys. **14**, 591 (1972).
4. L. E. Thode and R. N. Sudan, Phys. Rev. Lett. **30**, 732 (1973).
5. L. E. Thode and R. N. Sudan, Phys. Fluids **18**, 1552 (1975).
6. M. Lampe and P. Sprangle, Phys. Fluids **18**, 475 (1975).
7. L. E. Thode, Phys. Fluids **19**, 305 (1976).
8. R. N. Sudan, in *Basic Plasma Physics: Supplement to the Second Volume*, Ed. by A. A. Galeev and R. N. Sudan (Énergoatomizdat, Moscow, 1984), p. 38.
9. M. V. Kuzelev and A. A. Rukhadze, *Electrodynamics of Dense Electron Beams in a Plasma* (Nauka, Moscow, 1990).
10. R. Ando, V. A. Balakirev, K. Kamada, *et al.*, Fiz. Plazmy **23**, 1042 (1997) [Plasma Phys. Rep. **23**, 964 (1997)].
11. V. B. Krasovitskiĭ and V. I. Kurilko, Zh. Éksp. Teor. Fiz. **51**, 445 (1966) [Sov. Phys. JETP **24**, 300 (1967)].

12. V. B. Krasovitskiĭ and L. A. Mitin, Fiz. Plazmy **23**, 230 (1997) [Plasma Phys. Rep. **23**, 209 (1997)].

13. V. B. Krasovitskiĭ, Zh. Éksp. Teor. Fiz. **83**, 1324 (1982) [Sov. Phys. JETP **56**, 760 (1982)].

14. V. G. Dorofeenko, V. B. Krasovitskiĭ, and G. V. Fomin, Zh. Éksp. Teor. Fiz. **98**, 419 (1990) [Sov. Phys. JETP **71**, 234 (1990)].

15. M. V. Kuzelev and A. N. Khalilov, Vestn. Mosk. Gos. Univ., Ser. 3: Fiz., Astron. **31**, 27 (1990).

16. V. B. Krasovitskiĭ, Fiz. Plazmy **22**, 728 (1996) [Plasma Phys. Rep. **22**, 659 (1996)].

17. V. B. Krasovitskiĭ and G. V. Fomin, Fiz. Plazmy **24**, 904 (1998) [Plasma Phys. Rep. **24**, 841 (1998)].

18. B. B. Kadomtsev, *Collective Phenomena in Plasmas* (Nauka, Moscow, 1988).

19. L. D. Landau and E. M. Lifshitz, *Electrodynamics of Continuous Media* (Pergamon, Oxford, 1960).

Translated by I. A. Kalabalyk

Plasma Physics Reports, Vol. 26, No. 1, 2000, pp. 78–83. Translated from Fizika Plazmy, Vol. 26, No. 1, 2000, pp. 81–86.

LOW-TEMPERATURE PLASMA

Properties of a Spherical Stratified Gas Discharge

O. A. Nerushev, S. A. Novopashin, V. V. Radchenko, and G. I. Sukhinin

Institute of Thermophysics, Siberian Division, Russian Academy of Sciences, pr. akademika Lavrent'eva 1, Novosibirsk, 630090 Russia

Received December 11, 1997; in final form, January 20, 1999

Abstract—Experimental data are obtained on the conditions for the stratification of spherical direct-current discharges and on the properties of the strata. The experiments were aimed at studying discharges in both molecular and inert gases at low pressures and were carried out with a steel chamber whose wall served as a cathode. An anode was placed at the center of the chamber. The discharge stratification was observed to be especially pronounced in media containing a small admixture of the vapor of a high-molecular substance (e.g., acetone). In discharges in pure inert gases, no strata were observed. The current–voltage characteristics of discharges at different pressures were obtained. The discharges were found to be unsteady: current pulses with a duration of about 1 microsecond and a characteristic repetition rate of about 1 kHz were detected against a steady current background and were found to correlate with the pulses of the integral emission from the discharge. The radius of each of the strata was determined as a function of its number and of the gas pressure and discharge current. The radial profiles of the time-averaged floating potential were measured in experiments with stratified discharges and with uniform discharges in argon. © *2000 MAIK "Nauka/Interperiodica".*

1. INTRODUCTION

The formation of alternating dark and bright regions (strata) in the positive column of a glow discharge is a universal property of discharges in tubes. This phenomenon is observed in discharges in atomic and molecular gases at pressures from 1 to 10^4 Pa. The strata can be either stationary regions or can move with a velocity up to 10^5 cm/s. At present, discharge stratification in gas-discharge tubes is attributed to the ionization instability and the strata themselves are referred to as ionization waves [1–4]. The stratification phenomena in discharges are now described by two theoretical approaches, which complement one another. The main advantage of the first approach, which is based on the kinetic equation [5, 6], is that it takes into account the nonlocal character of the electron distribution function. A drawback of this approach is that the problems are resolved in a non-self-consistent fashion: the electric field either should be taken from the probe measurements or should be specified on the basis of model considerations. The second approach, which is based on Poisson's equation in the hydrodynamic approximation [3, 7], does not take into account the nonlocal nature of electron kinetics but makes it possible to solve the problems self-consistently. For these reasons, an adequate theoretical description of the stratification is still lacking even for discharges in tubes. Note also that the detailed theory of stratification in discharge tubes is essentially two-dimensional, so that the particle distributions along and across the tube axis should be described with allowance for the radial field profiles and particle diffusion toward the tube walls.

Nerushev *et al.* [8] were the first to record strata in experiments with spherically symmetric gas discharges. Mathematically, the spherical strata (unlike the strata in discharge tubes) are essentially one-dimensional; consequently, they are much simpler to describe. The construction of a self-consistent theory of the spherical strata is the subject of further theoretical investigations. Here, we present experimental data on the conditions for stratification of spherical direct-current discharges and on some of the properties of the strata.

2. EXPERIMENTAL SETUP

Figure 1 shows a schematic of the experimental device. The experiments were carried out with a cylindrical steel chamber, 60 cm in height and 50 cm in diameter. A steel ball of radius 0.6 cm, which was positioned at the geometric center of the chamber, served as the central electrode. The grounded steel wall of the vacuum chamber served as another electrode. The chamber was equipped with optical windows at the half-height of the cylindrical wall. The windows provided visual observations and were used to photograph discharges, to record the spatial modulation of the discharge luminosity by a high-speed multichannel optical analyzer with a spatial resolution of 0.1 mm, and to measure the integral emission from the discharge by a photomultiplier. The voltage and current of the discharge were recorded in the course of experiments. The discharge current was recorded with the help of one of the channels of a two-channel oscilloscope. The current from a photomultiplier, which was used to detect optical signals from the discharge region, was fed to

1063-780X/00/2601-0078$20.00

another channel of the oscillograph. The chamber was pumped down to a pressure of 10^{-1} Pa and, then, was filled with the gas mixture under study to a certain pressure. In our experiments, which were aimed at studying discharges in the pressure range from 5 to 500 Pa, the gas pressure was recorded by a deformation manometer and a thermocouple pressure gauge. The measurements were performed in the steady regime (when the vacuum pump was shut off and the chamber was filled with a working gas mixture) and in the dynamic regime (when the vacuum pump with a pumping rate of 5 l/s was operating continuously and both air and the vapors of high-molecular admixtures were puffed into the chamber through controlled leaks). In the experiments, we varied the relative content of the vapors and air. The radial profile of the time-averaged floating potential of the discharge plasma was measured by a 3-mm-long movable tungsten probe 0.26 mm in diameter, which could be moved with a step of 1 mm in the radial direction at the half-height of the chamber. The probe potential was recorded by a C-95 high-resistance electrostatic voltmeter.

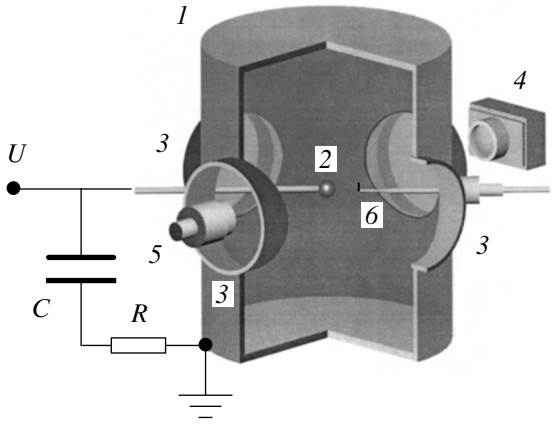

Fig. 1. Schematic of the experimental device: (*1*) steel vacuum chamber, (*2*) central electrode, (*3*) optical windows, (*4*) high-speed multichannel optical analyzer, (*5*) FEU- 84 photomultiplier, and (*6*) electric probe. The parameters of the power supply are U = 0–2.3 kV, C = 4 μF, and R = 24 kΩ.

3. EXPERIMENTAL RESULTS

The discharge was ignited by applying an excessive voltage (above the breakdown one) at the central electrode. After being initiated, the discharge evolved (under certain conditions) into a state with closed, nested bright striations—strata (the number of which varied from one to more than ten). The stratification could be achieved only when a positive voltage was applied to the central electrode. Figure 2 shows a photograph of a discharge with three spherical strata and with the central spherical bright core. The number of strata and their dimensions depend on the magnitudes of the pressure and discharge current and on the gas composition. The strata were observed to appear in discharges with a current from 5 to 80 mA in a pressure range from 5 to 100 Pa.

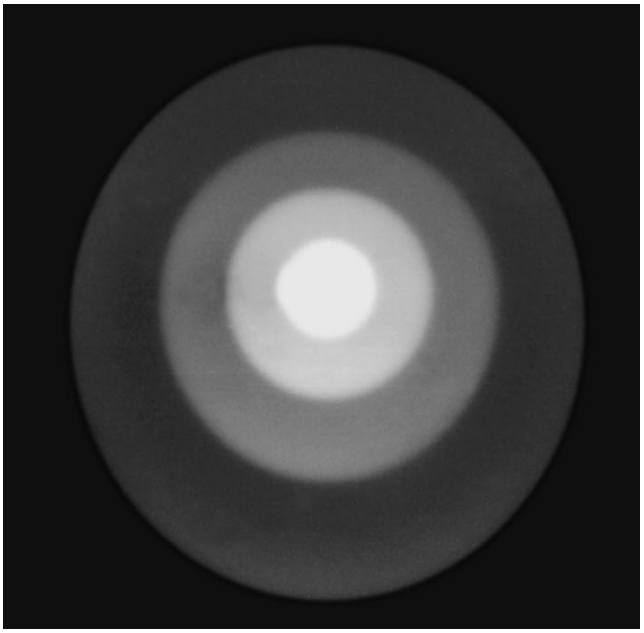

Fig. 2. Photograph of a spherically symmetric stratified discharge in air at p = 20 Pa and I = 40 mA.

Figure 3 illustrates the results of measuring the dependence of the radius R_n of each stratum on its number n. The radii of the strata are normalized to the radius R_0 of the central bright core. The data presented were obtained by processing photographs and then applying a time-averaging technique. An essential feature of the bright core is that its radius does not enter into the empirical dependence

$$R_{n+1}/R_n = \alpha, \quad (1)$$

which is valid for all of the remaining strata. The coefficient α, which depends on the current magnitude and gas composition, varies from 1.4 to 2. Figure 4 shows that the radii of the strata are almost inversely proportional to the gas pressure. Lower-current discharges evolve into states with a smaller number of strata of smaller radii (see Fig. 5, in which the numerals above the points denote the order numbers of the strata). The outer strata may be nonspherical in shape, in which case their boundaries are stretched out toward cavities in the chamber wall (the holes through which detectors are inserted into the chamber and the pipes for pumping out and gas supply). Presumably, the current density in these directions is elevated, so that, according to our measurements of the dependence of the radii of the strata on the discharge current, the boundaries of the outer strata in these directions should lie farther from the central electrode. A photograph of a nonspherical discharge is shown in Fig. 6.

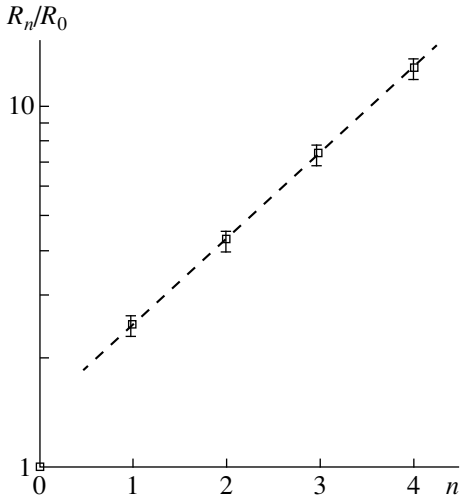

Fig. 3. Dependence of the radii R_n of the strata on their order number n (determined from the central sphere, $n = 0$) for a discharge in air at $p = 20$ Pa and $I = 40$ mA. The radii of the strata are normalized to the radius R_0 of the central bright core. The dashed line corresponds to the dependence $R_{n+1}/R_n = \alpha$ with $\alpha \approx 1.74$.

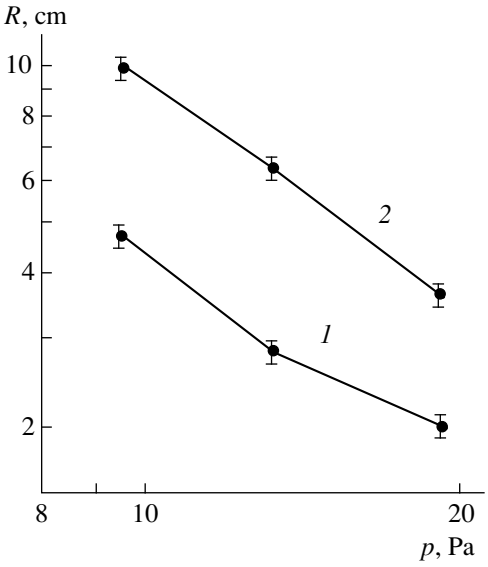

Fig. 4. Dependence of the radii of the first two strata ($n = 1, 2$) on pressure for a discharge in air at $I = 40$ mA.

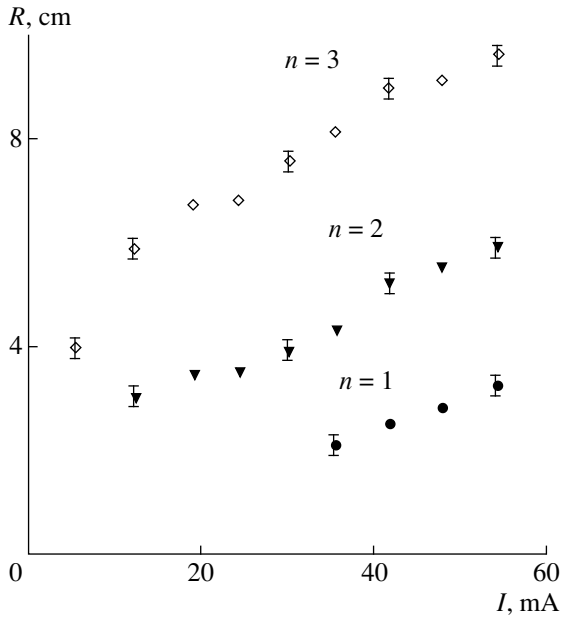

Fig. 5. Dependence of the radii of the strata on the discharge current for a discharge in air at $p = 20$ Pa. The numerals above the points denote the order numbers n of the strata.

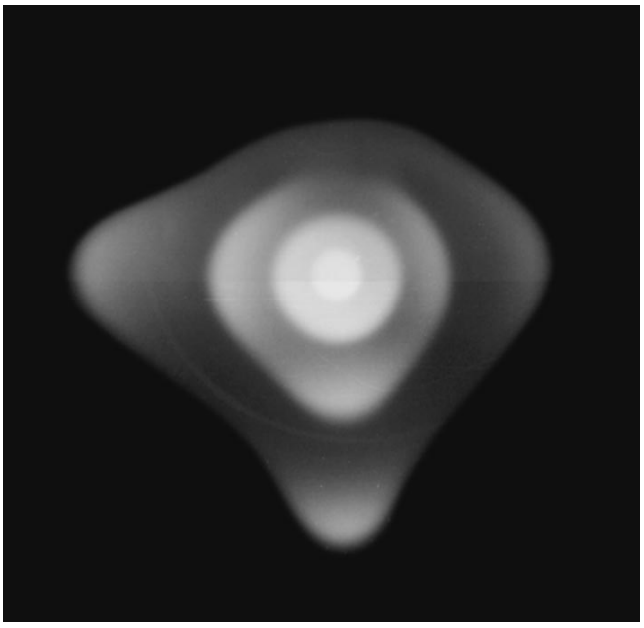

Fig. 6. Photograph of a nonspherical stratified discharge in air at $p = 30$ Pa and $I = 40$ mA.

Figure 7 shows the current–voltage characteristics of discharges in air at different pressures when a positive voltage is applied to the central electrode. As the discharge current is changed by more than an order of magnitude, the voltage changes insignificantly, which is typical of normal glow discharges in tubes. Note also that, at a fixed current, the discharge voltage increases monotonically as the pressure decreases. In the case of opposite polarity, such that the central electrode serves as a cathode, in the pressure range under study, the dis-

charge voltage coincides essentially with the voltage at the power supply, the discharge current is much lower, and no strata are observed.

Oscillograms of the anode current and discharge voltage showed that the discharge is unsteady: aperiodic current pulses with a characteristic duration of about 1 microsecond and a characteristic repetition rate from 0.1 to 1 kHz were detected against the mean current background. At the times when the current is peaked, the discharge voltage falls off far below its mean value. The recording of the emission from the discharge showed that the space-averaged emission intensity is also unsteady and its peaks are correlated with the current pulses. Note also that the background emission intensity between the peaks is lower than the peak intensities by two orders of magnitude. Figure 8 shows the corresponding oscillograms of the discharge voltage and the intensity of emission from the strata.

The unsteady character of the discharge current hinders the recording of the current–voltage characteristics of the Langmuir probe, which provide information on the distribution function, electron temperature, and electron density in different zones of the discharge. The peaks in the perturbed potential measured by the probe are correlated with the peaks of the discharge current. In our experiments, we measured only the time-averaged floating potential, the time constant being about 1 s. Figure 9 illustrates the radial profiles of the floating potential U_{fl} in a stratified discharge and in a discharge with no strata. We can see that there is a region in which the cathode potential falls off; the width of this region, which is situated near the outer electrode, is about 2–3 cm (see the vertical dashed line with *C*). For a stratified discharge, the gradient of the floating potential is nonzero from the central region of the chamber up to the anode surface (R = 0.6 cm). A discharge in argon (when no strata are observed) does not have this property. The radius from which the discharge potential begins to increase toward the center coincides with the boundary of the outermost stratum (see the vertical dashed-and-dotted line *S*).

One of the problems is to determine the composition of the gas in which the discharge can evolve into a stratified state. Our experiments were carried out with purely molecular gases (air, N_2, CO_2, O_2); inert gases (Ar, He, Kr); and admixtures of high-molecular gases, e.g., acetone (C_3H_6O), benzene (C_6H_6), dimethyl-formamide (C_2H_7ON), pentane (C_5H_{12}), ethyl acetate ($C_2H_8O_2$), ethanol (C_2H_5OH), and iodine methyl (CH_3J). In discharges in inert gases, no stratification was observed. In discharges in low-molecular gases with no admixtures, the smeared-out boundaries between strata are pronounced only slightly, in which case the bright regions of the discharge are observed to strongly pulsate in space. However, even a small admixture of a high-molecular gas (except for iodine methyl) to molecular or inert gases results in a well-pronounced discharge stratification. In contrast, in gases with a small admixture (about several percent) of iodine methyl, the stratification is completely suppressed and no strata appear. This is likely due to the fact that the degree to which the iodine methyl mole-

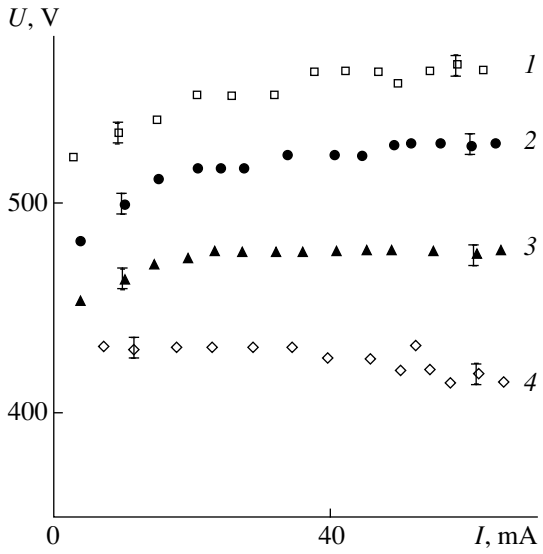

Fig. 7. Current–voltage characteristics of discharges in air at pressures p = (*1*) 10, (*2*) 15, (*3*) 20, and (*4*) 30 Pa. The anode is placed at the center of the chamber.

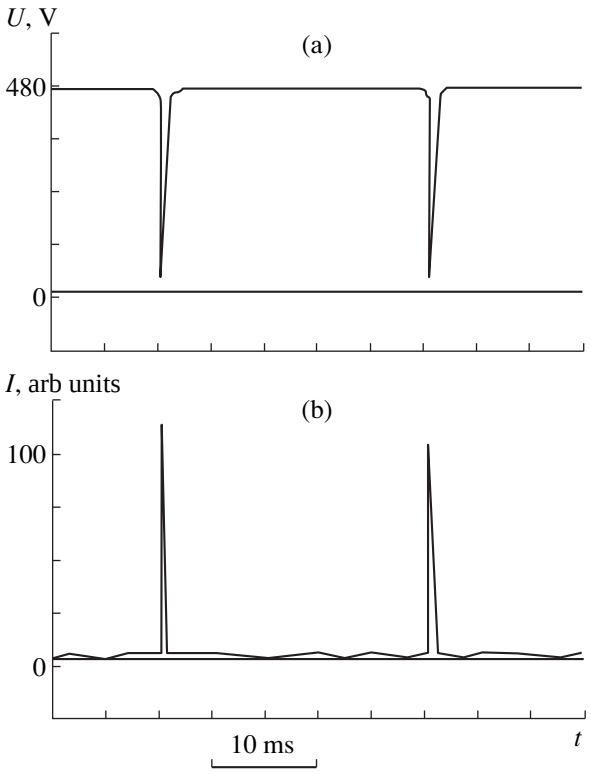

Fig. 8. Oscillograms of (a) the discharge voltage and (b) the intensity of emission from the discharge region for a discharge in air. The anode is placed at the center of the chamber.

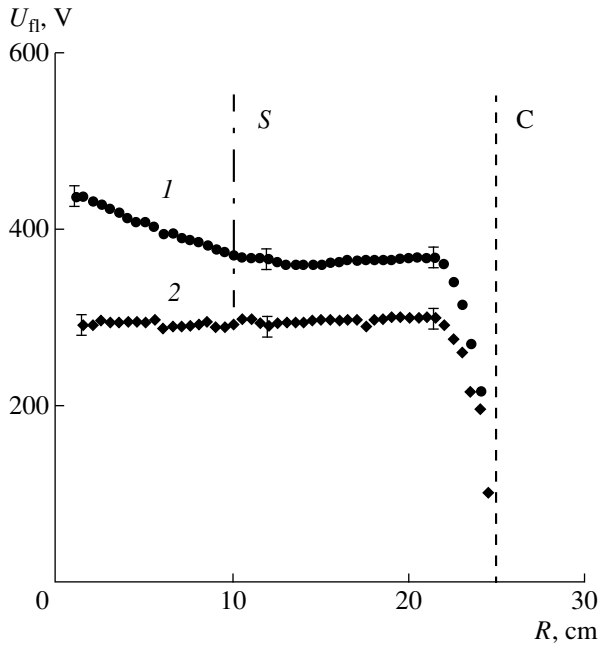

Fig. 9. Floating potential U_{fl} versus the radius R of the discharge chamber (the anode is placed at the center of the chamber): (*1*) a stratified discharge with three strata in air at p = 20 Pa and I = 40 mA (dashed-and-dotted line S corresponds to the boundary of the outermost striation) and (*2*) a discharge with no strata in argon at p = 18 Pa and I = 50 mA (dashed line C corresponds to the position of the cathode).

cules are electronegative is high. We failed to experimentally establish the minimum density of high-molecular admixtures required for stratification. Our observations showed that the discharge stratification is well pronounced in argon with a small (less than one percent) acetone admixture. In the series of experiments with no gas circulation, the time during which the discharge stayed in a stratified state was found to depend on the initial gas composition and to vary from several seconds to tens of minutes. In the course of the glow, the number of strata in the discharge progressively decreased and the discharge evolved into the state with no strata. After the disappearance of the strata, the stratification could again be observed in a discharge, which was ignited several minutes after the previous discharge was switched off. During the discharge, the gas composition was difficult to record. However, we can now state that the change in the gas composition (due to dissociation, the appearance of particles in metastable states and molecular ions, etc.) should be taken into account in order to understand the nature of the stratification of spherical discharges.

4. CONCLUSIONS

We have presented experimental data on some of the properties of strata and on the conditions for stratification of spherical discharges. The most important results are as follows:

(i) The stratification of spherical discharges was observed only when a positive potential was applied to the central electrode.

(ii) The current–voltage characteristics of the discharges agree with those of normal glow discharges in tubes.

(iii) Although our experiments were carried out with a constant-voltage power supply, the discharges were unsteady and were accompanied by "breakdowns," during which the discharge impedance decreased rapidly, thereby causing the discharge current to grow and the discharge voltage to fall off.

(iv) The current pulses were found to be correlated with the peaks in the space-averaged intensity of emission from the discharge region.

(v) In spherical stratified discharges, the time-averaged floating potential increased from the boundary of the outermost striation toward the central electrode (anode).

(vi) For a spherical stratified discharge to be steady, it should be ignited in a gas mixture with a small admixture of a high-molecular gas. (In connection with this, we note the paper by Conde and Leon [9], who observed numerous semispherical double layers in a discharge in a radially expanding flow of pure argon. However, the nature of this phenomenon is likely to differ from that of the phenomenon we are describing here.)

(vii) During the discharge, the gas composition changed, thereby causing the strata to disappear.

In conclusion, we estimate some discharge parameters under the assumption that the plasma is quasineutral and the discharge is steady ($\mathrm{div}\,\mathbf{j} = 0$, where $\mathbf{j}$ is the electron current density), in which case the ionization and recombination processes should be in local equilibrium. For discharges in air at the pressure p = 20 Pa, discharge current 50 mA, and voltage U = 500 V across the discharge gap, we can estimate the electron density from the known empirical rates of these processes as functions of pressure and the electric field [4, 10]: near the central electrode (anode) of radius 0.5 cm, we have $n_e = 5 \times 10^9$ cm^{-3}, and, at a distance of 20 cm from the center of the chamber, we have $n_e = 6 \times 10^6$ cm^{-3}. Accordingly, the reduced electric field E/p varies in the range from 40 to 20 V/(cm torr). The estimates also show that the Debye radius increases almost linearly from 0.02 cm at the anode to 0.5 cm at the cathode.

Note also that the discharges under study possess properties peculiar to both corona and glow discharges. For example, in experiments with positive corona discharges at atmospheric pressure (see, e.g., [11]), the current was observed to be unsteady in character (to exhibit breakdownlike behavior): the characteristics of this phenomenon are close to the characteristics described above. Morrow [12] theoretically analyzed the results of those experiments with allowance for negative molecular ions of oxygen and metastable mole-

cules. In our experiments, the electric field near the anode is above the threshold for breakdown in the pressure range under consideration. This indicates that our experimental conditions are favorable for the onset of corona discharges. The question of how the unsteady character of the process is related to stratification remains unclear, but the feature we have just pointed out may be of great importance in describing the mechanism for the formation of strata. This feature may give rise to new phenomena, among which is likely to be the spherical stratification we have described here.

REFERENCES

1. A. V. Nedospasov, Usp. Fiz. Nauk **94**, 439 (1968).
2. L. Pekarek, Usp. Fiz. Nauk **94**, 463 (1968).
3. P. S. Landa, N. A. Miskinova, and Yu. V. Ponomarev, Usp. Fiz. Nauk **132**, 601 (1980).
4. Yu. P. Raizer, *Gas Discharge Physics* (Springer-Verlag, Berlin, 1991).
5. F. Sigeneger and R. Winkler, Plasma Chem. Plasma Process. **17**, 281 (1997).
6. F. Sigeneger, G. I. Sukhinin, and R. Winkler, Abstracts of Invited Lectures and Contributed Papers, *XIV Eur. Sectional Conf. on the Atomic and Molecular Processes in Ionized Gases, Malahide, 1998*, p. 160.
7. Yu. P. Raĭzer and M. N. Shneĭder, Teplofiz. Vys. Temp. **35**, 19 (1997) [High Temp. **35** (1997)].
8. O. A. Nerushev, S. A. Novopashin, V. V. Radchenko, and G. I. Sukhinin, Pis'ma Zh. Éksp. Teor. Fiz. **66**, 679 (1997) [JETP Lett. **66**, 711 (1997)].
9. L. Conde and L. Leon, Phys. Plasmas **1**, 2441 (1994).
10. E. D. Lozanskiĭ and O. B. Firsov, *Theory of Sparks* (Atomizdat, Moscow, 1975).
11. A. Bolloud and J. Charrier, J. Phys. D: Appl. Phys. **14**, 207 (1981).
12. R. Morrow, J. Phys. D: Appl. Phys. **30**, 3099 (1997).

Translated by G. V. Shepekina

Plasma Physics Reports, Vol. 26, No. 1, 2000, pp. 84–86. Translated from Fizika Plazmy, Vol. 26, No. 1, 2000, pp. 87–89.

Information for Contributors

The paper must present the results of a completed, original study on any aspect of plasma physics. The results of the study should be relatively general in character. The paper should be understandable and easy to read for specialists in plasma physics and related branches of science. For this purpose, the authors are to clearly formulate the subject and goal of the investigation and the results obtained. The authors are also to give an assessment of the results obtained, define their position among the results obtained by other authors, and indicate the fields in which these results can be applied.

The manuscript should be prepared as carefully as possible. In order to avoid typesetting mistakes and delays in publishing, the authors should follow our instructions and recommendations.

Manuscripts not satisfying the following instructions may be rejected without registration. These instructions are based on the Technical Supplement to the Agreement between the NAUKA International Academic Publishing Company and the Editorial Board of *Fizika Plazmy* (*Plasma Physics Reports*) on the publication of the English translation of the journal.

INSTRUCTIONS FOR PREPARING MANUSCRIPTS

1. General Requirements

1.1. The manuscript should be clearly typed double-spaced on one side of white, A4 (290×210 mm) or Letter ($8\ 1/2 \times 11$ in.) format paper using a standard typewriter (or printer with an appropriate font). The number of lines per page should be 29–30. The left margin should be no less than 25 mm. All pages must be consecutively numbered. Only corrections made in black ink are allowed. The manuscript must be submitted to the Editorial Board in duplicate.

1.2. For efficient communication with the Editorial Board, indicate your e-mail address.

1.3. To hasten the publication of the accepted paper, it is recommended to present an electronic version of the paper (see below).

1.4. The paper must begin with the title followed by the authors' initials and surnames, affiliations, and addresses.

Example:

Possibility for Determining the Isotope Content in a Dense Plasma by Measuring the Flows of Charge-Exchange Atoms

A. V. Khudoleev, V. I. Afanas'ev, and F. V. Chernyshev

Ioffe Institute for Physics and Technology, Russian Academy of Sciences, Politekhnicheskaya ul. 26, St. Petersburg, 194021 Russia

Further, a short abstract follows.

1.5. The manuscript must be carefully edited.

1.6. It is recommended to use SI units and the ^{12}C scale for relative atomic masses. The use of outdated units is undesirable. In papers presenting results of numerical calculations, the authors of numerical codes should be cited.

1.7. All acronyms and abbreviations must be spelled out the first time they are used in the text, except for those generally accepted. There should be no acronyms, abbreviations, or references in the abstract.

2. Mathematical Expressions

2.1. All expressions and notations should be either printed or typed or hand-written legibly and large in black or India ink.

2.2. All formulas and symbols should be supplemented by standard identification marks written in pencil throughout the material (including figures and inscriptions in photographs) as follows.

2.2.1. When upper- and lower-case characters have similar outlines and differ only by their size, upper-case characters should be doubly underlined in black pencil, whereas lower case characters should be marked by two dashes above the character.

2.2.2. Power exponents and superscripts should be marked in black pencil with an inverted caret below, whereas subscripts should be marked with a caret above; complicated indices should be described in the margin.

2.2.3. Vectors should be underlined in blue pencil (do not mark them with an above arrow).

2.2.4. Greek letters should be underlined in red pencil and spelled out in the margin each time they first appear on the page; for example, ξ (xi), ζ (zeta), etc.

2.2.5. Special symbols (e.g., $\notin$, $\supset$) should be identified by marginal notes with the remark "special symbol."

[1] This information concerns papers submitted originally in English. Instructions and recommendations for preparing papers submitted in Russian can be found in the Russian version of the journal.

1063-780X/00/2601-0084$20.00 © 2000 MAIK "Nauka/Interperiodica"

2.2.6. To eliminate possible confusion between symbols with similar outlines, they should be identified by notes in the margin made in black pencil [e.g., *e* (not "el"), *l* ("el"), $\underline{0}$ ("zero"), $\underline{\mathrm{O}}$ ("letter")].

2.2.7. Multiletter mathematical symbols (such as sin, lim, Re, log, max, exp), zeros, and designations of chemical elements should be marked in black pencil by a square bracket from below.

3. Tables

3.1. Numerical data should be presented in the form of tables.

3.2. Tables should be numbered by Arabic numerals in the order in which they are mentioned in the text. It is recommended that the number be followed by the table title.

3.3. All columns must have headings and must be separated by vertical lines.

3.4. The use of abbreviations in tables is not recommended.

4. Figures

4.1. Figures (between 5×6 cm and 18×24 cm in size and with their orientation on the page definitely indicated) must be submitted in duplicate.

4.2. Figures must not be inserted into the running text but should be placed separately in sequence after the collected captions at the end of the manuscript.

4.3. Figures should be informative and should ensure an understanding of all the details; formulas and symbols in inscriptions should be identified by the same marks as in the text. Identify each figure with the figure number and the first author's name on the face side of the figure.

4.4. Photographs must be printed on glossy paper and submitted in duplicate (photocopies of photographs are not acceptable). Each photograph should be identified on the back by the surname of the first author and the number of the photograph written in soft black pencil.

4.5. Information presented in figures and photographs should correspond to captions and text descriptions.

4.6. It is important to avoid overloading figures with inscriptions. All of the text information concerning the figure should be presented in the figure caption. It is recommended to replace lettering in figures by numbers, which should be identified in the figure captions.

4.7. Use a black pencil to indicate in the margin the places within the text where illustrations and tables should be positioned.

5. References

5.1. References to other papers should be listed double-spaced under the title REFERENCES after the text at the end of the manuscript.

5.2. References should be numbered in the order of their citation throughout the manuscript. Within the text, references should appear as consecutive numbers in square brackets (e.g., [1]).

5.3. The reference should cite surnames and initials of all authors, except when there are more than four authors; in this case, cite the first three authors and use *et al.* in place of the names of the other authors.

5.4. References to laboratory reports (preprints) should not contain abbreviations or acronyms for the names of laboratories or agencies; spell them out.

5.5. Examples of reference formatting follow.

5.5.1. Books: A. S. Bakai and V. I. Maslov, in *Nonlinear and Turbulent Processes in Physics*, edited by R. Z. Sagdeev (Harwood, New York, 1984), p. 23.

5.5.2. Journals: S. I. Gritsinin, I. A. Kossyi, V. P. Silakov, *et al.*, J. Phys. D.: Appl. Phys. **29**, 1032 (1996).

5.5.3. Meeting papers: Y. Yasaka, M. Miyakita, S. Kimoto, *et al.*, in *Proceedings of XIII International Conference on Plasma Physics and Controlled Nuclear Fusion Research, Washington, DC, 1990*, Vol. 2, p. 725.

5.5.4. Reports (preprints): G. V. Pereverzev, Report No. IPP 4/260 (Max-Plank Inst. for Plasma Physics, Garching, 1993).

5.5.5. Dissertations: J. B. Swan, PhD thesis (Harvard University, Cambridge, MA, 1974).

INSTRUCTIONS FOR PREPARING AN ELECTRONIC VERSION OF THE PAPER

1. General Requirements

An electronic version of the paper may be presented to the Editorial Board either simultaneously with the manuscript or after the paper has been accepted for publication. The electronic version and the manuscript must be identical. Electronic versions containing corrections and inserts that are not coordinated with the Editorial Board are not accepted.

The electronic version consists of a file containing the text of the paper and graphic files containing the illustrations.

The electronic version must be supplemented by a file in which the authors' names, the title of the paper, and the file names, as well as the text editing processor and graphic formats used, are listed.

All of the files must be tested for viruses.

The files may be either presented on 3.5" (or 5") floppy disks or sent by e-mail.

It is recommended to send the text and graphic files as *attached files.* If the files are too large, they may be archived by using one of the commonly used archivers,

such as ARJ, ZIP, or RAR. UUencoding may also be used.

2. The Text of the Paper

It is recommended to present the text in MS Word format for Windows using standard type fonts (e.g., Times New Roman, Courier New, Arial). The standard typesize is 12 pt.

It is important that the lines within one paragraph must not be separated by the carriage return (paragraph) symbol (which corresponds to the *Enter* or *Return* key). Texts with separation of lines within one paragraph are unacceptable.

3. Graphics

3.1. For bitmap figures, it is recommended to use the 600-dpi TIFF format with 256 shades of grey; the JPEG and GIF formats are also acceptable.

3.2. Vector figures should be presented in the format of the graphic program in which they are drawn [e.g., Corel Draw (up to version 8.0), Adobe Illustrator (up to version 8.0), Free Hand (up to version 8.0)], or in the EPS format. If the graphic program is not widely used, it is recommended to convert the graphic files into the WMF or EPS formats.

3.3. Photographs must be presented in the TIFF format (no less than 300 dpi).

3.4. The graphic files must be named so as to indicate the title of the paper and the figure numbers. Each file must contain one figure only.